



A thesis submitted in partial fulfillment of the requirements for the
degree in Master of Science in Applied Physics

Albert-Ludwigs-Universität Freiburg
Institute of Physics

Single Shot Electron Imaging of He and Ne Clusters Under Strong Mid-Infrared Laser Fields.

Presented by Cristian Enrique Medina Hernandez
Date 12. August 2019
Referent Prof. Dr. Marcel Mudrich and Prof. Dr. Frank Stienkemeier

Abstract

In this thesis a new data acquisition method is explained for correlate single shot Velocity map imaging (VMI) and Time of flight (TOF) measurements on doped Helium and Neon droplets ionized by a MIR femtosecond laser. Until now, the electron VMI from plasma explosions has been treated in a statistical way. With our method we analysed electron images for single coulomb explosion of He and Ne clusters under strong MIR fields. We analysed the maximal kinetic energy distribution that shows a strong dependency to the collected number of electrons and, at certain conditions, it can be modelled as an electronic homogeneously charge spherical cloud, where the electron in the perimeter of the sphere will determine the maximal kinetic energy in the explosion. This thesis, present the measurements and comparison of different noble gases under Mid and Near-Infrared laser pulses doped with Xe, Argon, Calcium and water.

We demonstrate that exist a laser intensity threshold necessary to start an optimal coulomb explosion. Moreover, the efficiency of the plasma formation present a strong relation to the cluster size and the doping level. Similarly, the cluster element didn't show an important function in the plasma creation other than characterize the cluster size. On one hand, the bigger droplets present a proficient plasma heating compare to the small ones. On the other hand, there exist an optimum doping level to efficiently start the plasma formation independent of the dopant element. Furthermore, the laser pulse duration in contrast to the laser intensity, shows an important role in the ignition of the smaller droplets when interacts with the plasma resonance, increasing the signal counts autonomously the power. It leads to conclude that the interaction time between the ionized electrons at the beginning of the process and the pulse is fundamental to the plasma formation.

On the single dopant component it was show that the plasma formation is independent of the dopant element used, but the doping level improves considerable the efficiency of the plasma heating. On contrary, when we used a combination on Xenon and Calcium, it was clear that exist an optimum mix of atoms where the replacement of a few Xe atom for Ca improves the signal up to the double.

Contents

0.1	Introduction	6
1	Theoretical Background	8
1.1	Helium Nanodroplets	8
1.1.1	General Properties of Helium	9
1.1.2	Helium Droplets	9
1.2	Neon Clusters	14
1.3	Composite Clusters	16
1.4	Cluster-Intense Fields Interaction	17
1.4.1	Photoionization for single atoms	18
1.4.2	Multiphoton and Tunnelling Ionization	20
1.4.3	Cluster Ionization	24
1.4.4	Homogeneous Charge Sphere Model	28
2	Experimental Setup	31
2.1	Source Chamber	31
2.2	Doping Chamber	33
2.3	Detection chamber	35
2.3.1	Velocity Map Imaging Spectrometer	35
2.3.2	Time of Flight Spectrometer	39
2.3.3	LT Detector	40
3	Data Acquisition and Calibration Methods.	41
3.1	Camera and Trigger Protocol	41
3.2	Calibration Methods	45
3.2.1	VMI calibration	45
3.2.2	Laser Intensity Calibration	47
3.3	Data Analysis	47
3.3.1	Event Recognition	48

4 Results	52
4.1 Helium Nanoplasma in NIR Fields	52
4.1.1 Laser Parameter Dependence	54
4.1.2 He Droplet Size Dependence.	56
4.2 Helium Nanoplasma in MIR Fields	59
4.2.1 Helium Droplet Size Dependence.	61
4.2.2 Doping Dependence	63
4.2.3 Laser parameter Dependence	70
4.3 Neon Nanoplasma in Mid-Infrared	75
4.3.1 Doping Dependence	77
4.3.2 cluster Size Dependence	78
4.3.3 Neon Pulse Duration Dependence	80
5 Summary and Discussion	85
5.1 Laser parameters dependence on clusters	85
5.2 Cluster Size Dependence	87
5.3 Doping Dependence	89
5.4 Electron-Energy Distribution	93
6 Bibliography	101

List of abbreviations

ATI	above threshold ionization
BSI	barrier suppression ionization
CCD	Charge-coupled Device
CPA	Chirp Pulse Amplification
CWL	Central wavelength
EM	Electro Mechanics
LASER	Light Amplification by Stimulated Emission of Radiation
LT	Langmuir-Taylor
MCP	Micro Channel Plate
NIR	Near Infrared
pBASEX	polar Basis Set Expansion
PID	Proportional – Integral – Derivative
TBR	Three Body Recombination
TOF	Time of flight
VMI	Velocity Map Imaging
VUV	vacuum ultra violet
XUV	Extreme ultraviolet

0.1 Introduction

Physicists always have been fascinated to explain and resolve dynamic processes in short leaps of time of times and to characterize in a time scale fast processes with highly physical interest. Describing these systems requires to acquire data in brief time windows, for example, a film is only a consecutive sequence of photographs that recreate a large time laps in a smaller time scale. For atomic physics, we are talking about a micro-cosmos that can go down to attoseconds. Experiments in attoscience have given up to Nobel prizes, for example Ahmed Zewail in 1999, who demonstrated that femtosecond pulses allow a temporally resolved observation of ion movements in molecules [79].

The duration of the dynamics of a system is related directly to its energy and its quantum states, in other words, to its size. For example, to explore ion dynamics in molecules, times can fluctuate between femtoseconds to nanoseconds [28] and energies up to several electron volt eV. Furthermore, for smallest system as the relaxation of an inner shell vacancy [16] or the process of tunneling ionization [72] occur in attosecond regime, with energies that varies typically on the milielectronvolt scale (meV) for its energy levels. And further, for processes as nuclear fission and quasifission are predicted to unfold even faster, typically on a zeptosecond time scale [57].

To study ultra-short-dynamics, physicist have been challenged to create detector systems based on the interaction light-matter. Along the last decades, experimental schemes have been devised developing new light sources, as for example the laser, to interact with the microcosms. Nowadays, laser pulses can reach up to extreme non-linear optical processes, producing single isolated pulse of ultraviolet(UV) waves as short as 67 as [80]. Such fast pulses open up the possibility of time resolved measurements for short processes like nuclear dynamics, the generation of high energetic electrons and ions in the KeV-regime [22], as well as intensive XUV and attosecond pulse experiments [64]. Not just the pulse duration has been improved within the years, but also the energies that the pulse can deliver, laser pulses with intensities up to 10^{21} W/cm² are available commercially [51].

Femtosecond and attosecond lasers pulses are a milestone in the control and ignition of atomic processes. These advances have enabled the development of new research areas, as well as the investigation of ultrafast dynamics of highly excited matter on a nanometer scale. In particular, many studies have been published in recent years on atomic and molecular clusters that investigate their interaction with NIR, UV or XUV pulses [64]. These are motivated by a broad spectrum of possible applications such as the generation of energetic electrons and ions in the keV

regime [22].

In this thesis, we focus our efforts on the ionization processes by Near-Infrared (NIR) and Mid Infrared (MIR) femtosecond pulse in doped noble gases clusters. The interaction of the dopant with the laser field results in an energy transfer to the cluster that starts an ionization process, known as a nanoplasma. The oscillation of the electrons driven by the laser field inside the clusters creates an energy transfer that ionize the cluster atoms [22]. This process, caused predominantly by electron impact ionization, makes an avalanche-like ionization of the atoms in the cluster, leading to a heating of the plasma and, as a result, a hydrodynamic expansion and Coulomb explosion. Here, we studied the electrons and ion's resulting from the coulomb explosion using a velocity map imaging and a Time of flight spectrometer set in parallel to acquire the data and reconstruct the initial energy configuration of the plasma.

In the First chapter, we will present a brief introduction to the Helium and Neon cluster generation, a short explanation of the ionization process and the basic background for the plasma formation and coulomb explosion process. In the second chapter, we show a detailed explanation of the setup used, explaining from the creation of the Helium droplets process to its detection, describing as well the doping and ignition process. Finally, a detailed explanation of the correlation method for the VMI-TOF measurements is done, showing the set-up of the data acquisition and its advantages. In the third chapter, we discuss the acquisition method and the calibration methods used in the experiment as well as a brief explanation of the analytical model for the coulomb explosion, followed by the description of the data analysis method. Finally on the four chapter, we present the results and its analysis followed by a summary and outcome of the experiments as well as the inputs for future works to improve the results.

1 Theoretical Background

In this chapter we will present all the theoretical background necessary for the development of this project, from the creation and behaviour of the Helium and Neon droplets to the theory of the plasma formation and the coulomb explosion processes. In order to guide the reader in an organized way, the sections are organized in the same order the experiment is performed.

1.1 Helium Nanodroplets

The combination of cryogenic matrix isolation, discovered in 1954 [75], and the now well-defined properties of helium (He), especially its superfluidity phase discovered in 1937 by *Kapitza et al* [37], gives as a consequence, an excellent molecular matrix like the helium nanodroplets. Helium has unique properties that make it a perfect source for the nanophysics experiments. For example, it has any optical transitions in the entire infrared and visible regime. In addition, helium clusters are able to pick up atoms and molecules that form different complexes of the species embedded in the interior or the surfaces of the droplet, acting as an ideal matrix for spectroscopy of atoms and molecules. [65] [71].

The size of a Helium cluster can be up to 10^8 atoms, and reach the ultra-cold temperature regime (close to 0.37 K [70]) [18]. Two main advantages of this cooling properties arise. First, dopants in the helium nanodroplet are set to their absolute vibronic ground states, avoiding other possible spectra and establishing the cluster in a specific state. Second, the fast cooling helps in the formation of isomers that are difficult or impossible to generate with other methods [52]. Third, because the superfluid phase of the helium [26], the bond between dopants and helium is weak. Therefore, in contrast to spectroscopy in other matrices with higher temperatures, the optical transitions of many dopants are barely influenced by the helium matrix [71]. The theory of He super fluidity will not be part of this section, this information is well documented in other sources, and here we are based on ref. [18] where all theory is well presented to the reader. In the next section we will dedicate a bigger effort to explain the theoretical and technical background of the helium nanodroplets

creation as well as the physical and technical process to dope it.

1.1.1 General Properties of Helium

At room temperature, helium is a light inert gas. It is odorless, colorless, tasteless, and after hydrogen, the second most abundant element in the universe. [18]. It has a simple 2 atoms structure, exhibiting numerous exotic phenomena whose theoretical descriptions are rather complex in many cases, i.e it characteristics of a quantum fluid. From helium exist two stable isotopes 3He and 4He . 4He has two electrons, two protons and two neutrons, no nuclear spin and no total spin, pertaining to the bosonic family, while 3He with only one neutron has a spin of $I = 1/2$ and belongs to the fermions [4].

The bosonic state 4He is especially of interest, at temperature $T \leq 2.8K$ and under normal pressure has a phase transition from "normal liquid" $He - I$ to super liquid $He - II$ [67], in which the helium can be described by a Bose-Einstein condensation. Even the fermionic 3He exhibits this phase transition at $T \leq 0.03K$ [31].

The superfluidity of helium two (He-II), at temperatures close to absolute zero, brings with it some unique features. The essential Properties for this include an almost disappearing viscosity in the superfluid phase, weak interaction, very efficient cooling, and the transparency for electromagnetic radiation up to wavelengths in vacuum ultraviolet (VUV) Spectral range [18]. Helium has therefore in the complete visible spectrum no transitions from the ground state. Through the noble gas configuration, helium has a spherically symmetrical electron distribution [45], it can hardly be polarized and is the least reactive of all the elements.

1.1.2 Helium Droplets

The production of Helium droplets had to overcome first one principal problem, its condensation. At the end of the 19th century, many noble gases were liquefied for the first time by applying pressure at room temperature. However, for helium and hydrogen, this method was not successful. In 1922 Kamerlingh Onnes reached temperatures below 1 K by reducing the vapor pressure above liquid helium to about $2 * 10^{-5}$ bar with a series of pumps [13]. The Joule–Thomson effect [74] was the responsible for Onnes experiment to reach this low temperature. The basic idea is that under suitable conditions an expanding gas performs work against its internal forces, for example, when a gas is expanded through a small nozzle thermally isolated from its surroundings. The expansion under these conditions takes place at constant enthalpy, since the expansion nozzle performs none work. It follows the next relation.

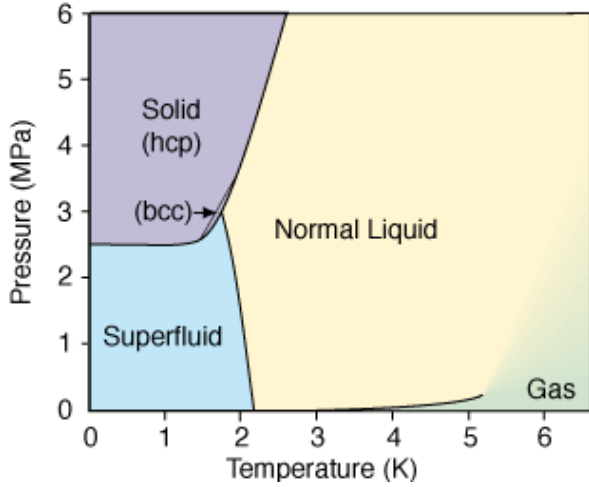


Figure 1.1: ${}^4\text{He}$ Phase transition at Ultra cold temperatures. ${}^4\text{He}$ is the more common isotope of helium. It remains liquid at zero temperature if the pressure is below 2.5 MPa . The liquid has a phase transition to a superfluid phase, also known as Helium-II, at the temperature of 2.17 K (at vapor pressure). Taken from [1]

$$W = H_1 - H_2 = (U_1 + p_1 V_1) - (U_2 + p_2 V_2) \quad (1.1)$$

Where H is the enthalpy before and after, $U = \frac{3}{2}Nk_bT$ is the internal energy, and follows the ideal gases law $pV = Nk_bT$ [18]. Under Joule–Thomson effect conditions, $W = 0$ so $H_1 = H_2$, this expansion leads to a cooling or a warming, bank on the conditions it becomes supersaturated. As a result, condensation takes place and a beam of clusters is formed.

Helium nanodroplets are typically produced by a continuous or pulsed adiabatic expansion of pre cooled gas through a small aperture from a reservoir into a vacuum [65]. In this process a droplet jet is formed, and its characteristics (blasting speeds and size distribution) can be changed due to the manipulation of the setup. For example, pressure differential between the reservoir and the vacuum chamber (usually in the range of a few to 10 MPa), the nozzle temperature (from a few K to $T \leq 40\text{ K}$) or the nozzle size (with pinholes of diameter rounding $5 - 20\mu\text{m}$).

When the Helium expands after the nozzle, its potential energy alters to kinetic energy in a supersonic flow field. After the expansion into the vacuum, the gas becomes supersaturated and condensation occurs, creating the beam cluster. These clusters are made of atoms or molecules, held together by Van der Waals forces, in this case He-He interaction, that share the same kinetic vector. This means that, the two particles travel as close and parallel to each other so bonding is possible as shown in Fig 1.3. From the reference frame of the cluster, each of its molecules is

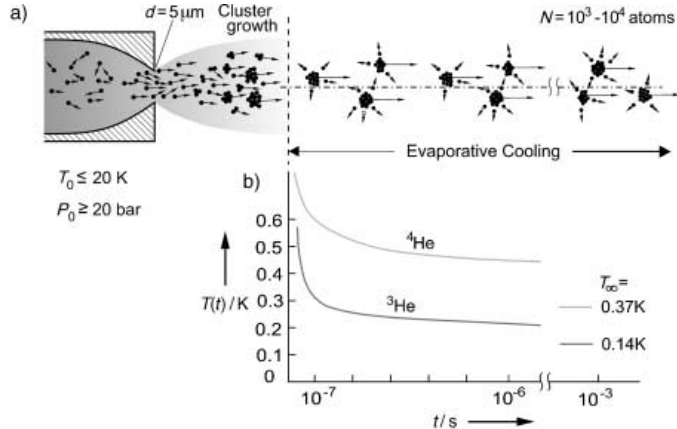


Figure 1.2: a) Schematic representation of the processes leading to the formation and subsequent cooling of Helium droplets in a gas expansion. b) Calculated dependence of the droplet temperature on time for ${}^4\text{He}$ and ${}^3\text{He}$ droplets after they have left the cluster, taken from [7]

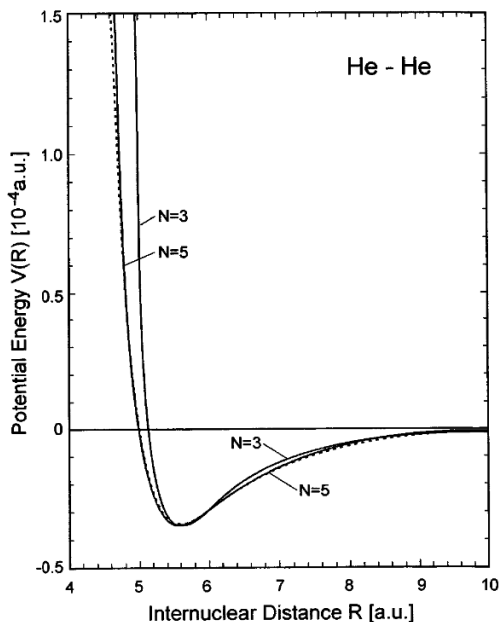


Figure 1.3: Van der Waals potential for He-He interaction. Taken from [7]

close to zero movements, in Helium this enhance the conditions to be liquid and in consequence, superfluidity is achieved [29].

Depending on the buffer gas used, the mechanisms for cluster formation in the supersonic expansion range as a condensation either from the gas phase or the liquid phase. In case the expansion is isentropic (adiabatic and reversible), the expansion is represented by a vertical line in this diagram. Clusters formed by condensation from the gas phase occur when the expansion crosses into the two-phase region on the right-hand side of the critical point. Clusters formed by fragmentation of the liquid

phase occur when the expansion crosses into the two-phase region on the left hand side of the critical point. The diagram is an example of three gases, He, Ar and H₂ at different pressures ($p' = P/P_{critical}$) [40]. The curves represent the regions where the supersonic expansion is possible and the temperatures (in Fig dimensionless) that each gas should have in order to achieve clustering and cooling [40].

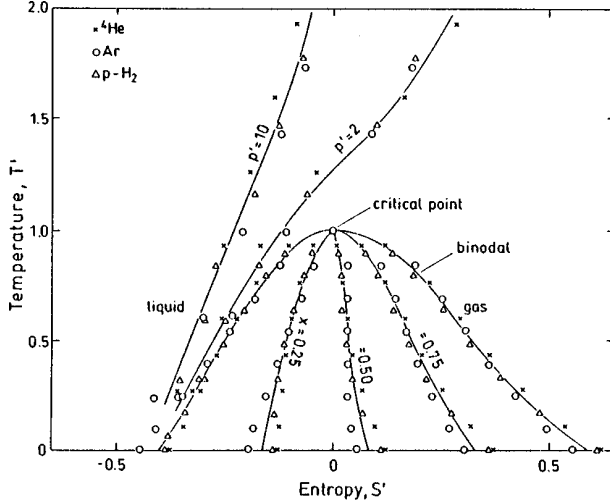


Figure 1.4: Dimensionless phase diagram for He, H₂ and Ar. Where T is dimensionless $T' = (T - T_{tp})/(T_{cr} - T_{tp})$, same as entropy $S' = (S - S_{cr})/\Delta S_{tp}$ and x is the fraction of the fluid in the gaseous phase, where the subscripts *cr* and *tp* refer to the critical point and triple point respectively, and ΔS is the entropy change for vaporization. The curves are drawn as guides to the eye, not exact measurements, taken from [40].

There is no mathematical approach of the physics behind this supersonic expansion but usually, Raleigh scattering measurements in combination with an empirical scaling law [29] are used to estimate the mean cluster size, assuming a certain degree of control over the cluster size distribution by adjusting the nozzle width and the source pressure. The droplet size distribution during supersonic expansion in the follows a log-normal distribution of the form [32].

$$p(N) = \frac{1}{\sqrt{2\pi}N\sigma} \exp\left[-\frac{(\ln(N/N_0))^2}{2\sigma^2}\right] \quad (1.2)$$

Where N is the number of atom in the cluster, σ is the distribution width and N_0 is the most likely numbers of atoms. Following it give a mean value.

$$\bar{N} = \exp\left(\mu + \frac{\sigma^2}{2}\right) \quad (1.3)$$

With a half width maxima of [32]

$$\sigma N_{\frac{1}{2}} = \exp \left(\mu - \sigma^2 + \sigma \sqrt{2 \ln(2)} \right) - \exp \left(\mu - \sigma^2 - \sigma \sqrt{2 \ln(2)} \right) \quad (1.4)$$

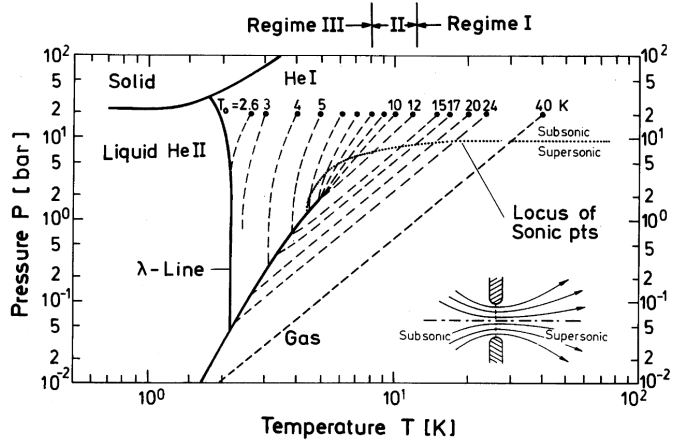


Figure 1.5: Expansion regimes. ${}^4\text{He}$ Pressure-Temperature phase diagram for Nozzle beam expansions starting at a backing pressure of 20 bar and a temperature. As discussed, qualitatively different behaviors are shown for the regime I-II and II where starting in the gas phase, near the phase transition respectively. Taken from [9].

As shown in Figure 1.5, the initial gas conditions (pressure, temperature and nozzle size) in the free expansion phase will determine the characteristics of the final helium beam. From here, three main regimes can be defined.

Regime I or sub-critical expansion, begins in the gas phase and leads to droplet formation via condensation. This is the case of most expansions since the pressure is located below the critical pressure P_c . Regime II, also called as critical expansion, is a long-winded regime that includes all trajectories which are near the critical point, leading to random expansion and difficult control of the beam due to the large fluctuations in density. Regime III, the super-critical expansion, starts at low temperatures where the helium stops behaving as an ideal gas, expecting flashing or cavitation breaking up the liquid drops jet. [9]

super-critical and sub-critical regimes have been studied in the last several years and are clearly identified in the resulting size distributions. Figure ?? shows that super-critical expansion forms large droplets (usually between 20–100 nm diameter) while a sub-critical expansion is suited to generate small droplets (around 5–10 nm). A simple relation that can be done to calculate the size or number of atoms in a Custer is using.

$$r = N_{1/3} * \rho A \quad (1.5)$$

Where r is the radius of the beam, and ρ its density, in this case, for helium $\rho = 0.0022 \text{ A}$ [66], but this approximation is not exact due the variation in He density at this temperature. As expected in both regimens, for creating larger helium nano droplets, higher He pressure and lower nozzle temperature are used. For our experiment a $5\mu\text{m}$ nozzle was used at temperatures oscillating between $11 - 20\text{K}$, and backing pressures of 30, 45 and 50 bar.

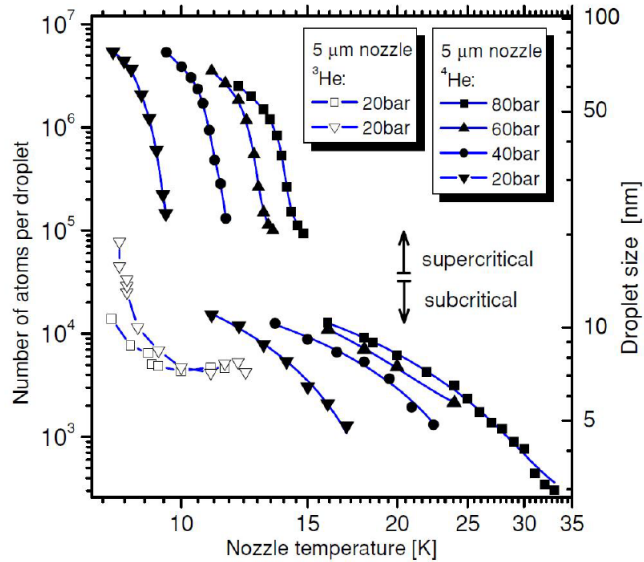


Figure 1.6: Sizes of the ${}^4\text{He}$ droplets as a function of nozzle temperature T and pressures, based on [70], using a $5\mu\text{m}$ nozzle. The sub and super critical regimes are clearly differentiated. Taken from [65]

1.2 Neon Clusters

Neon (Ne) is the second lightest inert gas with atomic number 10, it has 3 stable isotopes in nature, the ${}^{20}\text{Ne}$ with more than 90% of abundance, followed by ${}^{21}\text{Ne}$ and ${}^{22}\text{Ne}$ [49]. At extreme temperature, Neon is solid as shown in the graphic 1.7 and its triple point is around $T_p = 24\text{K}$ [78]. Neon is a noble gas, it shares most of the properties already mentioned from Helium, except for its superfluidity. It has a quite large ionization potential for its first electron at $I_p = 21.56 \text{ eV}$, what makes quite suitable to use it as a matrix with strong fields lasers, because at low intensities, it will not interact with the light source, so dopants can be carried out in a non-interactive way.

Ne cluster has been proved to provide an ideal medium for chemical reactions as solvation effect and heterogeneous chemistry at a microscopic level [25]. With a

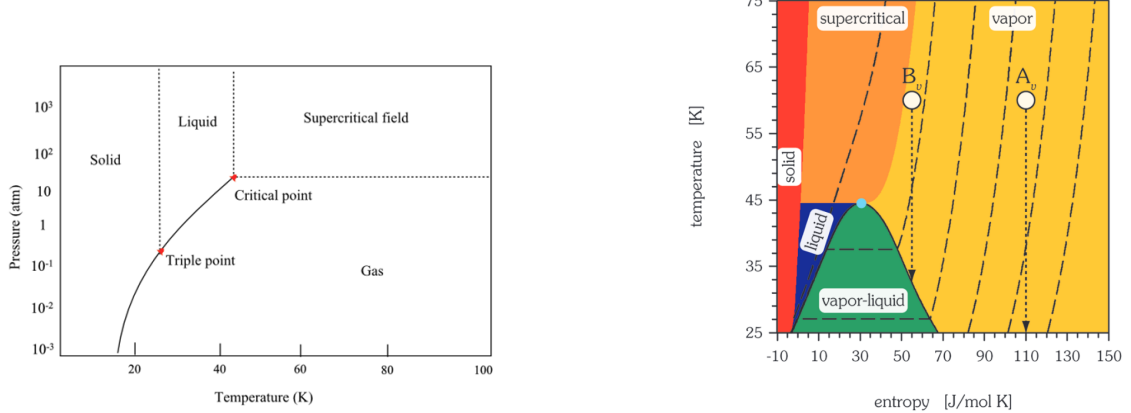


Figure 1.7: On the left, Neon phase diagram. taken from [78], on the right, $T - S$ phase diagram of Ne. The critical point is located at $T_c = 44.49$ K and a molar entropy of $S_c = 30.76$ J/(mol K). The dashed lines represent regions. Taken from [10]

properly regulated pick-up system the reactants are deposited in a controlled way in the cluster and it becomes a nanoreactor equivalent [24].

The conditions for creating Neon clusters are quite similar to the ones explained above, also well explained in the famous Haga law [30]. Several studies have been realized on the characterization of Ne clusters, for example by *R. Von Pietrowski et al* [53] who studied the Electronic excitations of Xe atoms and Xe_2 molecules embedded in free Ne clusters. On contrary to helium, is important to work with neon clusters at temperatures and pressures far from its solidification point. At extreme low temperatures, small differences in pressure leads to big size changes on the clusters, the higher the pressure in the nozzle the bigger the droplets. As an example, in *Pietrowski* work, it was shown that small droplets, $N = 300$, where N is the number of atoms in the cluster, are in a "liquid" state but for bigger droplets solidification starts to be present. In addition, the location of the dopant will be affected drastically by these sizes changes. When the droplet is in a liquid state the dopant atoms are free to move to the center contrary to denser droplets, where the dopant will stay at the surface.

The T-S representation of Helium, Fig 1.7 shows the isentropic processes as simple vertical trajectories. One advantage in this color plot is the visibility of the two-phase region where condensation may take place. The dashed lines represent isobaric lines at $p = 100, 1000, 10000, 100000$ Pa from left to right respectively. On one hand, supersonic expansions which originate in the vapor phase, at a very low source pressure equivalent to a comparatively large stagnation entropy s_0 , will not reach this region. On the other hand, for negative entropies the solid state is always reached although for lower temperatures and a relative small entropy, the liquid

state is the predominant. [10]

1.3 Composite Clusters

We can define a composite cluster or doped cluster, as an atomic lump that contains one or more different atomic elements. The main interesting properties in non-doped clusters are usually set as a function of its size, but for doped clusters, the interaction between the elements creates new degrees of freedom that makes more complex its interaction. For example, the new mixture will have different structural properties due the spatial distribution of the species [65]. Hence, composite clusters exhibit a more diverse behaviour and offer more opportunities to study different characteristics of the material.

The difficult problem to overcome in composite cluster is how to create them. Two techniques can be used. The first one, is the co-expansion of a previous mixed gas [68]. The second one is to produce first the cluster and then cross it with an atomic beam of the doping species.

For the first technique, clusters are produced by adiabatic expansion of mixtured gas through a narrow conical nozzle into vacum [68]. The cluster formation process in the coexpansion of a binary mixture is less well known beacuse it envolves several technical problems, depends on possible interactions between the elements, the condensation ranges of the bulks and even in the affinity of the materials [58].

The second thechnique, used in this study is the one called pick-up process [25]. The idea is simple, as a snowball on its way downhill collects or pick-up more snow, the helium cluster after being directional selected through a skimmer, passes through a doping cell full of a dopant gas at low densities ($10 - 2\text{Pa}$) [65]. As a result, the gas atoms that are along the droplet cross sections will be captured by the beam and travel with it. The probability for Helium droplets to collect k atoms or molecules via inelastic collisions depends on the length of the oven cell l , the cross section of the droplets σ , and the particle density inside the cell n . As l and σ remains constant, varying the density in the doping cell can regulate the abundance of k , following Poissonian statistics.

$$P_k(l, n, \sigma) = \frac{(ln\sigma)^k}{k!} e^{(-ln\sigma)} \quad (1.6)$$

Two important properties of these relations can be deduced. First, the maxima of different cluster sizes are equidistant, $n_{max} = \frac{k}{l\sigma}$ and second, the exponential function in the equation becomes nearly one for small particle densities [8].

Every pick-up process leads to an energy transfer to the droplets. As the dopant

rapidly cools down, that means an energy transfer to the Helium, causes an evaporation of some He atoms to keep the temperature unchanged in the cluster. This Helium evaporation or "shrinkage", leads to a decrease in the cross section of the droplet and the probability to collect further particle. At a certain energy entry, the complete droplet evaporates if too many dopants access to it. With the average kinetic energy E_{kin} , and E_{in} the internal. The involved energy is composed of the following contributions [8].

$$E = \langle E_{kin} \rangle + E_{in} + E_{binding} + E_{cluster} \quad (1.7)$$

Where

$$\langle E_{kin} \rangle \approx \frac{3}{2}k_b T + \frac{1}{2}mv^2 \quad (1.8)$$

Is the final kinetic energy of the droplet depending on its mass, velocity and temperature in the gas cell.

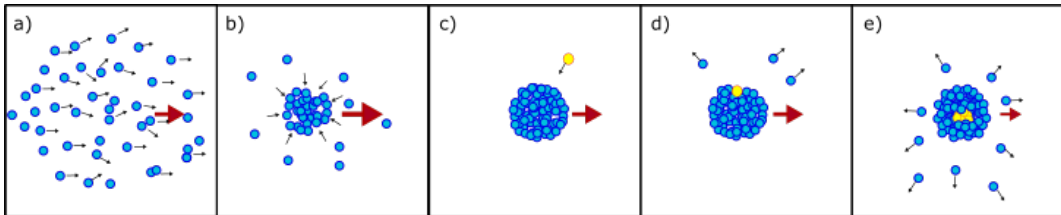


Figure 1.8: Animation of the Helium creation, doping and evaporation. From left to right, we see the Helium droplet production; after being released by the supersonic jet, the Cluster formation, the pickup process of the dopant and finally the Helium shrinking process.

Several studies have focused on the $E_{binding}$ with ${}^4\text{He}$, so the energy binding for a broad number of materials is known. It is also important to take into account that the binding energy includes the cluster-dopant binding as well as the dopant-dopant relation. [70]. The energy bounding for example of Xe-He is around 26.9 meV [44], or He-H₂O is about 0.1 eV [45].

1.4 Cluster-Intense Fields Interaction

The understanding of the interaction atom-fields has been studied broadly in physics since Einstein Photoionization Theory [17], who gave a base on all the quantum electrodynamics theory. The basic idea supporting this theory is the behavior of light as an electromagnetic field, where the electron, as a bounded charge in the atom, can be affected. This quantum dynamic theory is well understood since

1957 for small atoms, with one, two or few electrons [3], but still big molecules and atoms have been challenging scientist for years. In this chapter we will give a brief introduction to the atomic photo ionization process, explaining at the same time multi-photoionization and tunneling processes, so we can finish with a more detailed presentation of strong field interaction with clusters and the Keldish theory.

1.4.1 Photoionization for single atoms

The photoionization process describes the withdraw of an electron from a bound state into the continuum by interaction with electromagnetic field radiation [6]. The atomic bounded electrons while going through an electromagnetic field, in our case the laser beam, can absorb enough energy to get excited and fly away from the nucleus. A bound electron only can escape from an atom by absorbing photons its energy exceeds the binding energy [17]. When the photon energy of the laser is smaller than the ionization potential of the target, the electron can absorb two or more photos in the ionization process, this is called Multi photon ionization (MPI). Another possible process is called, tunneling ionization, where due the quantum mechanical properties of the electrons under certain conditions absorbs enough energy enough to be in an above threshold regime, due it quantum dynamic properties it can escape from its bonds via tunneling.

There is a variety of theoretical approaches to describe the interaction of laser fields with atoms. The Hamiltonian of the system of N particles (ions and electrons) with pairwise Coulomb interactions under the action of an external time-dependent electric field has the form:

$$H = \sum_{1 \leq i \leq N} \frac{P_i}{2m_i} + \sum_{1 \leq i < j \leq N} \frac{q_i q_j}{|r_i - r_j|} + \sum_{1 \leq i \leq N} q_i r_i \varepsilon(t) \quad (1.9)$$

where r_{i,p_i} and q_i are the coordinates, momenta and charge of the particles, including the interaction between the classical electric field and $\varepsilon(t)$ where [50]

$$\varepsilon(t) = \varepsilon_0 e_z \cos(\omega t + \varphi) \quad (1.10)$$

The process that drives ionization can be divided on two regimes, a quantum electrical regime and a classical one [38]. Equation 1.9 use the non-relativistic approximation and neglect contributions from magnetic fields. The classical description of the laser field is a good approximation for intense pulses, otherwise, quantum electrodynamics description is necessary.

An electron in the initial level with energy E_i can absorb a photon with energy

$\hbar\omega$ leading to final transition where $E_f - E_i = \hbar\omega$, when the energy of the photon is larger than the bounding energy, or the Ionization barrier the electron is free with a the remaining kinetic energy $E_{kin} = \hbar\omega - I_{pot}$ [2]. In classical mechanics the probability of the energy transition depends directly on the cross section (σ) of the electron and the field. However, in quantum mechanics, the photoionization cross section is related to its transition probability between the initial and the final state given by Fermi's golden rule

$$W_{|i\rangle \rightarrow |f\rangle} = \frac{2\pi}{\hbar\hbar} |\langle f | H | i \rangle|^2 \delta(E_i - E_f - \hbar\omega) \quad (1.11)$$

$$\sigma(\hbar\omega) = \frac{2\pi}{3} \alpha a_0^2 \hbar\omega |\langle f | r_n | i \rangle|^2 \quad (1.12)$$

When Eq. 1.11 is the transition probability of one electron to jump from initial state i to final state f , where H is the Hamiltonian operator. Eq. 1.12 is the consequent cross section considering only the dipole part of the interaction Hamiltonian, where α is the fine structure coefficient, r_n is the position operator of the electron n [23].

The energy photon needed to ionize an atom, is directly proportional to the energetic distance between the electronic states and the ionization threshold. For states closer to the ionization potential a UV photon can be enough to free an electron but for inner electrons higher photon energies are required, varying from few eV to the order of several of keV, needing radiation sources at shorter wavelengths such as XUV to X-rays. [2]

After photoionization is complete, the electronic structure of the atom needs to rearrange due to the vacancy left by the ejected electron. Relaxation processes can happen during this time. An electron from the outer shell will decay and replace the freed one, therefore the energy difference of the needs to be released in the form of a fluorescence photon or Auger electron. On one hand, in case of a fluorescence decay the ionic state of the target does not change, since no additional electron is released. On the other hand, the Auger decay is a non-radiative relaxation process, where a second electron is released from the Coulomb potential of the ion [56].

In example. As shown in fig 1.9, if a photon with energy $\hbar\omega > E_{bin}$ ionized an electron, this will leave the atom lifting a gap. An electron in the higher levels will replace the outer one, leaving an excess of energy. The outcome will be a fluorescence process with $E_{flu} = E_{in} - E_{out}$ or , the Auger $e-$, if $E_{in} - E_{out} > E_{bond}$ and this electron can also escape the atomic Coulomb potential [62].

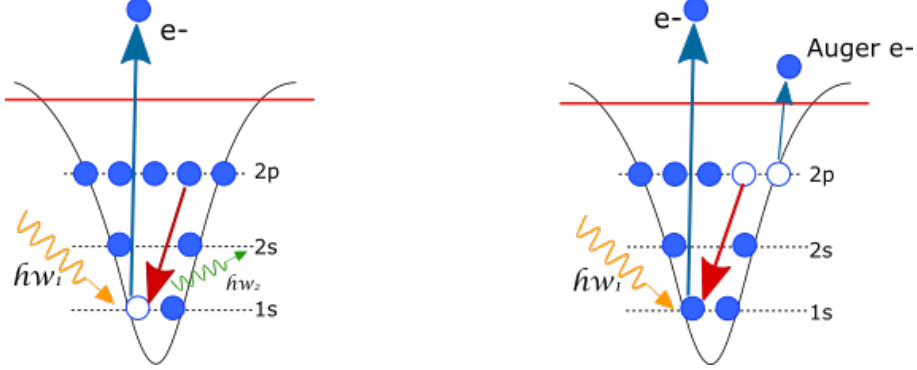


Figure 1.9: Two examples on the relaxation processes. On the left, A photon ionized an electron and the Electron E_{in} replaced, expelling a fluorescent photon in the process. On the right, the energy released by the replacement electron is enough to make another electron in the outer shell to also go to the continuum, Auger electron. Taken from [56]

1.4.2 Multiphoton and Tunnelling Ionization

Ionization is also possible, even when the photon energy is lower than the binding potential. Laser Fields with intensities below $I \leq 10^{14} \text{ W/cm}^2$ are not strong enough to change the binding potential of an atom significantly [60] and it is when multiphoton Ionization takes place (MPI). MPI is the simultaneous absorption of several photons to overcome the ionization barrier. The way MPI occurs depends on the laser frequency and intensity. When the intensity is much lower than the characteristic atomic resonance, MPI occurs via transitions through virtual states. Ionization by several photons at low laser intensities can be realized by the so-called resonance enhanced multiphoton ionization (REMPI) [47]. Ionization by a REMPI process takes place in two steps. First, a resonant excitation by one or more photons occur on an electron state of the atom. In the second step, this electron state is transformed into a virtual state, to an upper state until the electron is excited by spontaneous decay. So for example, the total energy absorbed by an electron until it gets ionized is $n * \hbar\omega > I_{pot}$ where n is the number of photons absorbed until it actually have enough energy to overcome the potential I_{pot}

For Laser intensities $I > 10^{14} \text{ W/cm}^2$, with higher intensities and lower frequencies, tunneling ionization (TI) is more likely to occur. In this case, the binding potential of the atomic state is strongly affected by the electric field of the laser. Around the peak of the electric field the potential gets narrower, and the electron in the outer states gets closer to the bidding barrier, allowing the electron to tunneling through the confining potential to the continuum [27]. TI is inherently a quantum process. The bending of the Coulomb potential becomes by the superposition of the coulomb potential and the laser field. Therefore TI must occur when the time of the

ionization is shorter than a laser oscillation cycle [6]. Based on the same principle, when the laser field becomes so strong to lower the binding potential that separates the highest electron level, then the electrons in this state become free electrons. This process is called barrier suppression ionization or BSI [42].

In Fig. 1.10, we present a sketch of the 3 possible ionization processes explained above. On the left, a simple ionization process where a photon with energy $E_{phot} = \hbar\omega$ is higher than the potential barrier I_p . In the center, a MPI process is shown, n photons excite the inner-shell electron, exiting it through a virtual level until it finally has enough energy to be free to the continuum. Finally on the right, a TI happens. Here the coulomb potential barrier is affected by the laser files bending, the outer shell electron gets closest to it until it tunnels [56].

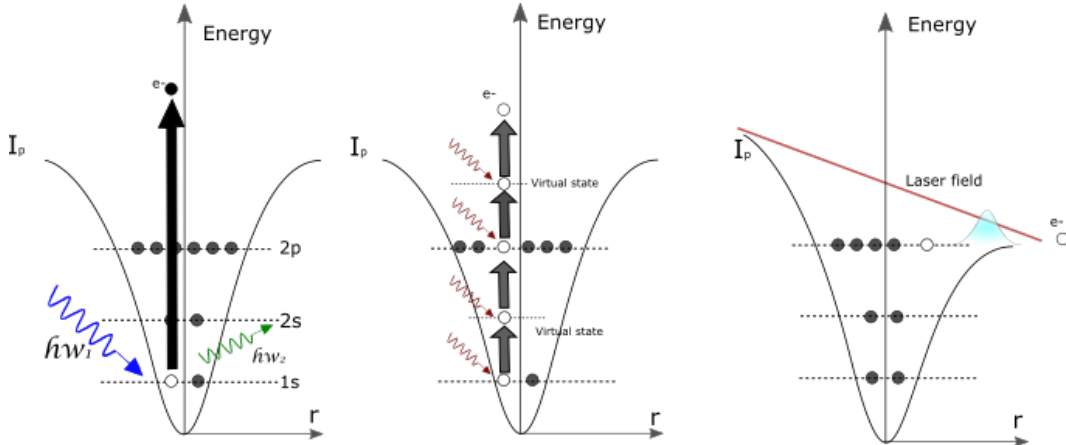


Figure 1.10: On the left is the sketch of a single photon ionization process, where a photon with energy $E_{phot} = \hbar\omega$ is higher than the potential barrier I_p . On the center the MPI process, inner-shell electron absorbs n photons, getting excited through the electronic levels (reals or virtual) until it reaches the continuum. On the right the BSI Process, the coulomb potential barrier bends by the laser fields, been lower than the outer shell electron state, the electrons can scape easilly. Based on [56].

As explained the Intensity of the external field plays an important role in the ionization process. A rather easy way to differentiate when each process needs to be taken into account is provided by the Keldysh parameter [39].

$$\gamma_k = \sqrt{\frac{I_p}{2U_p}} \quad (1.13)$$

Where γ_k is the Keldish parameter, I_p is the atoms ionization potential and U_p is the ponderomotive potential defined as:

$$U_p = \frac{e^2 E_0^2}{4m_e \omega_0^2} \propto I \lambda^2 \quad (1.14)$$

Where m_e is the mass of the electron, ω_0 , λ , I and E_0 are the frequency, wavelength, intensity and the peak of the electric field of the laser pulse. On one hand, when the Keldish parameter is higher, $\gamma_k \gg 1$ MPI regime is considered. On the other hand, the $\gamma_k \ll 1$ describes the TI interaction.

Keldysh Theory

In this section we will give a brief introduction to the keldysh theory based on the work of Keldysh et al, [39], and the papers review of the theory by [54] and [38]. For a deeply explanation we recommend the reader to reference this works.

The keldysh Theory, also known as the Keldysh–Faisal–Reiss theory (KFR), is well used for the description of quantum process induced by intense laser radiation. The applications and advantages of Keldysh formulation in many-body theory among several, can overcome from, treatment of systems away from thermal equilibrium, solutions in super symmetry methods of systems with quenched disorder or to the calculation of the full counting statistics of a quantum observable [36].

According to the Keldysh Ansatz, the transition probability amplitude between an atomic bound state and the continuum by the value of the photoelectron momentum p measured at the detector is given by [54].

$$M_k(p) = -\frac{i}{\hbar} \int_{\text{inf}}^{+\text{inf}} \langle \Phi_p | V_{\text{int}}(t) | \Phi_0 \rangle dt \quad (1.15)$$

Where M_k denotes the Keldysh transition probability, Φ_0 is the bond state wave function unperturbed and Φ_p is the canonical momentum, equal to p , also known as the Volkov function, and V_{int} is the electron field interaction operator. If the amplitude of ionization $M_k(p)$ is known, the differential probability to find the photo-electron in the elementary volume near the momentum p is given by the momentum distribution of the photoelectrons

$$dW(p) = | M(p) |^2 d^3 p \quad (1.16)$$

Giving a total probability of

$$W = \int | M(p) |^2 d^3 p \quad (1.17)$$

Meaning that, for enough long pulses, containing a large number of optical periods

so that its electromagnetic field is close to a periodical function of time close to the initial, it is physically more appropriate to use probabilities per time unit (rates) instead of time-integrated values.

Ponderomotive Energy

As soon as an electron is released into the continuum, it starts to be under the influence of the external laser field. A description of the energy that it acquires during this interaction is given by the ponderomotive energy (PE).

$$U_p = \frac{e_2 E_a^2}{4m\omega^2} \quad (1.18)$$

Where m and e is the electron mass and charge, E_a and ω_0 amplitude and frequency of the electric field respectively. The formula of the ponderomotive force can be easily derived as shown in [55] [11]. Let's consider a polarized electric field (in a.u.).

$$\mathbf{E} = \hat{z}E_a \sin(\omega_0 t) \quad (1.19)$$

Considering only the \hat{z} -components so we can avoid the vector sign. By classical mechanics we have.

$$p(t) = - \int_{t_0}^t E(t') dt' = \frac{E_0}{\omega} (\cos(\omega_0 t) - \cos(\omega_0 t_0)) \quad (1.20)$$

The term on the left of the parenthesis is known as the time varying Quiver terms, and on the one on the right, refers to the drift motion. Expressing the fields in terms of vector potential we will have

$$\mathbf{E}(t) = \frac{\delta \mathbf{A}(t)}{\delta t} \quad (1.21)$$

$$p(\infty) = A(t_0) = - \int_{-\infty}^t E(t) dt = \frac{E_0}{w} \cos(w_0 t_0) \quad (1.22)$$

in the case where the pulse duration is big $t \rightarrow \infty$ the $p + A(t) = 0$. This means that the momentum acquired by the electron will depend on the phase it is realized wt . Since the electron can be unbound in any phase of the laser pulse, will have an average kinetic energy described by

$$U_p = \frac{1}{2\pi} \int \left(-\frac{E}{w} \cos(wt) \right)^2 d(wt) = \frac{E_0^2}{4w_0^2} = \frac{p_{max}^2}{2} \quad (1.23)$$

The ponderomotive energy also gives the maximum momentum that an electron

can acquire (eq. 1.22), given at the maxima. The ωt phase relation, defines what it called *the three step model* showed in figure 1.11. The first step corresponds to $\omega t < \pi/2$ where the laser field is suppressed, and as explained above, TI or BSI can take place. The second step, is where $\omega t > 3\pi/2$, on contrary step 1 the potential barrier is enhanced, electrons in the continuum that was winning kinetic energy are caught by the potential again, being driven back to the atom. Finally the step 3 at phase $\omega t = n * \pi$, for $n=1, 2, 3, \dots$. At $n = 2$ it is called "recollision process" of the electron. Where the electron can be caught by the potential again, and the excess of energy release another bound electrons, depending on the kinetic energy necessary [41]

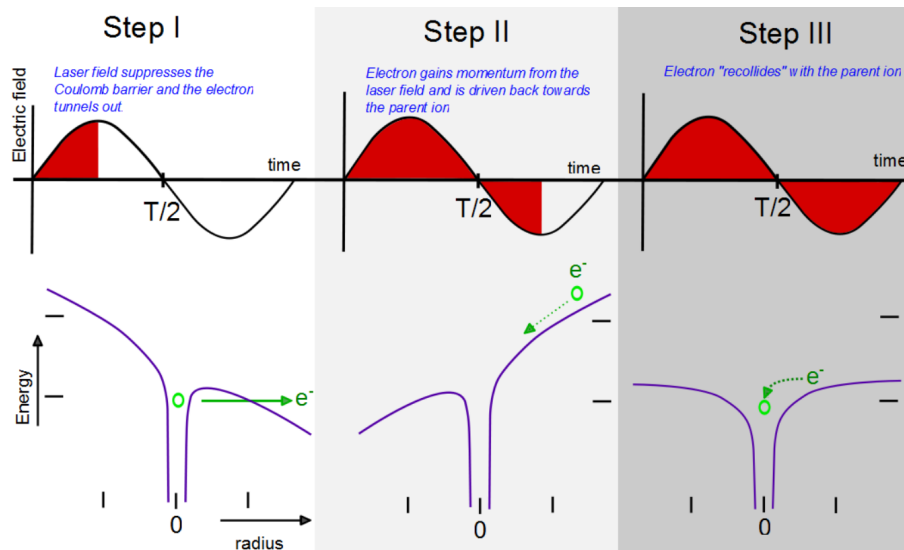


Figure 1.11: Recollision process at the three step model. Taken from [42]

If we transform the eq. 1.23 to laser intensities we will have $U_p = 9,33 * 10^{-14} I [W * cm^{-2}] \lambda^2 [\mu m]$. For a MIR-pulse with intensities $\sim 10^{14} W/cm^2$ and $\lambda \sim 3200 nm$ we have electron energies between one and a hundred of eV.

1.4.3 Cluster Ionization

Until now, we have described the most known ionization processes for single atom. But on cluster ionization, the dynamics are more complex and involve more parameters. Clusters are combinations of atoms or molecules which, depending on their species, are held together by Van der Waals forces, ionic bonds or metallic bonds. In this explanation we refer from now on only to He cluster, which mainly are just affected by Van der Waals attraction [65] and its interaction with the Laser Fields, specifically pulsed laser with a wavelength smaller than the cluster size, meaning

that all the atoms in the cluster are equally affected by the pulse, in other words the Field penetrates all over the cluster.

The first challenge to overcome when working with Helium, is its Ip. Being a rare gas, its ionization potential is higher than many of its doping molecules used. For example, under MIR lasers helium clusters need $I > 10^{15}$ W/cm², so TI or BSI is not the main process at the beginning of the plasma generation. Other interactions have to be explained in order to describe the process properly. This section we will be based on *Saalaman et. al* work [61] and *Grüner et. al* [28], for this purpose, we will divide the process in three phases or stages.

In the first stage called “*atomic ionization*”, the doping atoms are ionized independently of each other by the electric field at the leading edge of the laser pulse, it occurs mainly through inner ionization, especially on TI or BSI. The resulting free electrons acquire positive kinetic energy and have two options, leaving the cluster or they stay inside the cluster attracted to its positive ion core. After the first stage, the cluster becomes into an “ignited” nanoplasma, consisting of ions and quasi-free electrons, electrons that are free to travel inside the cluster volume but still not into the continuum [43].

The second stage is the *nanoplasma expansion*. During this stage the cluster is still interacting with the laser field, acquiring, by a large number of processes, energy by its atoms and electrons. Ions are further created by a combined force of the laser and other ions, the *ionization ignition* [28]. Quasi-free electrons oscillate, driven by the laser pulse and are heated to high temperatures. The heating becomes extremely efficient when the collective oscillations of quasi-free electrons become resonant with the laser pulse, Triggering a cascade reaction to more outer ionizations, freeing the remaining electrons in the cluster, this process is called *plasma resonance* [61].

After the laser pulse is over, the last stage starts. The ions continue to expand, in consequence, the radius rises as same as the cluster potential becomes smoother. So, it is easier for the highly energetic quasi-free electrons to leave the cluster, forming a coulomb explosion that destroys the cluster in a ions-electrons cascade. This process was first described by *Ditmire et. al* [15] combining high energetic collisions with cluster resonance absorption.

The graphic 1.12 shows on the left how the cluster potential is composed by the Van der Waals potential and atomic forces of the different atoms that compose the cluster. On the central images, additional to the atomic biddings, the electrical force due the ions in the cluster increase the potential, the laser pulse is still on and the quasi-free electron will gain energy while they are in this. Finally, on the right the laser field is off, the electrons have fled away and the cluster ion have been repelling

each other so the potential is reduced to the minimum(just atomic interactions.)

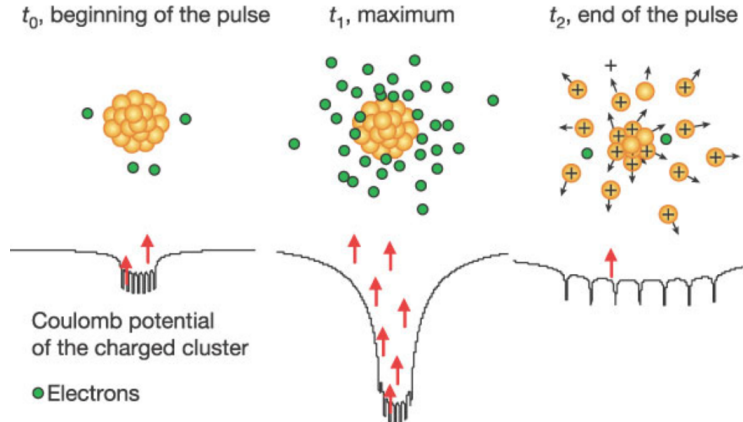


Figure 1.12: Cluster potential regimes. On the left, the atomic ionization starts the plasma formation. On the center, the quasi-free electrons auto-ionize the cluster, increasing the potential barrier and gaining energy due the laser field so a coulomb explosion can take place. On the right, The Coulomb explosion is finished, the potential is driven to it minimum and all the electrons and ions are ejected. Taken from [73]

Depending on the droplet size and the laser intensity, the Cluster can expand in two different ways. If the laser intensity is rather high and the droplet is small, a Coulomb explosion can occur. On the contrary, if the laser is not intense enough or the droplet is too big, a nanoplasma can be generated, therefore a hydrodynamic expansion will take place. Two forces are really important during the cluster expansion. Both act on the cluster during the phase two and three (during and after the laser pulse). The first, is the force associated with the free electrons with high kinetic energy. These hot electrons expand and pull the low energetic electrons and heavy ions on its pad [15]. The other force acting on the cluster is due to the inner cluster charge itself. The hottest electrons in the cluster will have a mean free path large enough so they can free stream directly out of the cluster, and, if the electron's energy is large enough to overcome the space-charge buildup on the cluster, they will leave the cluster altogether. If the charge buildup is sufficiently large, the cluster will undergo a Coulomb explosion [33]. According to Madison et all, a time scale for the laser pulse duration where the coulomb explosion can take place should be closer or lower to the femtosecond regime, depending on the element composing the cluster. [46]. Based on the laser power available on modern laser pulses, the same studies present that electron after a coulomb explosion can get kinetic energy up to 6KeV.

When the intensity is not enough to make the atomic bonds to break, the electrons

remain in the cluster forming a hydrodynamic expansion as a result of a conversion of electron-thermal energy to direct kinetic energy [20]. The effects that the expansion has on the electron temperature can be calculated by equating the rate of change of radial kinetic energy from the thermal contribution with the rate of change of thermal energy within the cluster. When this condition is fulfilled. The electron can present a resonance condition in the cluster, traveling in the space-charged forces formed by the plasma, winning enough kinetic energy until all the system collapse.

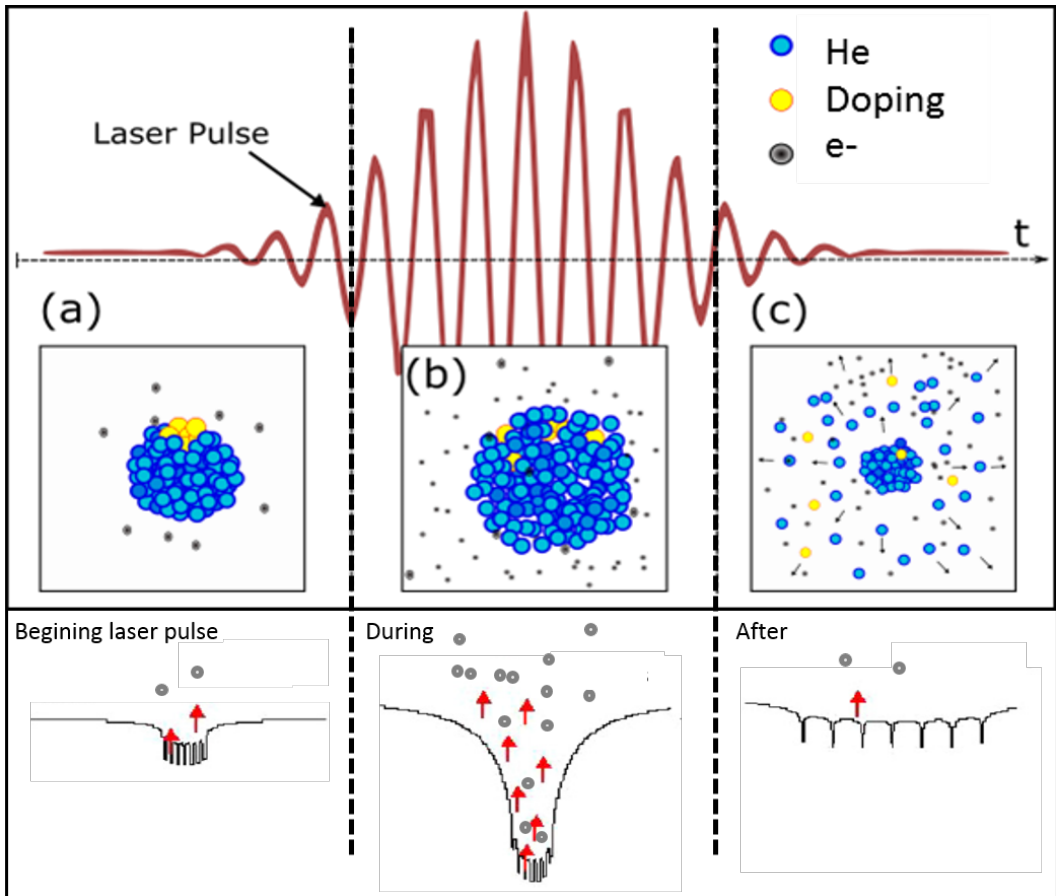


Figure 1.13: sketch of the Coulomb explosion for a doped cluster due the excitation of a pulsed laser field. At the beginning of the process the laser ionized the droplet, until some femtoseconds (up to 500fs) after, the system collapse and result into a coulomb explosion.

Although the two models are different in each regime, for example, at low kinetic energy or the beginning of the pulse, the Coulomb explosion produces less ions for low energies compared to the product on hydrodynamic explosions. Further, the number of high energy ion the coulomb explosion can create (although in less quantity) tent to be hotter ions too. We have to take into account that even the two processes are described for different laser regimes. Both processes can happen in parallel, but at certain energies is clear, that one or the other will be the responsible

at the end, for the collapse of the system.

1.4.4 Homogeneous Charge Sphere Model

Once the ionization process started, an electronic cloud of quazifree electrons will be created around the remaining cluster. This is a complex physical process due its chaotic system determined by the individual velocity vectors of the particles and their interaction between the Electric field, the cluster and each other. Various theoretical approaches ranging from phenomenological models [15] to large-scale microscopic calculations [61] have been done but far for been interpreted to clusters and system with more than a few thousand of particles. Additional a theoretical scenario of a single well-characterized cluster, irradiated by a laser pulse of a given intensity is usually far from the real experimental situation. An analytical solution is far from been formulated, we work joint to the theoretician Andreas Heidenreich to make computational simulations. This are demanding simulations that takes a large of computational power even for small cluster, the results can recreate reasonably the experimental system and so give a better background to the understanding of the plasma formation.

Another, more simple and intuitive approach is done by *Ranaul Islam et al.*, in [35] they try to express the kinetic energy distribution for an ion cloud. Two important assumptions are made for this model. First, we assume a uniformly charge distributed spherical cloud with radius R and density $\rho = N/vol$ where N is the number of particles inside the sphere, furthermore all the particle lays with zero kinetic energy. Second, The basic mechanism underlying the kinetic energy distribution in clusters is their Coulomb explosion, it converts the potential energy E_{coul} of a partially ionized cluster atom at a distance r from the cluster center into kinetic energy E . The probability dP/dr to find an atom at a distance 4 from the cluster center is then given by [35]

$$\frac{dP}{dr} = \frac{3r^2}{R^3} \Theta(R - r) \quad (1.24)$$

where, $\frac{dP}{dr}$ is the probability to find an electron at radius r and Θ is the step function for the particles inside the radius of the sphere, with homogeneous charged density, we have N particles with a charge of q and just after the are ionizes they have not moved yet, then the potential Coulomb energy of an particle inside the cluster is given by

$$E_{coul}(r) = Ne^2 \frac{r^2}{R^3} \quad (1.25)$$

for $r \leq R$. N is the number of electrons in the sphere and e is the elementary charge of an electron. A charged sphere like this will immediately coulomb explode and for $t \rightarrow \infty$ all coulomb energy is converted to kinetic energy, which can be measured experimentally with the VMI. It is possible to retrieve the energy distribution out of the spatial distribution 1.24 with 1.25 as the substitution formula.

$$dr = \frac{R^3}{2Nq^2r} dE \quad (1.26)$$

Furthermore, we define the maximum coulomb energy

$$E(R) := E_R = Nq^2 \frac{1}{R} \quad (1.27)$$

with all this follows the energy distribution of the electrons

$$\frac{dP}{dE} = \frac{3}{2} \sqrt{\frac{1}{E_R}} \frac{1}{E_R} \sqrt{E} \cdot \Theta(1 - \frac{E}{E_R}) \quad (1.28)$$

it can be seen, that the energy distribution is fully characterized by E_R , so it is enough to know the maximum kinetic energy, which is just the radius of the central feature in our VMI images. With this even the inverse Abel transformation can be bypassed, because the edge of a sphere is invariant for projecting the sphere on a plane.

With the formula for the homogeneous density in a sphere

$$R = \left(\frac{N}{\frac{4}{3}\pi\rho}\right)^{1/3} \quad (1.29)$$

and formula 1.27 the charge density in the beginning in the process can be derived to

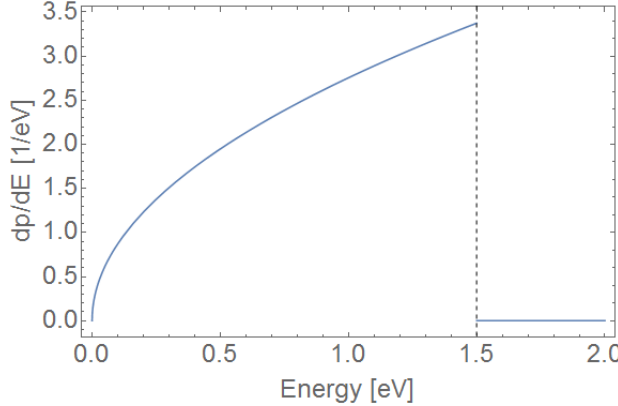


Figure 1.14: Energy distribution for a coulomb explosion of a full sphere of electrons according to formula 3.10. The dashed line marks cutoff energy E_R

$$E_{max}(N) = \underbrace{\frac{e^2}{4\pi\epsilon_0} \left(\frac{4}{3}\pi\rho\right)^{1/3}}_{=:B} N^{2/3} \quad (1.30)$$

and with this the charge density reads

$$\rho = 48\pi^2 \frac{\epsilon_0^3}{e^6} B^3 \quad (1.31)$$

In summary, the charge density can be calculated with the fit parameter B or B-factor as we will named from now on. B can be retrieved by plotting the maximum kinetic energy E_R as a function of the number of electrons N . Both can be extracted out of the VMI images, E_R from the radius and N from the brightness of the central feature.

2 Experimental Setup

In this chapter, we will present the experimental setup, giving special attention to the Nanodroplets generations, the doping process and the data acquisition system. A subchapter is also dedicated to the single shot correlation data acquisition system tested specifically for this Master's project. The apparatus we worked with, is part of the group of Molecule and Nanophysics at the University of Freiburg, Germany, and was calibrated and used for the experiments in [63] and [34].

In figure?? a sketch of the apparatus is shown. From left to right, the source chamber where the ultra-cold molecular beams are produced. The central chamber or "doping chamber", where the beam gas is doped via pick up process using a gas doping cell or a diffuse oven for alkalioids, where gases or thermally vaporized solids are used as dopants. The last chamber or "detection chamber", combines a VMI-TOF detection system and a Langmuir Taylor (LT) detector. To generate the nano plasmas, the apparatus was used in two different institutions, at the Max-Planck-Institute for Nuclear Physics in Heidelberg and the Extreme-Light-Infrastructure (ELI) in Szeged, Hungary, because of the laser systems that can be provided there.

The following sections describe the essential components of the apparatus and the new Triggering systems implemented to correlate the VMI and TOF signals. The structure is compacted to a length of about 240 cm long, each chamber has attached to its own turbo pumps with pre-vacuum scroll pumps and separated by valves and skimmers. On one hand, this enables to manipulate the vacuum in an independent way and control the targets in the "detection chamber". On the other hand, allows an optimum adaptation of the suction power of the pumps to the gas load of the individual chambers, as well as, to ventilate and open without having to disturb the entire system.

2.1 Source Chamber

The Source chamber consists of a 6-way CF vacuum chamber, with a 2-stage cryostat which powers a cold-head that can be cooled down to 9K. It is located at the entrance of the chamber, parallel to the floor with an attached conical nozzle for the gas

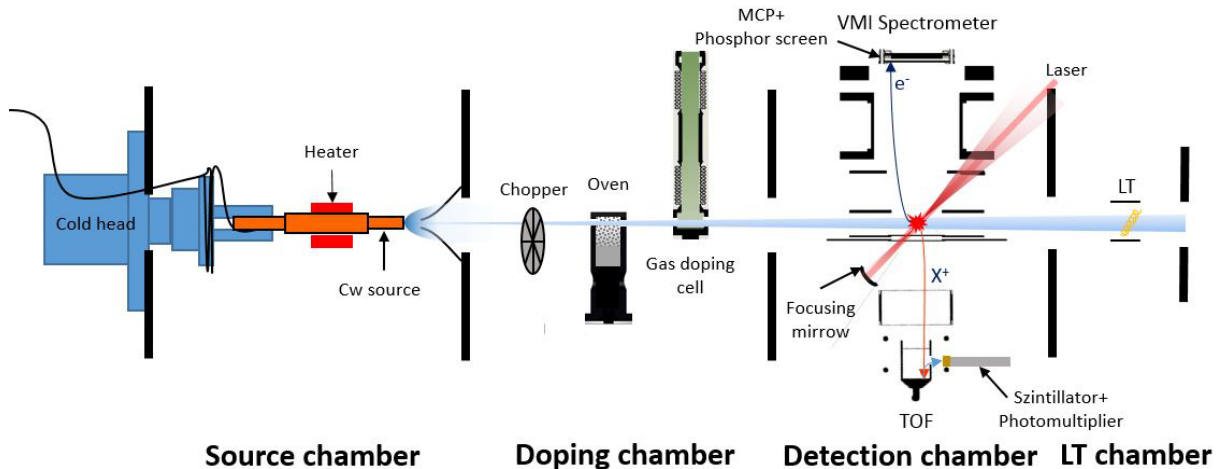


Figure 2.1: Sketch of the vacuum chambers, including the main parts of the setup

expansion process. The cooling capacity of the cryostat consists of a copper tube, into which pre-cooled helium is introduced. It can be adjusted by operating two heating resistors in combination with a sensor diode for temperature measurement and a PID controller. Controlling the resistor current the temperature at the end of the nozzle can be kept stable. The conical nozzle used to generate the atomic beam is the standard used in the research group on Nanoplasm research directed by Prof. Frank Steankeirmeyer at Freiburg University. It is made of copper and has a platinum plate in front with a hole of $5\mu m$ of diameter for He experiments and $15\mu m$ for Ne gas clusters. The diameters were chosen in order to follow the size dependence of the *Hagenas* law, which together with the adjustable gas pressure and the nozzle temperature regulates the flow. The cold head-nozzle arrangement are connected to the chamber via a self-made x-y manipulator, with a thermally insulating rubber ring, which allows a beam adjustment in relation to the other components in the setup without breaking the vacuum. At the bottom of the chamber an Agilent turbo pump of $1800L/s$ capacity is attached to a pre-vacuum scroll pump as exhaust. A skimmer with a diameter of $400\mu m$ is located in front of the effusive jet, sorting the gas beam not just by size but also by its velocity vectors, allowing just those beams with direction along Z. To adjust the nozzle optimally to the skimmer, it is connected to an x-y displacement unit and can be aligned from outside the vacuum chamber. To prevent the small opening of the nozzle from clogging over time, high-purity helium 6.0 (99.9999% purity) and Ne 5.0 (99.999% purity) are used, this clean gas ensures a constant gas flow through the nozzle. At this extreme temperature any impurity in the gas bottle can condense, blocking the nozzle or changing the conditions of the clusters formation.

2.2 Doping Chamber

As explained, the doping process takes place by inelastic impacts with atoms from the gas phase, referenced as the pick-up technique. In this experiment we doped with both metals and noble gases, and two different methods of doping are used: Metals are heated in evaporated phase in the oven, while gas dopant yield in a Gas doping cell entered the vacuum chamber through a needle valve. On the next section, we will explain the elements of the doping chamber and its most important characteristics used.

The oven chamber is connected after to the Source chamber via the skimmer, it is also a 6-way CF vacuum chamber, with a turbo pump on the bottom, connected to its own pre-vacuum scroll pump. On the sides the flanks allow a cold trap not used in this experiment, on the other side the flank that permit connection to the oven and the vacuum sensor. The Skimmer is made of Nickel, a very thin metal easy to bend, so in order to prevent strong pressure differences in the chamber that can modify the skimmer, a bypass is connected between the two chambers using a stainless steel flexible hose. An internal stand is welded to the front of the chamber and aligned with the skimmer. This stand supports the Chopper, the gas doping cell and the oven. In the front the rail the choppers is located. It is a steel disk with three notches uniformed located, two photocells around the bottom of the disk reads the position of the bottom notches so the upper one can be positioned right in front the skimmer. In this way, when the disk rotates the beam can pass or its block by the disk in a controlled way.

After the chopper, there is the Gas Doping cell, a circular flat metal base with a self-modified KF hose. The base of the cell has a matching pattern so the hose can be easily put and remove without losing the alignment. The stainless steel flexible hose has two 5mm hole (one in front and one opposite to it, some cm up the base) aligned to the skimmer so the gas bean can go though. The hose is fixed to the base and goes to the top of the chamber where it is connected to a "swagelok" needle valve that allows to control the gas flux for doping the beam. A Pfeiffer CMR375 Capacitive sensor is located after the needle valve so a better control of the pressures and the number of dopant in the cluster. The bendable construction allows, not just to remove the doping cell without difficulty, but also to fit it on the top without depending on a fix way to locate the top plank, in this way there is room for maneuvering and the installation is faster.

Finally, at the end of the rail lies the Oven. As shown in fig 2.2 the oven consists of a patterned base (similar to the gas cell) that can move a few mm on $x - y$ plane. Over it, a metal cylinder with 4 heating cartridges holds a movable crucible in the

center that contains the dopant sample, this movable container is set down by a rod that comes from the top of the chamber after a valve. Both, the stove and crucible have holes (a conical entrance of 40mm diameter and 3mm diameter respectively) that allows the pass of the gas beam and are aligned to the beam pad, in this way the passing Atomic beam takes dopants via collisions with the vaporized sample material.

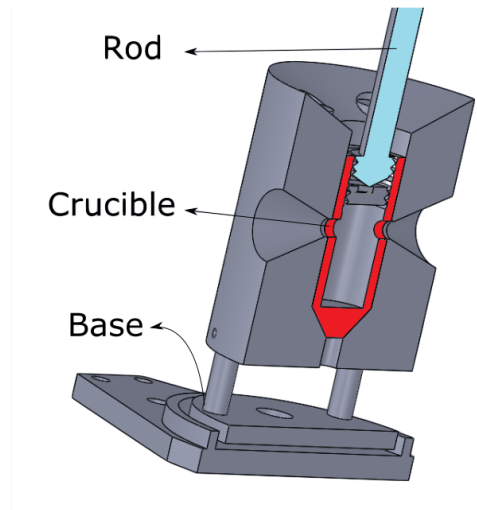


Figure 2.2: Cut of the Oven design, including part of the rod and the crucible.

One important advantage of this new oven design done by *Dominic Schomas*, is that the dopant can be change without braking the vacuum, it was tested in this experiment and prove to be useful in saving time and effort. To control the temperature of the oven a temp sensor is fixed in the stove, and the resistors current is manage by a PID controller allowing a stable temperature during the experiment. The maximal temperature reached was 450°C , enough to create the gas phase for the potassium K and calcium Ca used in this experiment. Finally, there is an extra skimmer of diameter 2mm, fixed to a valve between the connection of the doping chamber and the detection chamber that helps to avoid the disperse beams or an overflow from one chamber to the other.

In addition to the doped gas nano droplets, effusive gas is also released from the dopant chamber into the detector chambers through the needle valve and can be ionized and detected there. This disperse gas was pouring in directly on the chamber or filtered by diffused atoms going out of the oven and passing across the second skimmer once the choppers is close. This atomic gases were added for calibration of the detectors and background reduction allowing just one gas at a time.

2.3 Detection chamber

As mentioned, the detector chamber is connected to the Oven chamber through a valve and a skimmer. The detector chamber contains a newly developed Velocity-Map-Imaging Spectrometer on top, a time-of-flight mass spectrometer on bottom and a LT detector in front. In this section we will give a brief presentation of the VMI and the TOF used for this experiment, taking special interest in the new Triggering process that allows to detect single nanoplasma explosions.

2.3.1 Velocity Map Imaging Spectrometer

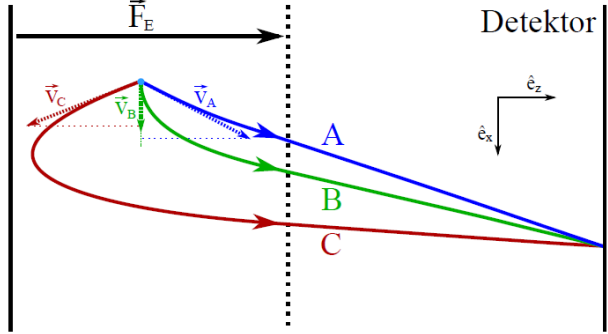
Velocity map imaging (VMI) is a widely used technique in areas such as atomic and molecular physics and physical chemistry. It is used to investigate velocity distributions of charged particles, which are generated in a defined volume, typically by photoionization. A laser pulse generates charged particles by photoionization in the interaction region, which are accelerated by an electric field created by two electrodes. The VMI used in this experiment is a modification on the original design by Eppink-Parker [19]. Its is made by a lower electrode called Repeller followed by the extractor, ground electrodes which generated the electric filed that drives the particles to a detection system consisting of an Microchannel plate or MCP and a Phosphor screen, which is observed by means of a CCD camera on top. All electrodes have a circular layout and are about 1mm thick. The extractor and ground electrodes have a concentric hole where the particles pass through. Once the Electron or Ions, guided by the electrodes, arrive to the MCP an electronic avalanche occurs, increasing the signal of each individual particle. The electronic avalanche hit the Phosphoscreen producing photons that can be detected with the camera focused on top.

Velocity distribution in VMI

In order to describe the velocity distribution detected by the VMI, we assume that the charged particles come from a point in space emitted between the Repeller and the extractor. Furthermore, we presume that the initial kinetic energy of the particles obtained during the ionization process is small, in comparison to the energy supplied by the electric field. The initial conditions of the charged particles are determined by the ionization volume and the initial velocity vectors $v_i = (v_x; v_y;$, whose distributions are of interest. The particles are drive by the Electric field in the direction v_z to the spectrometer axis. If one starts from an isotropic initial distribution for the velocities, particles with differing initial velocity vectors can

finish in the same point on the detector, as shown in fig 2.3. This results in a loss of information, its is expected because we are trying to 3D information from a 2D projection.

Figure 2.3: Representation of particle trajectories A, B and C of the ionization volume to the detector plane, which, in spite of initially different velocity the finish on the same point of the detector plane. Withdrawn from [21]



Assuming a cylindrically symmetric distribution $f(r, y)$ along the y -axis. If an infinitely far away observant look at the distribution F along the z -direction. With a basic axis conversion it can be shown that along the Z direction, the projection of the distribution F of the integrated signal respond to.

$$F(x, y) = 2 \int_{|x|}^{\infty} \frac{f(r, y)r}{\sqrt{r^2 - x^2}} * dr \quad (2.1)$$

Been F in cylindrical coordinates and $r^2 = x^2 + z^2$. Also called *Abel-transform*. But in order to resolve our signal we need the opposite procedure, turn this 2d distribution into the 3d spherical distribution that we assume in the beginning. For this process is called *Inverse Abel-transform*, and it can be shown as.

$$F(r, y) = \frac{1}{\pi} \int_{|x|}^{\infty} \frac{dF(x, y)}{dx} \frac{1 * dx}{\sqrt{r^2 - x^2}} \quad (2.2)$$

The main problem that carries this transformation is that is not resolvable to a non-continues distribution that is the case of the Images recorded by the camera. So a numerical method needs to be used. Fortunately, a Software PbaseX, is available to solve this integral. The idea is to have a basis function f_k (in this case Lagrange polynomial) in the space of distributions f . Their projections F_k onto the detector are well known, and the Able transform will be set as:

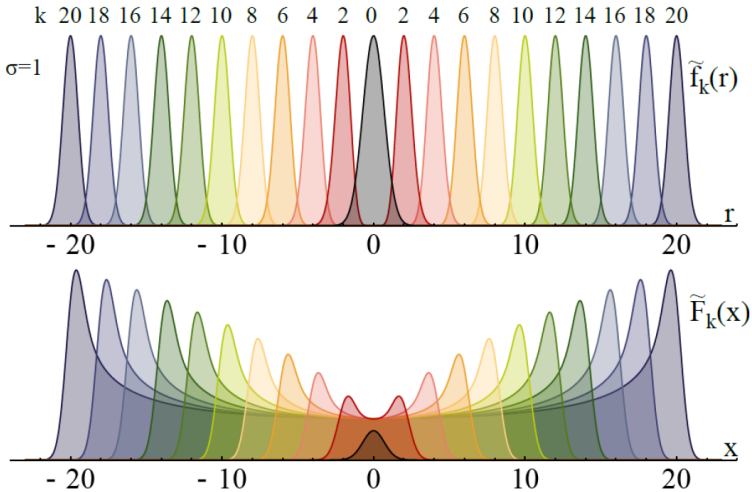
$$F_k(x) = 2\sigma\rho_k(x) \left\{ 1 + \sum_1^{k^2} \left\{ (x/\sigma)^{-2l} \prod_{m=1}^l \left(\frac{(k2+1-m)(m-1/2)}{m} \right) \right\} \right\} \quad (2.3)$$

VMI	Repeler	Extractor	Lens
X1	-2430	-1940	3500
X3	-7290	5820	10500
Ion	2430	1940	0

Table 2.1: Typical voltages for the different VMI settings

If every measured image can be expressed on this basis, then the reconstruction of the F distribution when $k \rightarrow \infty$ can be obtained. A graphical example of this transformation is given in fig ?? where each color represents a f_k projection, where all f are in the same basis, the sum of all the different f will set the final reconstructed F_K .

Figure 2.4: At the top of the graphic some basic functions f_k in different colors, which can be used for the Inverse-Abel transform in the Basex method. On the bottom, the corresponding Abel-transformed functions \tilde{F}_k . Taken from [21]



VMI Parameters

The VMI detector used in this experiment is detailed in [63], this construction basically follows the standard geometry of Eppink and Parker [19]. It is composed by three electro lenses (Repeller, lens and extractor) that focuses the ions or electrons on a 86,6mm (effective area) diameter Micro channel plates (MCP) arrange. This detector set is basically two MCP's superposed, rotated to each other and a phosphoscreen (PS) layer of same diameter facing the top plank of the chamber with a Ca-fluoride glass of 1mm thick. An external CCD camera is focused to the PS.

The voltages applied to the MCP and PS determine the brightness of the final pictures of the ions, so in general just one set of voltages has been used, around

1400V for the MCP and 4000V for the Ps. The achievable energy acceptance for this stack is $34eV$ for a the VMI setting 1 and $270eV$ for the X3 settings. The VMNI have a resolution of $\Delta E/E \leq 4\%$ [63]. The camera used in the experiment was a Basler acA1920-155um focused on the PS.

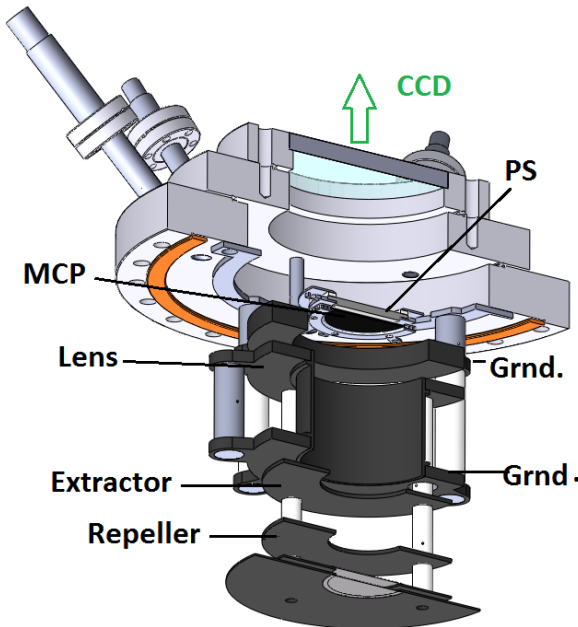


Figure 2.5: Sectional cut view of the CAD model of the spectrometer setup. On black, the electrodes and the white the Polyether ketone (PEEK) isolators. On orange, the cooper ring and on blue the top window facing the CCD camera

On fig ?? we present a view of the model of the VMI used in this experiment, From bottom to top, the structure of the electrodes consists of two Repeller electrodes separated by a few millimetres with circular openings on which a fine mesh copper grid is applied, an aperture electrode as Extractor, another aperture electrode which is held at ground potential and then from the extended lens electrode with the following second ground electrode. At the top, the MCP-PS arrange (on black the MCP and on gray the PS) facing the center of the window installed in the top plank of the chamber. Around the window there are three connections that allow the voltages for the electrodes and the cables are carefully arranged around the structure to avoid discharges or even disturb the uniform electric field.

The openings of the Repeller (at the bottom in bluish color) electrodes allow the use of these electrodes as well as extractor electrodes for a TOF spectrometer. In simultaneous operation of the VMI and the TOF spectrometer, the glued grids prevent mutual field effects of the two spectrometers. The Repeller and extractor are grade 2 titanium and the lens is stainless.

2.3.2 Time of Flight Spectrometer

The Time of flight (TOF) spectrometer used was based on the design by Wiley and McLaren [76]. As its name refers, the TOF mass spectrometer relates the time that a particle at an electric field requires to reach certain distance with its mass, when atoms and molecules are photoionized, they pass through an electrostatic acceleration field and are registered in a detector after crossing a field-free flight path. Based on the flight time the ratio m/q of a particle can be determined as:

$$t - t_0 = a \sqrt{\frac{m}{q}} \quad (2.4)$$

Where a is an experimental factor depending of the flight distance, electric fields and material of the setup, m/q is the relation mass - charge, t_0 is the time ionization time (given by the laser)and t is the time of flight.

The ions creation takes place in the aperture between the Repeller and extractor electrodes. Behind the extractor electrode there is a further aperture electrode, which is held at zero potential and thus generates a pre establish flight route with a defined field, grids are glued to the openings of the electrodes to prevent the propagation of the fields through the orifices in the electrodes. The Repeller electrode is set to a positive potential and the extractor to a negative potential. The resulting electric field accelerates the ions through the openings in the flight tube, on which grids mount on both sides keep the drift path free of field. Once the coulomb explosion takes place, the ions are accelerated by the electric field of the Repeller and then fly through a field-free drift path to the detector. This allows a complete mass spectrum to be recorded within a few microseconds in a single measuring step [48].

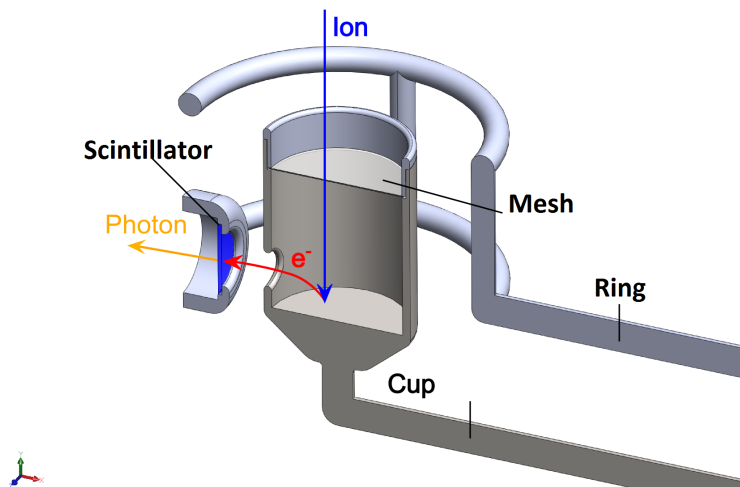


Figure 2.6: Illustration of the functional principle of a Daly detector.

The flying Ions finally are detected by a Daly detector [12]. It consists of a cup, a grid and a ring. The cup lies on negative high voltage while the ring for positive. The ions from the Repeller pass through the field free tube corrected by a drift electrode. Since in the direction of the hole the potential for electrons drops sharply, the ring electrode generates an electric field, which directs the ions into the cup. The ions that pass the grid at high speed hits on the bottom of the cup, they generate some electrons, which are transmitted through a small hole in the bottom and then in a scintillator Eljen technology (EJ-204) flashes some photons in the process. These light is detected in a Hammamatzu r-647 photomultiplier (PM). The voltage output of the PM is controlled by a fast analogue-to-digital converter, and it is used at 900V voltage. The cup and the drift-scintillator tube was set at high voltages, $-17000V$ and -4000 respectively.

2.3.3 LT Detector

The Langmuir-Taylor detector (LT detector) chamber consists of a small CF40-6-way chamber. The detector consists essentially of an annealing filament, which is located between two planar round electrodes. The Operating Principle of an LT-Detector is based on surface ionization by the tunnel effect [14]. For the annealing filament is typically used rhenium, platinum or tungsten, as this is the most common due its comparatively high electron work function. With high voltages, the wire reaches high temperatures, as a consequence, a passing neutral atom is ionized, releasing an electron into the wire. The resulting ions are attracted by the negative electrodes around the wire generating a current. The ionic current generated at the electrodes is proportional to the number of ionized atoms and is measured using a picoammeter. The LT chamber is connected to the VMI chamber via an orifice plate and is used mainly as a beam dump and to align the detector. The most current generated in the chamber the most atoms are passing through the hole, so we can be sure that the beam pad is in the detection area.

3 Data Acquisition and Calibration Methods.

Taking advantage of the possibility to record individual signal in the TOF and the VMI spectrometer, we develop a method in which the data of both detectors is correlated to describe a single coulomb explosion. The large exposure time of the camera and the software limitations required the use of a trigger protocol in order to collect and sort the signal coming from a single laser shot. The next section present the triggering protocol developed for the ELI-Alps beam time, together to the calibration methods used for the VMI. In addition, in our experiment, in contrast to other spectroscopic techniques, the Photoelectric Spectra (PES) of the $e-$ VMI looks different for each signal because of the size distribution of the clusters production and the different focus intensities each cluster is exposed to. Nevertheless, the images and therefore the PES look rather similar in shape, small circular boops in the middle of the detector with a clear edges and a brightness higher than the background. The larger clusters ($\langle N \rangle = 10^6$) present small deformation in the circles as show in chapter 4. For example, some images show small-medium uniformly bright circles while others signal, shows high intensities in the edges and lower in the center, like a "donut", as we will refer from now. In section 3.3 we present the Data protocol and the algorithms used to detect, sort and analyse the acquired signal.

3.1 Camera and Trigger Protocol

One of the main objectives of this project, is to record individual data for single shots nanplasma explosion in the VMI and TOF. The advantage is the ability of the threat the data in a separate way to reduce the background and know the energy distribution information that is lost when data is averaged.

Two methods were developed. A first approach was done using a software triggering for the CCD camera and the oscilloscope, an Acqiris Card CC103, for the TOF. Using Lab View, an external clock (a RaspberryPi 3) was triggered by the laser, the beginning of the explosion, at the same time, it software-trigger the cam-

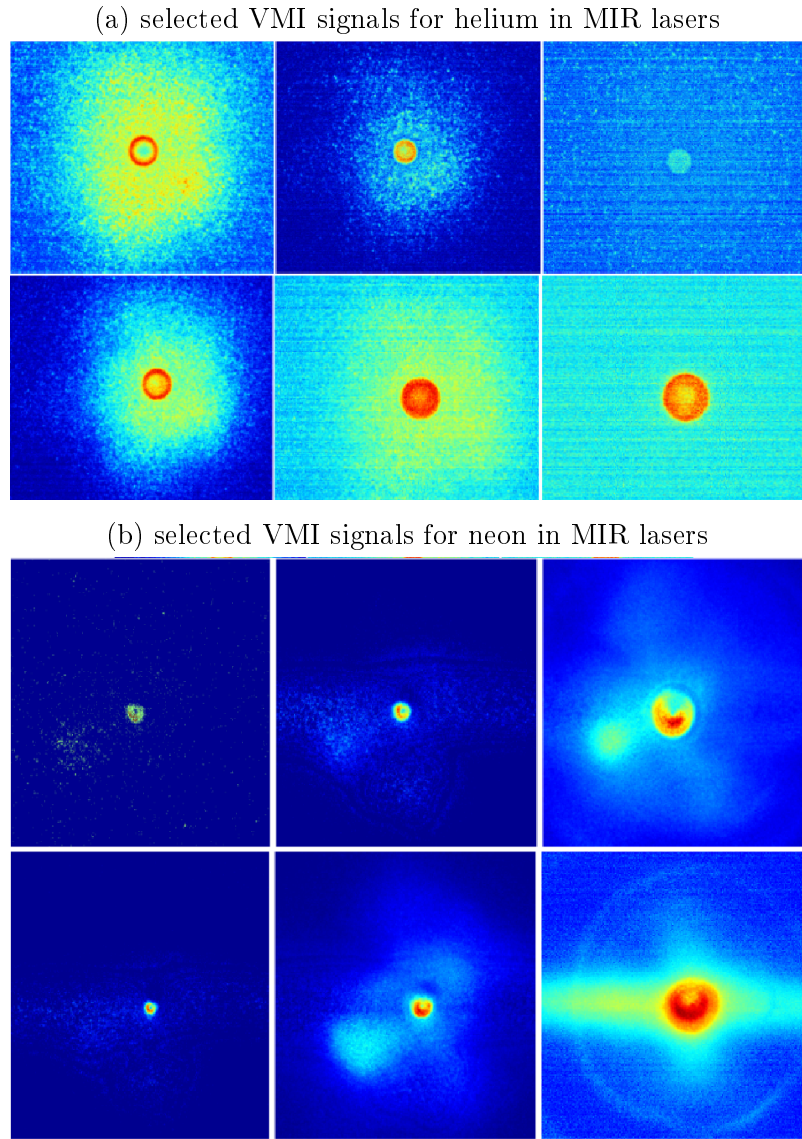


Figure 3.1: Example images of MIR VMI signal in He and Ne with different parameters. On the top, several example plasma signal including, low intensity and the donut shape. On the bottom, random example for Ne signals, including low signal and non-uniform bloops.

era and oscilloscope programs to start the acquisition. Having all the data acquired in the same software would allow to sort the data online and reduce the storage needed for the experiment. The Lab view program was tested unsuccessfully for the data acquisition rate needed in ELI 100 KHz, the main problem was that when a software-triggering scheme is used, extra delays are applied due to the operating system and the communication protocols, so even the data were acquired at the same time the delays at saving the information it in the hard drive made impossible to correlate the signals.

List delays	
Channel	Set to:
A	$T + 0$
B	$T + 1\mu s$
C	B or $B+6 \mu s$

Table 3.1: Trigger Channel delays

Based on that same idea, a second approach was used. As alternative of the software triggering, a hardware triggering was used. The laser triggers a delay generator that at the same time triggers the oscilloscope, a *R.S RTO2000* with bandwidth of 600MHZ to 6GHz, and the camera. Two facts need to be taken into account, first, the minimal exposure time of the camera is $34 \mu s$. Second, the timing between the camera receiving the trigger signal and the real start of the acquisition is not negligible as it is for the oscilloscope. The camera took 5-6 μs to start after the trigger was sent. To solve this problem the triggering scheme in Fig. 3.2.

A delay generator (Stanford Research Systems MD DG335) receives the laser trigger (100KHz), channel B and C were connected to the oscilloscope's channel 1 and 2, channel A was connected to the pin 1 (trigger) of the camera. Due the limitation in the exposure time of the camera, we cannot identify a single laser shot with it. Table 3.1 shows the delays used in the experiment, where T is the original laser trigger and A, B and C are the channels in the delay generator. The oscilloscope can identify each individual laser shots but the camera will see at least 3 shots. Fortunately, not all laser shots generates signal, the signal rate oscillates between 3 to 10% of the total images, this mean that most of the pictures will have no signal, rare cases will have two or more, but the majority of the pictures with signal will contain just one explosion in the VMI that can be correlated to its individual TOF signal.

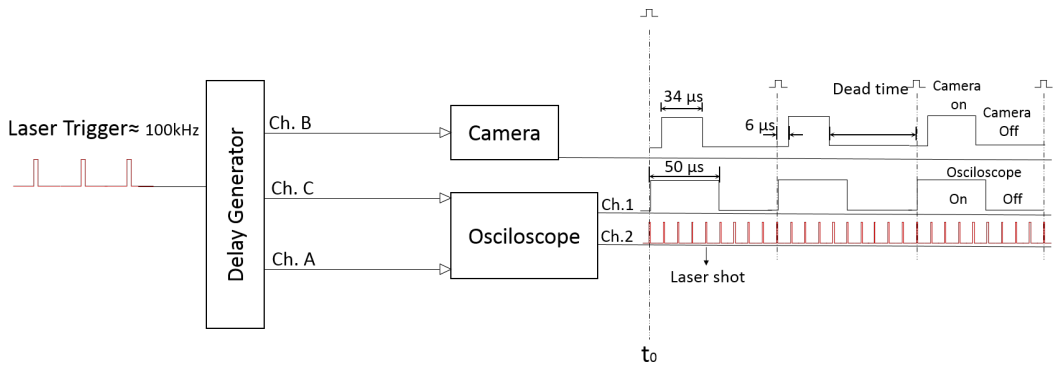


Figure 3.2: Scheme of the trigger system used.

In Fig 3.2, we show the Trigger scheme used in the experiment. The oscilloscope and camera are triggered by the delayed channel B. The oscilloscope is set to $50\mu s$ and the camera to the minimal exposure time. So the camera and oscilloscope sees the same trigger, the oscilloscope will record at least 5 laser shots, but the camera because starts later just can see three as shown. The pictures are saved in the memory RAM of the computer so the dead time after the camera is off is mandatory to give the operating system enough time to save the data on disk and don't get out of ram. A small improvement in this system can be done if we trigger the camera with B and the oscilloscope with C, so both apparatus can start almost at the same time and no corrections need to be done. Each of the data set is save with a unique label to correlate the signals after. Once an explosion is found in the VMI pictures, we check in its corresponding TOF that to proof there exist just one explosion in all five laser shots, so we can be sure that picture correspond to a single coulomb explosion, in case more than one signal is found, this picture is discarded. Fig 3.3 shows an example of some electron-VMI pictures to its corresponding TOF. Fig A shows a typical VMI-TOF relation with one peak in the time of flight for ^{+}He . Fig b. presents a brighter electron VMI picture meaning a bigger explosion as seen in the TOF. Fig c. show an example of a Coulomb explosion where dimmers where formed as show in the TOF with two peaks that correspond to ^{+}He and He^2 .

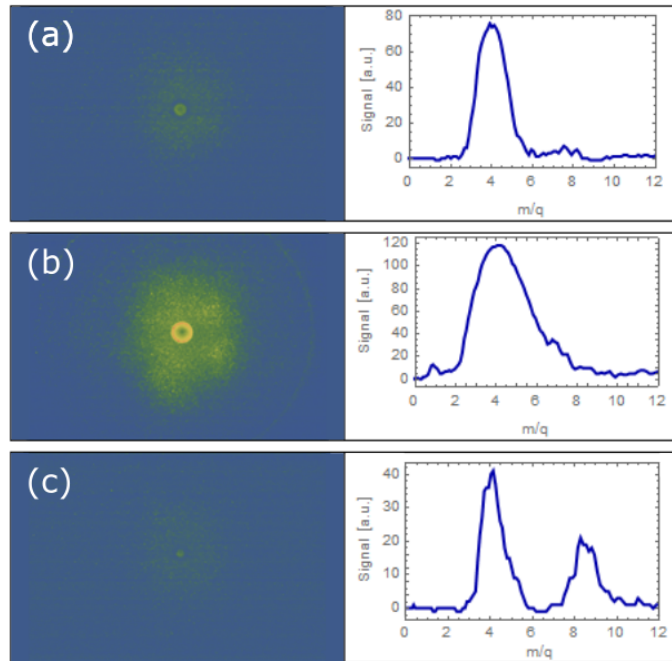


Figure 3.3: Example of VMI-TOF correlation signals for He droplets, in the left some Electronic VMI pictures and on the right their correspondent TOF spectra On the Y-axis the Ion yield and on the x-axes the mass/charge

3.2 Calibration Methods

3.2.1 VMI calibration

To calibrate the VMI spectrometer, two different methods were used. A quadratic calibration function $E = \alpha \cdot r^2$ is used, where E is the kinetic energy of the particles and r is the measured radius. This function is chosen because $E_{kin} = 1/2 \cdot mv^2$. In order to keep the simplicity, stray fields, third order or linear terms are not included, as long as the calibration curves fit well with the measured.

On one hand, the most independent method is the trajectory simulation, because it does not rely on any laser system or physical process. These simulations were done by Dominik Schomas with SIMION 8.1. For the starting conditions for the electrons we chose a small interaction volume comparable to the estimated experimental parameters and the emission direction perpendicular to the spectrometer axis. For those electrons the projected energy on the detector screen is equivalent to the real kinetic energy, with this the inverse Abel transformation can be avoided. It is necessary to simulate different kinetic energies for the electrons, at different velocity vectors. After extracting the radii, where the electrons hit the detector plane, a calibration from pixels to mm for the camera is needed, because SIMION gives the radii of the electrons in mm. To do so, known distance in the camera image is needed, for example the inner diameter of the phosphor screen, making possible to generate the fit curve. The disadvantage of this method is, that it is very difficult to include any magnetic or electric stray fields into the simulations or other external parameter that can be in reality.

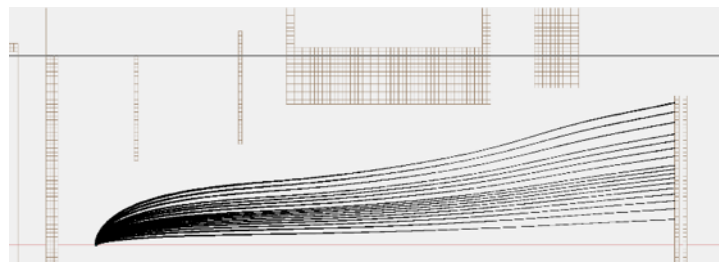


Figure 3.4: energy calibration of the VMI spectrometer with SIMION. Electrons with discrete kinetic energy are emitted perpendicular to the spectrometer axis.

On the other hand, in order to contrast the simulation, a physical process is used, creating electrons with a well-known energy, then above threshold ionization (ATI) of rare gas atoms is a suitable method to calibrate the spectrometer. The result of the ATI mechanism are several rings in the VMI along the laser polarization axis

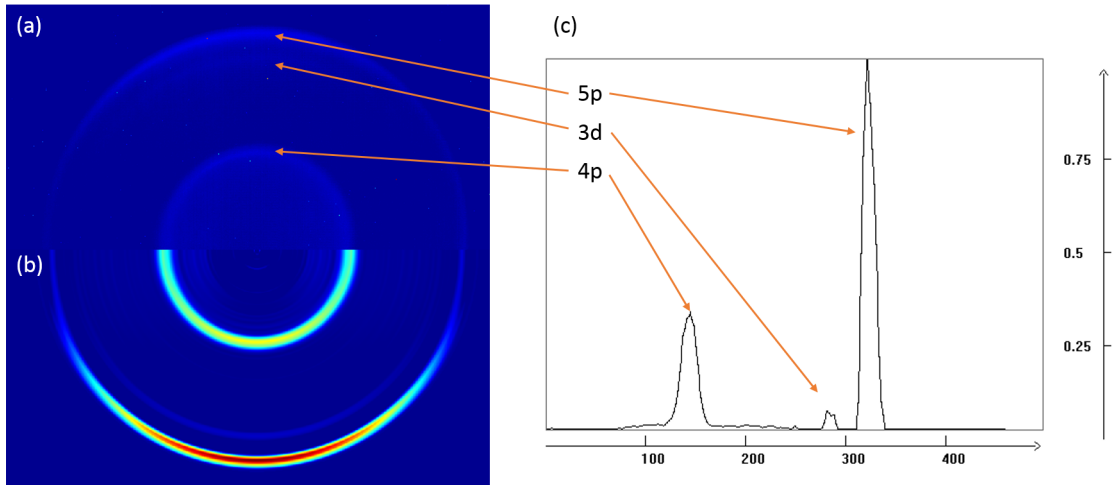


Figure 3.5: (a) Photoelectron image of potassium excited and ionized by linear polarized 404nm light, (b) Abel inverted image and (c) corresponding photoelectron spectrum, not yet calibrated on the energy

that are energetically spaced by the energy of one photon. With at least 2 rings visible it is possible to do the calibration with the following formula

$$\Delta E = \alpha(r_2^2 - r_1^2)$$

where ΔE is the photon energy, r_i are the peak positions of the Abel inverted rings and α the calibration factor. Best results are achieved by using as low peak intensities as possible, so tunnel ionization is suppressed.

Another method to calibrate a VMI spectrometer is the use of a narrowband laser in combination with resonant processes. A very useful scheme is published by *Wituschek et al.* [77]. The scheme uses continuous 404 nm laser light to excite either the $5p_{3/2}$ or the $5p_{1/2}$ state in potassium. From this state, relaxation in four other states and the ground state is possible. The 404 nm light can also ionize electrons from the resonant 5p state, the 5s, the 3d and the 4p states. The resulting electrons carry a very well defined kinetic energy $E_{kin} = E_{Photon} + E_{state} - E_{ionization}$. Since all energies on the right side of the equation are well known, the kinetic energy is also well known. This allows the calibration of the spectrometer with three points (the cross section of the 5s state is too small to see it) in the low energy range.

3.2.2 Laser Intensity Calibration

When using a focused MIR and NIR laser, it is essential to know the peak intensity in the focus of the laser field. Most of the time calculations give wrong results, because they assume a perfectly Gaussian shape and do not account losses in optics after the power measurement or an imperfect focus. So it would be desirable to avoid calculations and measure the peak intensity directly. In this thesis two different schemes are used, the $2U_P$ cutoff energy of electrons in a laser field [?], [2] and the ratios of charge states of ions produced in the laser field [5].

Assuming that the laser is a perfect Gaussian beams we can calculate with linear optics the Focused intensity. In cylindrical coordinates with the origin in the focus of the beam where z is the direction of propagation and r the distance from the z -axis one can use following equations to describe the intensity distribution of the beam:

$$w_0 = \frac{f\lambda}{\pi\omega} \quad (3.1)$$

where w_0 is the calculated focus depending on the focal length of the focused mirror f , the wavelength of the laser λ and the radius of the collimated beam before it is focused. the intensity will red as

$$I_0 = \frac{2P}{\pi\omega_o^2 R\tau} \quad (3.2)$$

where P is the power of the laser, R is the repetition rate and τ is the laser pulse duration.

3.3 Data Analysis

Due the complexity of the coulomb explosion, few analytical models exist in literature. the variables and parameter in which the nanoplasma depends are several and its analysis can be quite complicated. As shown above, the individual signal tends to have a well defined circular shape that can be advantageous to our analysis, Fig. XXX shows a picture of the normalized sum several signals for helium at 10.6 K and have a similar behaiiur for the other experiments. On the left, the corresponding kinetic energy distribution after doing the inverse Abel transform in PbaseX software. As see, there exist a large combination of energy available along the plasma production and can be comparable to the most recent work of Kelbr *et al* [?], where the electron spectra show similar values.

This large range of spectra for the averaged data and the defined circularity of the

individual signal make us suspect that exist a energy dependence. Fig. 3.6 show a raw picture of single event and its Abel transform. The sharp peak in the electron spectra show a strong electron energy preference that change in each explosion. The peak in the energy distribution define the radius of the signal. To avoid doing the Inverse Abel transform for each individual picture, we create a event finder algorithm to identify and analyse each signal in the data sets. In this way we will detect and analyse the max energy distribution in the nanoplasma for the single explosion, and correlated to the electron yield given by the intensity of the signal.

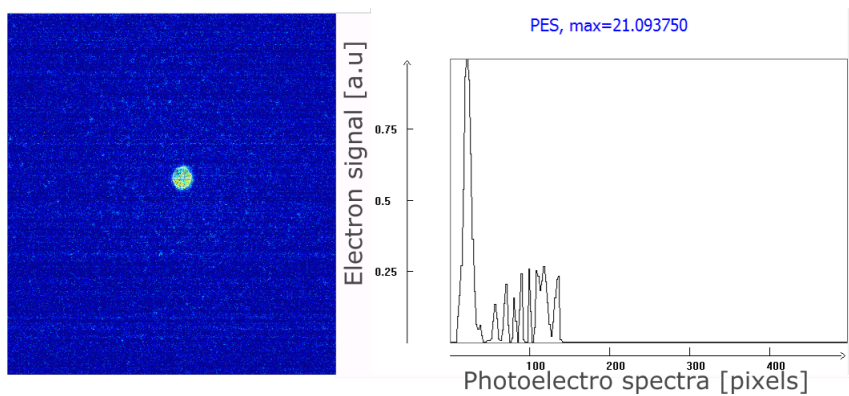


Figure 3.6: Example of the Inverse Abel transform for a single shot image. The photo electron spectra show the energy distribution of the signal with a peak in 21 pixels

In other words, Our result will be based in the finding and analysis of the Max radius and brightness of each individual bloop signal. The next section shows the event recognition scheme and the radius finder algorithm.

3.3.1 Event Recognition

The low event rate of the nanoplasma explosion results in a lot of empty VMI images. On average 10000 pictures were taken for each set of data where less than 10% of them contain signal. To separate empty images from signals, the central bright bloop is used. A center is selected manually and all pixels within a region around the center are summed up. If the sum is above a certain threshold value the image contains a signal. To analyse the central feature in more detail the size and the brightness of this feature is of importance. To determine the radius and the brightness, two methods were compared, one using the Mathematica 10.1 (wolfram inc.) algorithms and the other using a binning processing.

First, the ImageMeasurements and Componentmeasurements algorithms in Mathematica act, over binarized images, works with arbitrary 2D and 3D images and

computes multiple properties, finding components bases on a specific matrix. For this special case, a circular matrix with the specifications of minimum radius and no share edges were given as parameters. The efficient of this process was demonstrated to depend strongly on the initial image and the signal-noise rate, hence, a recursive function were develop to change the binarized threshold recursively until the algorithm find just one object that matches the signal. The threshold was changed progressively and modifiable steps in order to get the most precise fit. Once the object is found, the radius and center are saved, and sum the total intensity inside the radius, so a Radius-Brightness measurement is complete for each individual image.

The second method was based on a circular binning of the signal. A center for each data set is manually place after summed all signal pictures and find the center of the signal bloop, set to be in the same position within one measurement. Three circles are defined around this center, the first one with radius r (in pixels), which is variable, the second one with $r_{in} = r - \Delta r$ and the last one with $r_{out} = r + \Delta r$, where Δr has to be picked out from the dataset. The three circles define two areas A_{in} and A_{out} , see Fig 3.7. An average pixel value ρ for both areas is defined via

$$\rho_{in} = \frac{1}{N_{in}} \sum_{px \in A_{in}} \text{value}(px) - bg \quad (3.3)$$

$$\rho_{out} = \frac{1}{N_{out}} \sum_{px \in A_{out}} \text{value}(px) - bg \quad (3.4)$$

$$(3.5)$$

Where N is the number of pixels in the respective area and bg is a background taken far from the central features. The normalization on the area is important, because the areas are of different size. To finally find out the radius of the central circle, the difference $\rho_{in} - \rho_{out}$ is maximized, this is the case for the orange box in figure 3.7. For the green and the purple boxes $\rho_{in} = \rho_{out}$, which gives zero for the difference. Real signals do not have a perfect cut-off or a constant radial profile, which leads to noisy curves, when Δr is chosen too small, which makes the determination of r difficult. An example of a single shot image, where the radius is determined for $\Delta r = 3, 4, 5$ in pixels, is shown in figure 3.7. The VMI image in this figure has a donut shape, if the inner radius is of interest the same curve can be used to determine the inner radius as well if the minimum of the function is taken.

As shown in 3.7, the density difference have a summit in two cases, one when the inner our outer density changes signs. The lower peak, when exists, refers to the change from a low density change to a high one, besides the higher peak, describe the

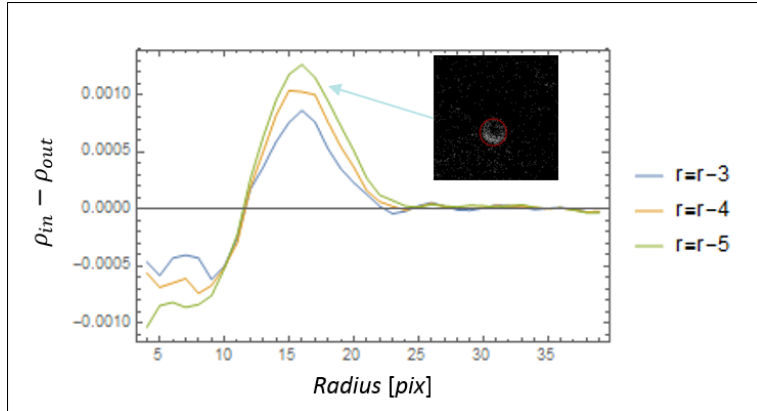


Figure 3.7: Difference of mean pixel values to determine the radius of the central feature in the VMI images

change from a high density to a lower, setting the radius where the edge of the bloop is pointing out that not all signals have the donut shape so this case was just added when needed. Finally, as in the last procedure, the inner pixels in the circle with radius r are summed and the radius-Brightness is save for all signal. In the case, as the example, where the second inner circle is clearly identified, the sum of all the pixel discard the inner are, and at the same time, adds the inner radius-brightness measurements to it. Fig 3.8 shows a raw image where the inverse Abel transform and the Binned Finder algorithms where compare. The signal shows a clear edge where the peak electron signal (PES) of the Abel transform is at 58.6 pixels, while a similar curve is described by the density binned plot of the Finder algorithm at 60 pix, given a good agreement between the two techniques. Figure 3.9 shows a set of well fitted radius for each signal, proving the good efficiency of the algorithms.

Last, once the radius-brightness data is recorded, and the calibrations are set, the system can be compare to the model explained above, where radius can be converted into maximal kinetic energy, $r \rightarrow k_{energy}$, and brightness to number of electrons, $b \rightarrow N_{e-}$.

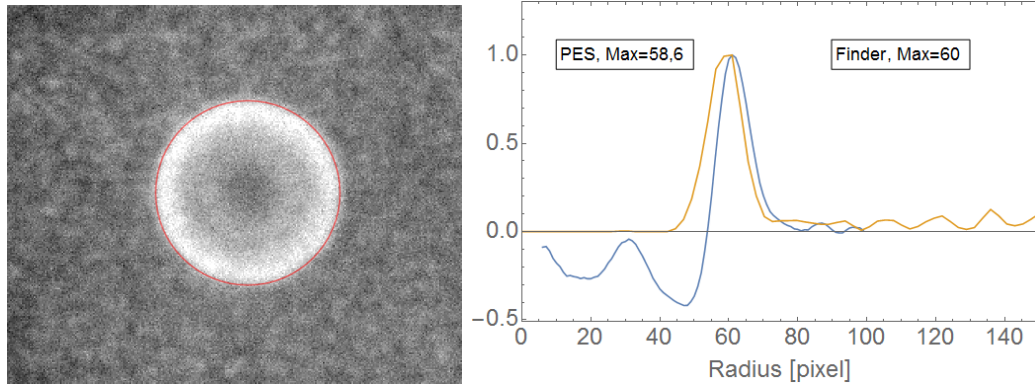
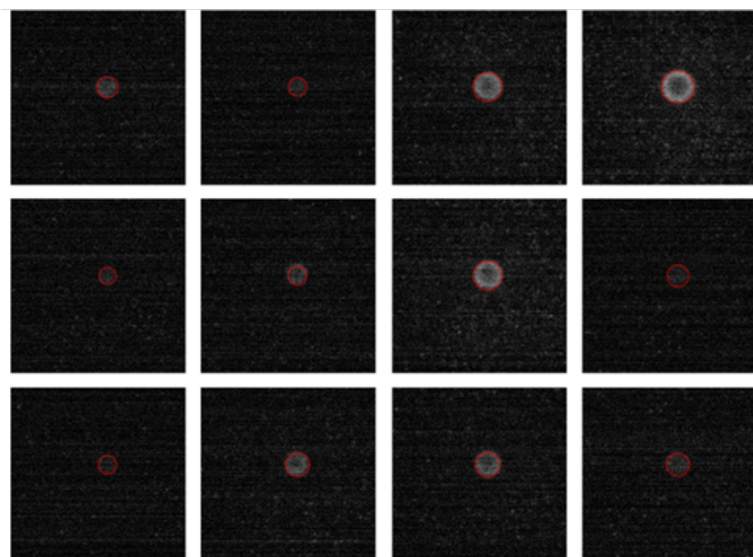


Figure 3.8: On the Left, example images of MIR VMI signal. On the right, the correspond Inverse Abel transform PES (orange) and the Bloop finder density plot (blue). Both algorithms show a peak at radius of the circular signal, highlighted in red. The density plot also shows a second depletion close to 45 pixel that give extra information as the radius of the inner less brighter ring.

Figure 3.9: Example of random signal images fitted to its corresponding radius.



4 Results

This experiment was performed in two laser facilities. At The Extreme light Infrastructure-Attosecond laser pulsed source (ELI-ALPS) in Szeged, Hungary, and at the Max-Planck-Institute for nuclear physics in Heidelberg, Germany. Several studies have been performed in He droplets and its charging dynamics driven by embedded xenon cluster ignition in strong laser fields using field free-TOF to detect the electron spectra [?] [?]. Similarly, studies using time-of-flight mass spectrometry for neon or Ar clusters that were exposed to intense free electron laser pulses [?] [?], But almost none research in strong MIR laser pulses.

In the first section we will present the results for Helium cluster in NIR field. The Experiment was done in Heidelberg with a Ti-Sr 800 nm wavelength laser. An intensity scan, Droplet size dependence and Xe doping dependence are investigated. The second section will show the results of Helium clusters in a 3200 nm wavelength (MIR) in Szeged, where we make measurements of cluster size dependence, Xe-Ca, Ar and water doping dependence and pulse duration dependence. Finally we present the results at the second beam time in ELI, where similar experiments were performed with the same laser using Ne clusters. Measurements of cluster size dependence, pulse duration dependence and Xe doping were also performed. More detailed information about the laser system used can be found in [69].

To assure a clear presentation of the results, each section is divided in 3 parts, Laser parameters, droplet size and doping dependence. On each section we will present the main results as the histograms and mean values for the individual experiments. In chapter 5 we will discuss the analysis of the data and the comparison between signals at similar parameters in order to overview the different principles behind the plasma formation. We will refer electron-VMI just as VMI in the following chapters.

4.1 Helium Nanoplasma in NIR Fields

As presented in section 3, the setup allows to modify several parameters such as: The cluster can be created, at different nozzle temperatures resulting in different

droplet sizes. He can be doped with one or two elements and different dopant sizes. Finally the cluster will be driven into a coulomb explosion by a fs laser pulse, so the electrons will be detected by the VMI spectrometer and the ions will be detected by the TOF detector.

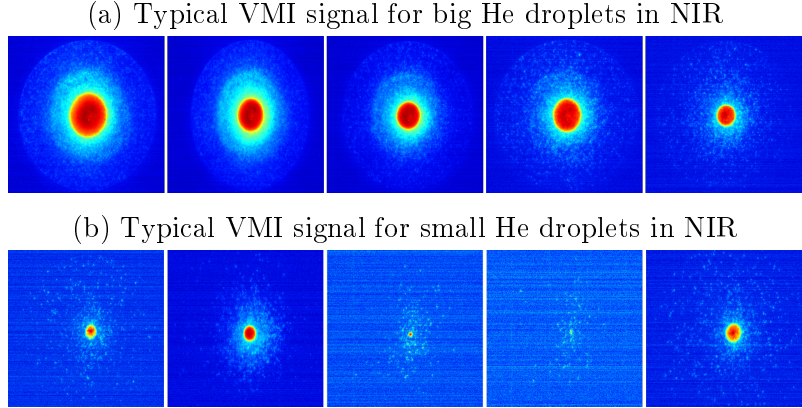


Figure 4.1: Some examples of VMI images for He clusters in NIR laser field. fig a. presents typical intense signals for big droplets and b. shows typical pictures of the weaker signals.

In the next sections, special attention will be taken on the VMI results due to the amount of information it can deliver. The TOF data, is analyzed in an independent way, but will not be part of the main results. The data on He droplet in NIR laser fields were already analyzed in the master thesis of Nicolas Rendler and the information can be found in [59]. The main purpose to re-evaluate this information is to compare the experiments with similar parameters to the ones used in ELI-AlPS.

Fig. 4.1 show some example of the variety of radius and intensities for the electron-VMI signal for He cluster in NIR laser field, it presents high and low intense signal for different data sets. In Fig a. the high brightness allows to see the edge of the detector in the outer circle close to the frame of the pictures. All signals present a similar behaviour, a uniform circular feature with a defined edge surrounded by a cloudy background. The most frequent signals are the small and less intense pictures like the bottom row.

Fig. 4.2 left, shows an example of hundreds of individual He signals summed and averaged, on the right it inverse abel transform PES done in MEVELER [?] for different droplet size (nozzle temperatures). On the left, an example for the biggest droplet, the white circles shows the energies marked with dash lines on the right plot. The Energy distribution presents a first peak that shifts from 0.5 to 3 eV depending on the droplet size and decrease down to 50 eV rapidly, which is the limit of the detector. It means that, the summed signal has a sharp derivation on

the intensities, showing that the average signal presents a defined maximal energy (radius) similar to the single explosion signals. For the next subsection the data presented will be evaluate from the single shot explosion.

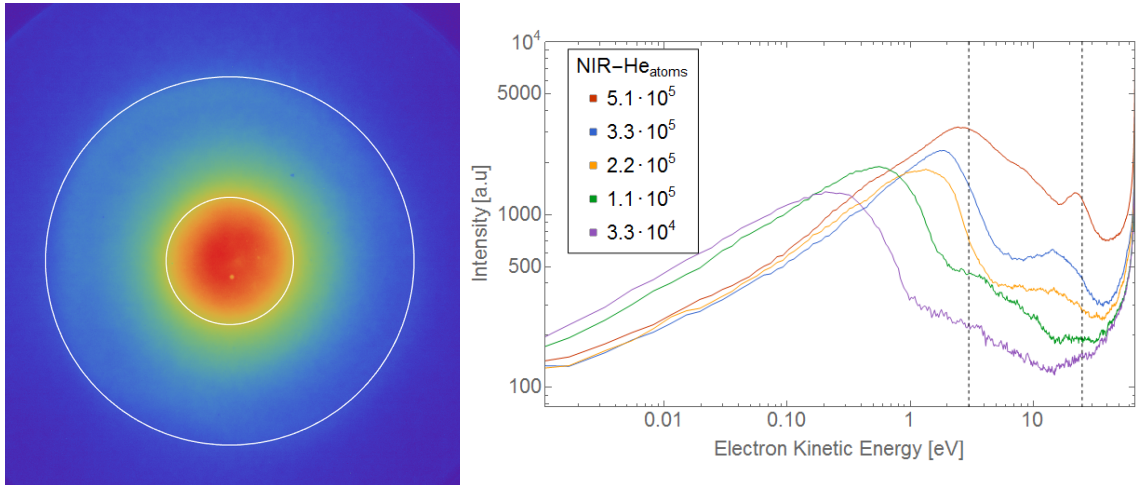


Figure 4.2: Average energy distribution for VMI signal in He clusters driven by NIR laser fields. On the right and example of the raw images for the biggest clusters. The plot, shows the inverse abel transformed PES for the summed and averaged signal at different clusters sizes. The dashed lines mark the energies at 3 and 25 eV where the two peaks are present and correspond to the edges of the circular feature in the raw image.

4.1.1 Laser Parameter Dependence

For the interpretation of the measurements it is important to determine the laser intensity in the focus of the ionization volume. The laser system used at the Max-Plank-Instituted is a NIR laser at 800nm wavelength and a rate of 3.5 Hz and a $d_{pulse} = 23\text{ fs}$ pulse duration measured by Nicolas Rendler in his master thesis [59]. Table 4.1 shows the different laser intensities used in the experiments calculated with Eq 5.3 in Render's work [59] $I(P) = P \cdot 5.7 \cdot 10^{12} \text{ W/cm}^2$ where I is the laser intensity in the focus and P is the power of the laser measured before it enters into the chamber

He Droplet Intensity Dependence.

Helium clusters at the same nozzle temperature $T_{nozzle} = 12.2\text{ K}$ and backing pressure of $P_0 = 45\text{ mbar}$ were doped with Xenon at a fix doping level, with the a constant pressure measured in the oven chamber of $P_{oven} = 2 \cdot 10^{-6}\text{ mbar}$. This measurement were taken with a slightly smaller detector arrangement with a diameter of $d = 42.2\text{ mm}$ of active area. At this nozzle temperature the helium droplet

Power [mW]	Laser intensity [W/cm ²]
55	$3,1 \cdot 10^{14}$
80	$4,5 \cdot 10^{14}$
115	$6,5 \cdot 10^{14}$
140	$7,9 \cdot 10^{14}$
185	$1,0 \cdot 10^{15}$
210	$1,2 \cdot 10^{15}$
240	$1,3 \cdot 10^{15}$

Table 4.1: Laser focused intensities calculated for different Powers

have proximate $N = 3.9 \cdot 10^6 \pm 1.4 \cdot 10^6$ atoms before going through the oven chamber and its doped with $X_{e,dop} = 134$ atoms. The VMI voltages were set to VMIx1 (see table 2.1) and the MCP and PHS to 1250 V and 4000 V respectively. The camera was establish to exposure time of $\tau_{exp} = 1$ ms. 50000 pictures were taken for 7 different laser power, at 55, 80, 115, 140, 185, 210 and 240 mW.

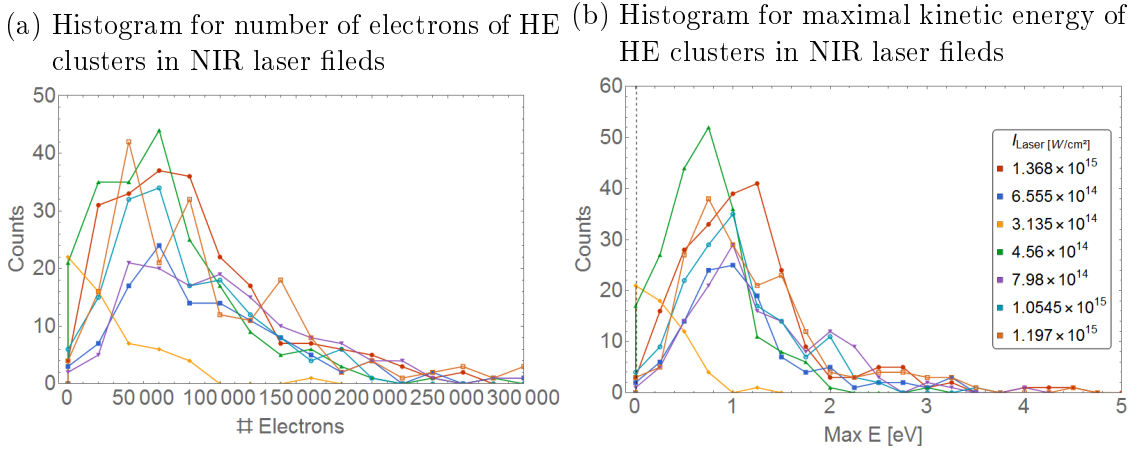


Figure 4.3: On the left, The histogram for the number of electrons. On the right, the histogram for the maximal kinetic energy found in He clusters in NIR laser fields. The dashed line on the right, shows the energy correspondent to 6 pixels that is the minimum radius reachable by the signal finder protocol.

After the signal is detected, the signal finder protocol determine the radius and brightness of the central feature in each picture, transforming it to number of electrons and maximal kinetic energy. Fig 4.3 presents the histogram for the number of electrons (Left) and the max energy (right) for the different laser intensities. As shown, the histogram presents a clear maxima around 60000 electrons and 1 eV respectively. Both present Boltzmann distribution shapes ramping up the values in the lower energies and electrons values and a slower slope for the higher ones. The dash line on the energy plot represents the minimum energy that the algorithm can

detect.

Fig. 4.4 top, present the signal rate defined as the number of picture with signal over to the total number of pictures taken. It shows a strong dependence on the laser intensity, but even at lower intensities some coulomb explosion can be found. Although the percentage of pictures with signal decrease remarkably, was never found zero signal, meaning that there was enough initial ionization to start the coulomb explosion. Fig 4.4 bottom shows the mean number of electrons and the mean maximal kinetic energy, it reach a maximum after $I = 8.5 \cdot 10^{14} \text{ W/cm}^2$ and both graphs stay constant at higher intensities. This result is not surprising because we don't expect large differences on the energies reached after the system is fully ignited, suggesting that after the beginning of the process, the coulomb explosion keeps a constant behaviour. First, the laser intensity play a fundamental role in given the starting condition to the nanoplasma formation but after a threshold, the laser does not influence in the final coulomb explosion any more. Second, a clear density limit is shown, it is possible that it is influence by this limitation of the laser on the process, but mostly it can be limited by the droplet size that was used in the experiment, as consequence, the biggest droplets are all expanding so in order to find bigger energy and densities we should use lower nozzle temperatures.

4.1.2 He Droplet Size Dependence.

For this data set, helium clusters at different nozzle temperatures, were doped with xenon, with a doping pressure $2 \cdot 10^{-6} \text{ mbar}$ measured in the doping chamber. The VMI were set to VMIx1 voltages and the MCP and PHS to 1250 V and 3400 V respectively. The camera was set to $\tau_{exp} = 1 \text{ ms}$ exposure time. 50000 pictures were taken for 5 different temperatures, at 12.5 K, 13 K, 14 K, 16 K and 20 K. The data were analyzed using the data processing mentioned in chapter 3 to convert the bloop radius and its inner brightness to maximal kinetic energy E_{max} and number of electrons ($\#e-$). Extrapolating the data of Render's thesis [59], we can calculate a prediction of the total number of atoms before and after the doping. Table 4.2 shows the mean number of atom per cluster to at the different nozzle temperatures and also its corresponding number of dopant.

Similar as the last subsection, radius and brightness of each signals were transform to max kinetic energy and number of electrons using the signal finder routine. Fig 4.5 shows the histogram for the number of electrons (left) and the max energy (right) for the different number of atoms $< N >$ in the cluster. The histogram presents contrasting distributions with stiff and clear peaks for the smaller droplets and broader distributions for the bigger droplets. In the num of electrons histogram, the

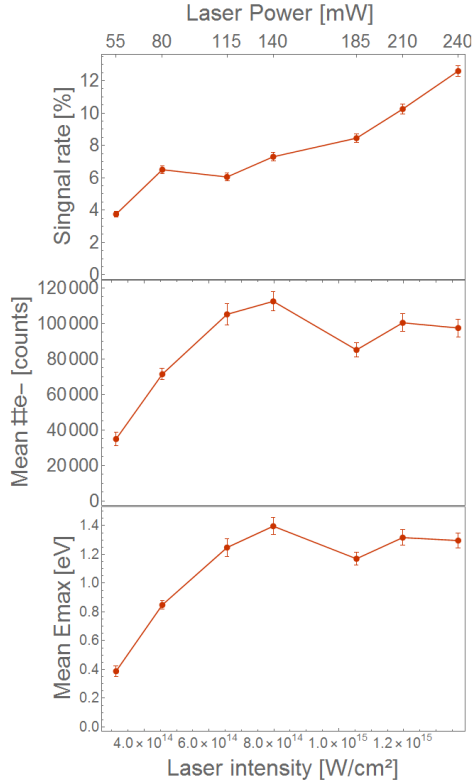


Figure 4.4: On top, the signal rate at different laser intensities. On bottom, the mean number of electron and the mean Max energy for the different laser power. The error bar correspond to the standard derivation for each data set.

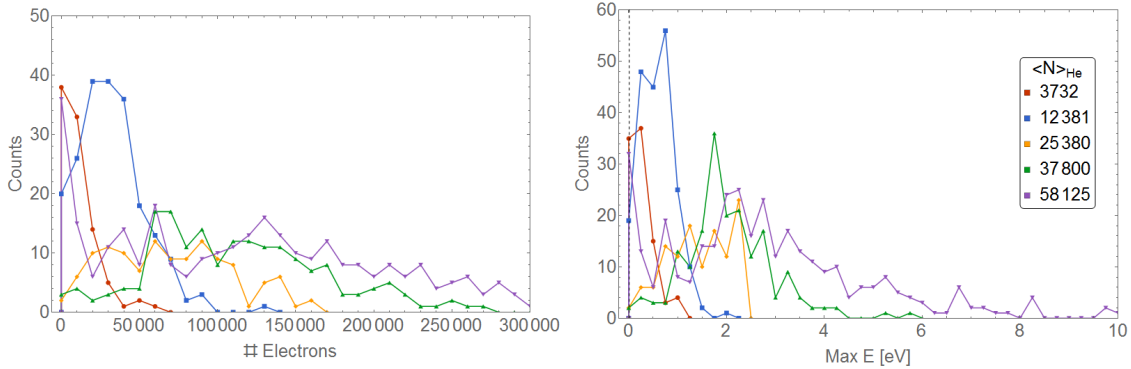


Figure 4.5: On the left, The histogram for max energy and on right, the histogram for number of electrons.

smallest droplets have a peak lower than 50000 while the lower nozzle temperatures have a plateau structure over 80000, same for the energies with peak in 1 eV and 2.5 eV respectively.

Fig. 4.6 shows the corresponding signal rate depending on the cluster size. As shown, the biggest droplets contain the highest percent of signal compared to the small droplets. It is expected due the bigger droplets can pick up more dopants and

NIR Helium Cluster Size (Ref)		
$T_{Nozzle}[K]$	$N_{Xe}\text{atoms}$	$N_{He}[\text{atoms}]$
20	66	$3 \cdot 10^4 \pm 1.5 \cdot 10^4$
16	199	$9 \cdot 10^4 \pm 4.5 \cdot 10^4$
14	189	$2.0 \cdot 10^{5 \pm 1 \cdot 10^5}$
13	149	$3.1 \cdot 10^5 \pm 1.5 \cdot 10^5$
12	160	$5 \cdot 10^5 \pm 2.5 \cdot 10^5$

Table 4.2: NIR Helium Cluster Size

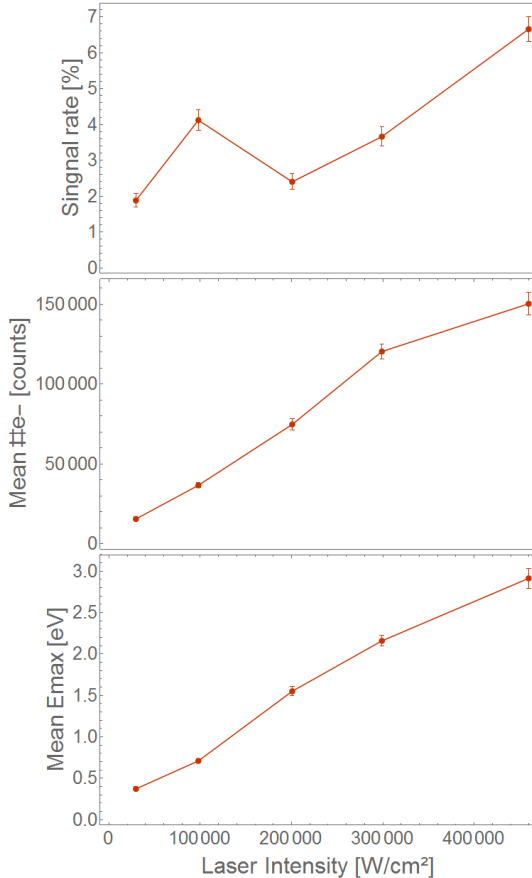


Figure 4.6: On the top, the signal rate at different laser intensities. On bottom, the mean number of electron and the mean Max energy for the different laser power. The error bar correspond to the standard derivation for each data set.

increase the initial ionization probability. Furthermore, the larger the number of atom in the cluster the most electrons available to be detected. In the Mean $\#e^-$ and E_{max} values, for example at 12 K, the mean energy shows that exist counts for high energetic explosion, up to 4 eV, but the mean value of all the data is not higher than 3 eV. This behaviour is also present for the other nozzle temperatures, where there exist a broad distribution for 13, 14 and 12 K with mean values further from

the biggest value. Moreover, the number of electron in the system also rise with the size, for $\text{Ne}_{5.10^5}$ the mean number is close to 150000 electrons, almost 10 time bigger than the smallest droplets. Similar happens in the signal rate, the mean values present a linear dependence with the droplet size. This trivial relation is due the increment on the number of electron available in the system, so the bigger the droplet the bigger the explosion.

4.2 Helium Nanoplasma in MIR Fields

In this section helium nano droplets doped with different alkaloids in mid-infrared laser fields are described. Helium was expanded from a nozzle of $5 \mu\text{m}$ opening at a backing pressure of $P_0 = 30$ bar, using different nozzle temperatures. The beam is doped with a xenon gas when passing through a gas doping cell in the doping chamber or calcium atom when it pass through the oven. Therefore, the mean dopant cluster size is determined by the xenon pressure in of the gas doping cell, which is controlled by a high-precision needle valve and the oven temperature. The flight distance through the gas doping cell is 30mm. The MIR laser pulses are orthogonal to the cluster beam through a vacuum window into the chamber and focused into the cluster beam by a focusing mirror. The laser intensity in the focus during the measurements was in average $2.5E14 \text{ W/cm}^2$ at a maximum power of $P \sim 10 \text{ W}$, it had a minimum pulse duration of $t_{pulse} = 45 \text{ fs}$ and a rate of 10 KHz. The laser power depends on the pulse duration because the total pulse energy needs to be distributed on time, in each specific case we will denote the power when it changes. The polarization of the laser field was orthogonal to the spectrometer axis. The laser systems was operated in all time by the ELI-laser personal supporting the experiment. The electronic signals were recorded with the Basler CCD camera at a minimal exposure time $t_{Exptime} = 45\mu\text{s}$ triggered with the TOF as explained in chapter 3, this process grants the single shot signal. The camera is focused on the MCP-PHS arrange that makes the electron signal visible.

We do not expect that all laser shots hit a cluster or generates a plasma explosion, so most of the data sets had low signal rate (#Pic with signal/total # Pics), in order to have representative statistics, in each experiment were taken 10000 pictures, about less than 10% had signal. Fig4.7 shows example of different range of explosions and signals. Most of the VMI signal had the expected circular aspect except for the larger size droplets, with the donut shape. Because we are using a bigger MCP, we cut the images closer to the center to avoid analyze irrelevant data.

Fig. 4.8 left, shows an example of hundreds of individual He signals summed

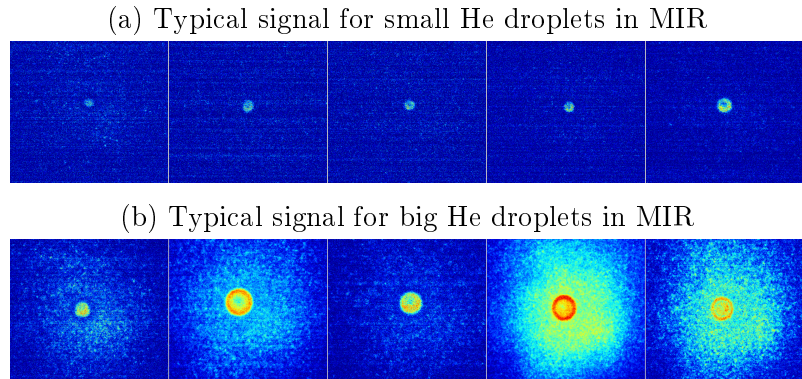


Figure 4.7: On the top, the typical pictures for small He droplets explosion of low intense signal. On the bottom, the typical pictures for the big He droplets that usually contains the more intense signals. Also, the donut shape is present in either some of the small signals as in the bigger ones

and normalized at 10.5 K, on the right it inverse Abel transform PES for different droplet size. As before, the energy distribution shows a clear trend independent of the nozzle temperature. It presents a first shoulder around 0.1 eV and decaying constantly down to 12 eV. The dashed lines indicate the energy of the white circle in the picture, it set the edge of the central feature correspond to the falling edges of the energy spectra, similar to the signal for single explosions.

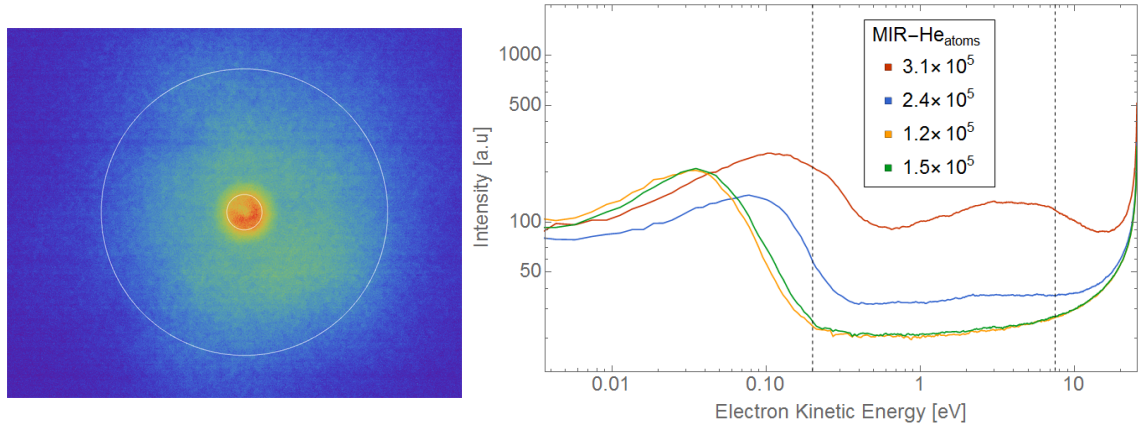


Figure 4.8: On the left, The histogram for max energy and on right, the histogram for number of electrons.

The MIR and NIR signals present large similarities except for the high intense pictures with a localized energy on the edge, or a donut shape, with low brightness in the center and a high intensity in the edge of the central feature. Despite this differences and because we are focus on the single explosion, it does not affect the signal analysis due we are based on the max kinetic energy and not in the internal energy distribution.

4.2.1 Helium Droplet Size Dependence.

He clusters at different nozzle temperatures, were doped with Xenon at a pressure of 0.0060 mbar measured in the gas doping cell. The voltages were set to VMIx1 and the MCP and PHS to 1600 V and 4000 V respectively. The camera was set to minimum exposure time and the trigger system was used. 10000 pictures were taken for 4 different temperatures, at 10.6 K, 11 K, 12 K and 12.5 K. The data was evaluated once more as last section, as result, it was shown that even for this high repetition laser rate, single shot signals was achieved. The TOF signal work as a reference to identify the single explosion, and then each individual VMI picture is treated as follows. Fig 4.9 shows a mean TOF for the measurement at $\text{Ne}_{2.8 \cdot 10^5}$. As we can see, there is a large amount of water and a small peak for hydrogen still in the vacuum chamber, this remain gases affect especially for the background. It is shown that Helium is effectively ionized due the peak at He^+ but no He^{2+} signal was identify, on contrast to Fig. XXX were single explosions with ${}^2\text{He}^+$ peaks were identified.

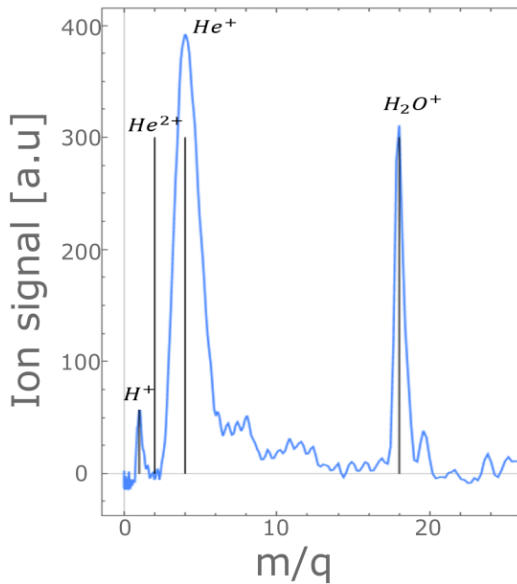


Figure 4.9: Mean TOF spectra for He at 10.6 K.

Using the experimental data taken on the NIR experiments by Nicolas Rendler [59], we can extrapolate the data to have a prediction of the total number of atoms before and after the doping. Table 4.3 shows the mean number of atom per cluster to at different nozzle temperatures and its corresponding number of dopants. As reference for the cluster size scaling, we used data at $P_0 = 50$ bar and temperatures similar to the experiment.

Fig 4.10 shows the histogram of the E_{max} and $\#\text{e}^-$ for the different temperature.

Cluster Size reference		
T_{Nozzle} [K]	N_{Xe} [atoms]	$\langle N \rangle_{He}$ atoms
10.6	220	$2.80 \cdot 10^5 \pm 1.4 \cdot 5$
11	192	$2.29 \cdot 10^5 \pm 1.1 \cdot 5$
12	138	$1.42 \cdot 10^{5 \pm 1.2 \cdot 5}$
12.5	119	$1.13 \cdot 10^5 \pm 1 \cdot 5$

Table 4.3: cluster size reference

On one hand, in the E_{max} , the first peaks describe that most of the droplets achieve energies between 0.05 and 0.1 eV, decreasing rapidly after. On contrary, the biggest droplets have a more broaden distribution than the higher temperatures. Furthermore in the $\#e-$ histogram, a broader distribution is shown, a larger assortment is found for droplets with less than 2000 electrons, having a drastic decrease after with some individual points at a huge number up to 80000 $e-$.

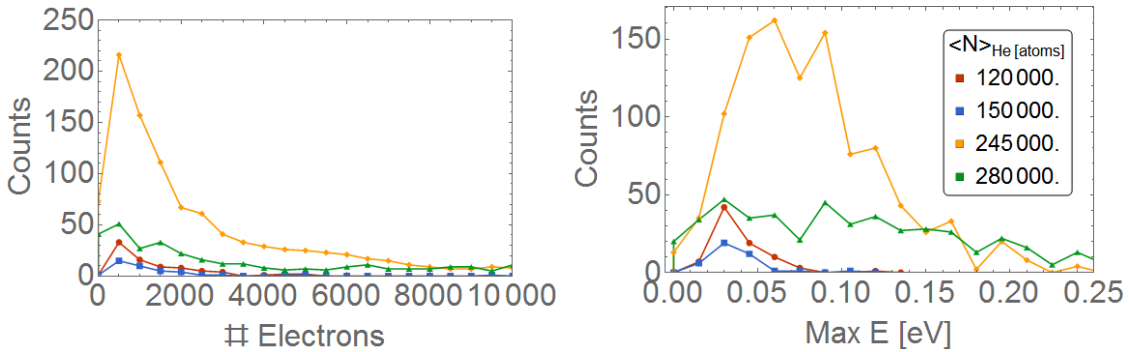


Figure 4.10: On the left, the histogram for max kinetic energy. On right, the histogram for number of electrons.

Fig 4.11 presents the signal rate and the mean values for the number of electrons and max kinetic energy depending on the droplet size. As shown the figure, the biggest droplet have the largest signal rate at 10.6 K and 11 K and immediately for the smaller droplet the rate decrease drastically, same tendency is show in the mean values, suggesting that that the plasma is easier to ignite at lower temperatures. Therefore, as more electrons and energy are detected while the signal rate increase, we assume that the nanoplasma formation is more efficient for larger droplets. The drop on the signal rate at 10.6 K compared to the 11 K can evidence a loss of efficiency for the laser to ionized huge droplets. Unfortunately, no other measurement where taken at lower temperature to confirm if this is a statistical event or a real effect.

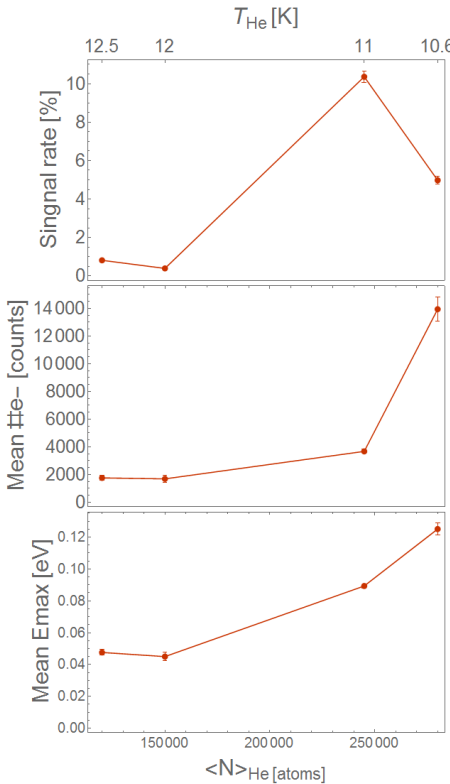


Figure 4.11: On top, the signal rate in percentage of the pictures with signal depending on the nozzle temperature. On bottom, the mean of the number of electrons and the Max energy for each point respectively.

4.2.2 Doping Dependence

One of the advantages of the setup is the possibility to exchange easily the doping element. Here we present the results of four different dopants at different level in He droplets. Xe and Ar were introduced through the needle valve to the doping cell while the calcium was evaporated from the oven. Fig 4.12 present typical examples of the signal at each doping element. Although the signal varies in intensity, specially for the Ar doping, the shape and structure looks similar to the above experiments, so same procedure will be applied.

Helium-Argon Doping.

In this data set, He clusters were doped with Argon at different gas doping pressures. Helium was produced at a nozzle temperature $T_{nozzle} = 11$ K and ignited by the MIR laser pulse, the VMI were set to VMIX1 voltages and the MCP and PHS to 1700 V and 4000 V respectively. The camera was set to $t_{exp}=50$ μ s exposure time what means the data was not correlated with the same trigger. The exposure time was modified due to the low signal rate, nevertheless the information will be still evaluated.

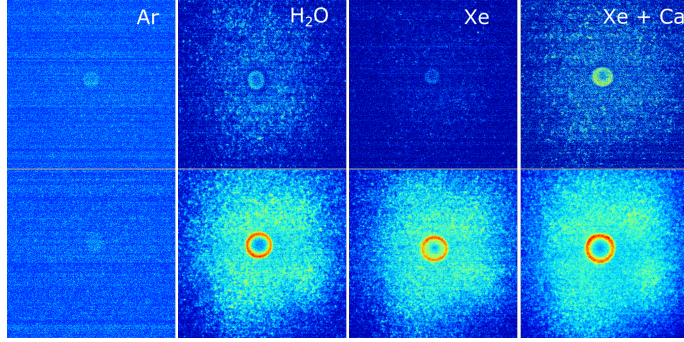


Figure 4.12: typical signals for He cluster doped with Ar, water, Xe and a Xe-Ca mixture. The signal varies in intensity, on top the usual low brightness and on bottom the more intense pictures

in the same way as before, taking into account that signal rate was so low that is possible to have single shot. 100000 pictures were taken for 3 different doping pressures, at $2 \cdot 10^{-4}$, $6 \cdot 10^{-4}$ and $12 \cdot 10^{-4}$ mbar measured in the gas doping cell.

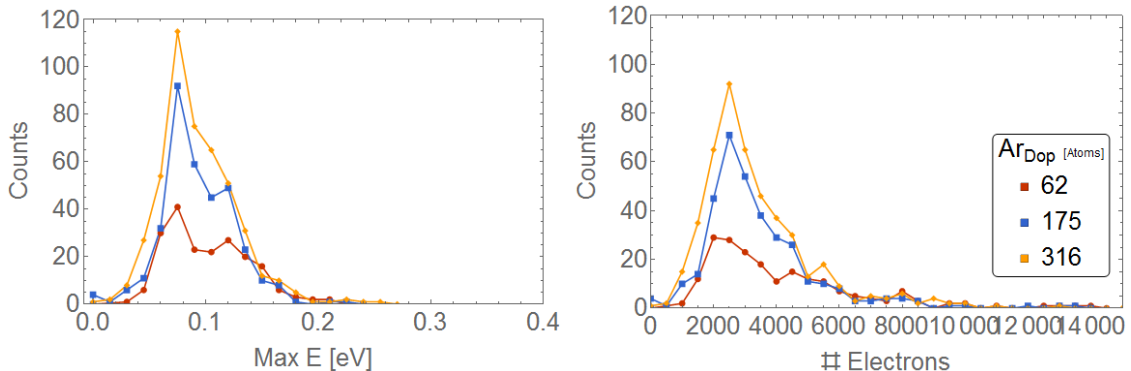


Figure 4.13: On the left, The histogram for max energy and on right, the histogram for number of electrons for He clusters in MIR laser at different doping level.

Fig 4.13 shows the histogram for the He droplets doped with Ar at different doping levels, On the left the max energy distribution shows peaks around 0.1 eV with a similar distribution independent the doping level, Same in the mean number of electrons (left), where the peak is around 3000 e- and the disposal of the plot shows similar tendency

As shown in the previous examples, the signal intensity for argon was low and it is reflected in Fig 4.14 where the signal rate (top) is lower than 5 %. Here the amount of dopant increase the efficiency of the plasma, going from a 2 % up to 4.5 %. Combined to the Mean values results, where the mean values decrease with the doping, we can deduce that the efficiency for small droplets ignition also improves. As seen before, the histograms have a slightly broader distribution with high doping

level, evidencing that the dopant helps in the plasma formation of the smallest droplets.

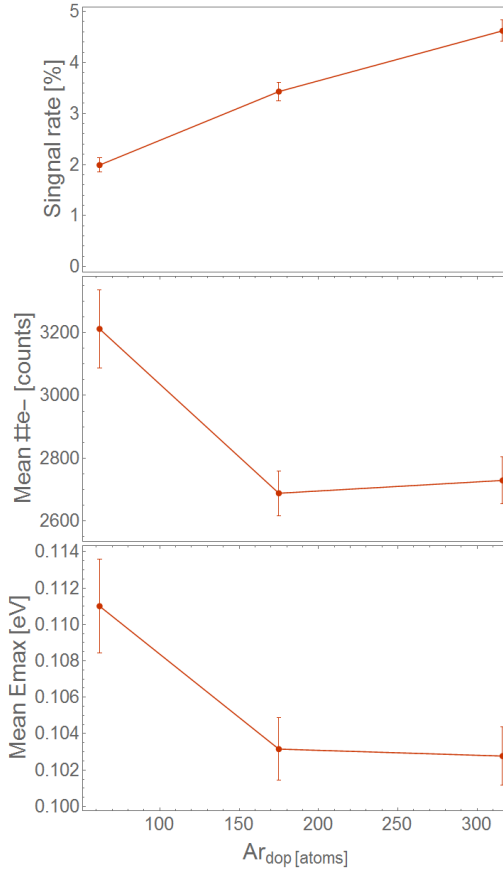


Figure 4.14: On the top, the signal rate for the He-Ar doping. Center and bottom, are the mean values for the number of electrons and max energy respectively

Helium-Water Doping.

One of the most common and available dopants is water, not just because it is easy to get in the lab but also because it is also difficult to remove from the vacuum chamber. Even in our best vacuum, experiments usually contained few traces of water. In addition, at Mid-Infrared, water have a special resonance that could be advantageous because it will withstand a faster ionization and in consequence, a better creation of the plasma. This data set was taken with He droplets at $T_{\text{nozzle}} = 11 \text{ K}$ doped with water. A small drop of water were located into the entrance of the needle valve, to achieve a controlled doping. The pressure at the gas doping cell was varied in order to perform several doping levels. The camera was set to $t_{\text{exp}} = 120 \text{ ms}$ so single shot was not enabled. The voltages were set to VMIx1 and the MCP and

PHS to 1750 V and 4000 V respectively. 100000 pictures were taken for 5 different doping pressures, at $1 \cdot 10^{-4}$, $2 \cdot 10^{-4}$, $3 \cdot 10^{-4}$, $6 \cdot 10^{-4}$ and $12.5 \cdot 10^{-4}$ mbar.

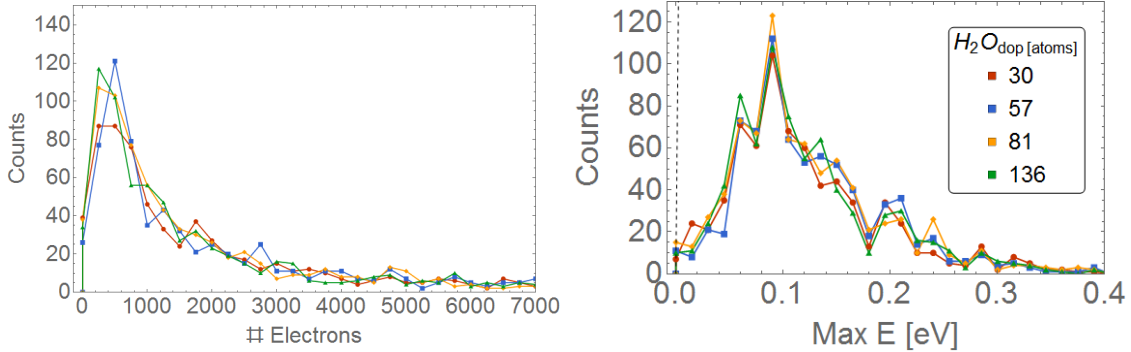


Figure 4.15: On the left, The histogram for max energy and on right, the histogram for number of electrons for He clusters with water in MIR laser at different doping levels.

Similar to the histograms above, fig 4.15 presents small changes on the max energy distribution and number of electrons, where there is a well defined peak around 1000 e- and 0.1 eV. In this case the energy distribution does not present any broadening and the counts behaves independent on the doping level. The dash line in the left, represent the minimum energy (radius) that the blob finder can achieve.

Fig 4.16 presents the signal rates and the Mean number of electrons and max energy depending on the water level. As shown, the three rates have similar and constant values, for the signal rate, the values oscillate around 7 % independent the doping level, On contrast to Argon. Same happens to the mean values that are around 3000 e- and 0.13 eV respectively. As we showed, under the correct doping levels and He cluster sized, water molecules are a great dopant to ignite the He cluster in MIR laser pulses. The nanoplasma reach high energy states as well as a huge radius for the electronic cloud, reaching mean of electrons detected up to 70000. The mean values in the energy or electrons does not depend on the doping, as already described in the other experiments, once the ionization process ignites the plasma the final result does not present variations.

Helium-Xenon-Calcium Doping

In this experiment Helium clusters where doped with Xenon and Calcium atoms simultaneously. The Helium clusters were created at the same nozzle temperature $T_{nozzle} = 10.6$ K and a backing pressure of $P_0 = 30$ mbar. Xenon were introduce at 5 different pressures measured in the gas doping cell and Calcium was evaporated in the oven at 7 different temperatures. Table ?? shows the sorted parameters used

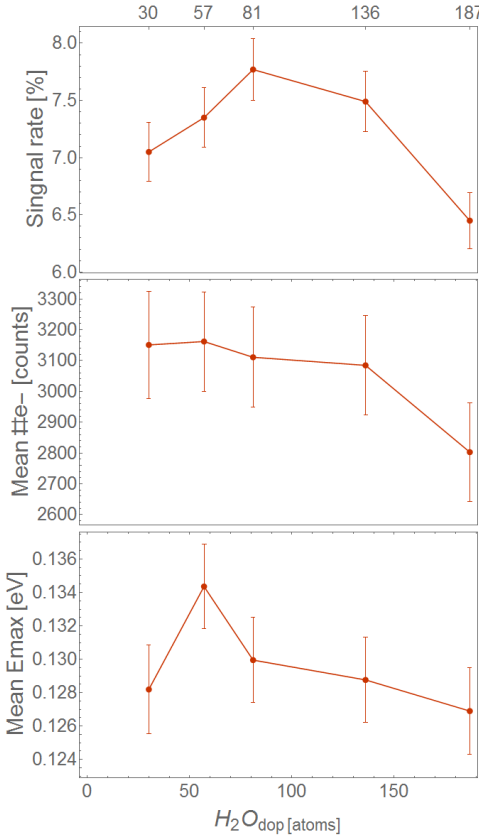


Figure 4.16: On the top, the signal rate for the He-Water doping at different doping levels. On the center and bottom, are the mean values for the number of electrons and max energy respectively

and their associate cluster size. The cells in the index (up and left) represent the number of atom for the Xenon and calcium for each data set while the inner cell shows their correlates mean He cluster size in atoms, The spaces in black are data set that were not taken. The VMI voltages were set to VMIx1 and the MCP and PHS to 1600V and 4000V respectively. The camera was stablish to exposure time of $t_{exp} = 34\mu s$ and single shot was assure. The laser power was monitored constantly to guarantee an average power of 10.7 W at pulses duration around 45 fs.

In Fig we present the histograms for $\#e^-$ and E_{max} . All the different doping are plotted in the same diagram in order to show that it doping the tendency does not change radically. As usual, the points are the individual pictures blob analysed and binned, the dash on the energy histogram represents the minimum energy that the finder can achieve at 6 pixels. Further, the histograms we can show that the E_{max} distribution is similar for all doping. There is a defined peak close to 0.1 eV with a Boltzmann distribution likewise and a slow slop up to 0.4 eV. Moreover, the number of electrons present a peak close to 2000 with the slop decreasing down to 8000 where the counts reduce below 10. A second result to take into account, mentioned

Xe_{dop}	0 atoms	30	90	180	350
Ca_{dop}					
5 atoms	$2.4 \cdot 10^5$	$2.3 \cdot 10^5$	$2.3 \cdot 10^5$		
7	$2.3 \cdot 10^5$	$2.3 \cdot 10^5$	$2.3 \cdot 10^5$		
15	$2.2 \cdot 10^5$	$2.2 \cdot 10^5$	$2.1 \cdot 10^5$		
22	$2.1 \cdot 10^5$	$2.1 \cdot 10^5$	$2.0 \cdot 10^5$		
31	$1.9 \cdot 10^5$		$1.8 \cdot 10^5$	$1.8 \cdot 10^5$	$1.7 \cdot 10^5$
45	$1.7 \cdot 10^5$		$1.6 \cdot 10^5$	$1.5 \cdot 10^5$	
62	$1.3 \cdot 10^5$		$1.3 \cdot 10^5$	$1.2 \cdot 10^5$	$\langle N \rangle_{He_{atoms}}$

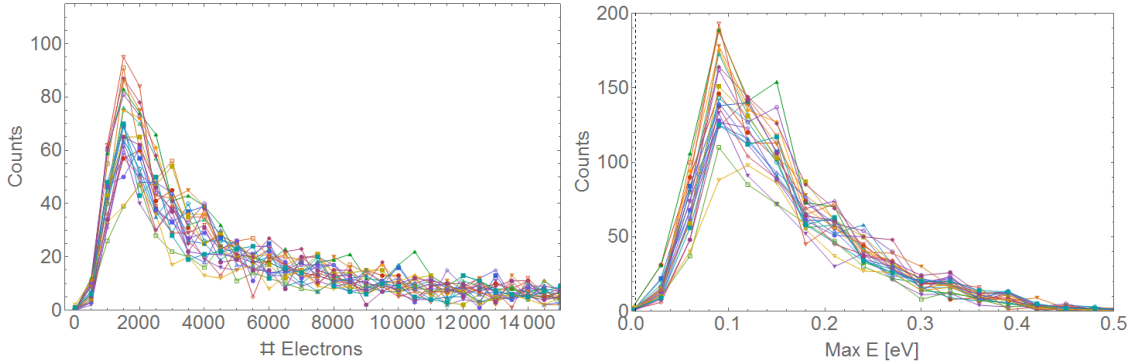


Figure 4.17: On The left, the histogram for the Number of electrons for all doping levels. On the right, the histogram for the Max energies. The electron histogram was binned every 1000 e- while the energy was binned every 0.03 eV. The behaviours of the histograms follows the Boltzmann distribution and remains independently from the doping level, the counts remains relatively constant.

in the past section, is that the histogram share a peak electrons but the counts are reduce because of the signal rate as expected, so the dopant level does not play a big role in the final distribution of the nanoplasma energy, but as we will see next, it does act in the signal rate and mean values.

Fig 4.18 shows an interpolation for the signal rate and mean values for the max energy and number of electrons. The green scale shows the signal intensity in percentage, #e- counts and energy in eV for each doping level respectively, on the bottom axis the number of Xenon atoms and on the left axis the number of calcium atoms. The white points represent the doping levels where the measurement were done. According to the signal rate, there exist two maxima, one at $Xe_{100}-Ca_{20}$ and at $Xe_{360}-Ca_{30}$. The fist one is the most important because it shows an increment in the efficiency of the plasma formation at low doping comparable with the second peak where the number of dopants is 4 times longer. The histograms for electrons and energy also show a maxima but at low doping . The interpolation for the number of electron(center) presents the maxima at $Xe_{50}-Ca_7$ and a small depletion at

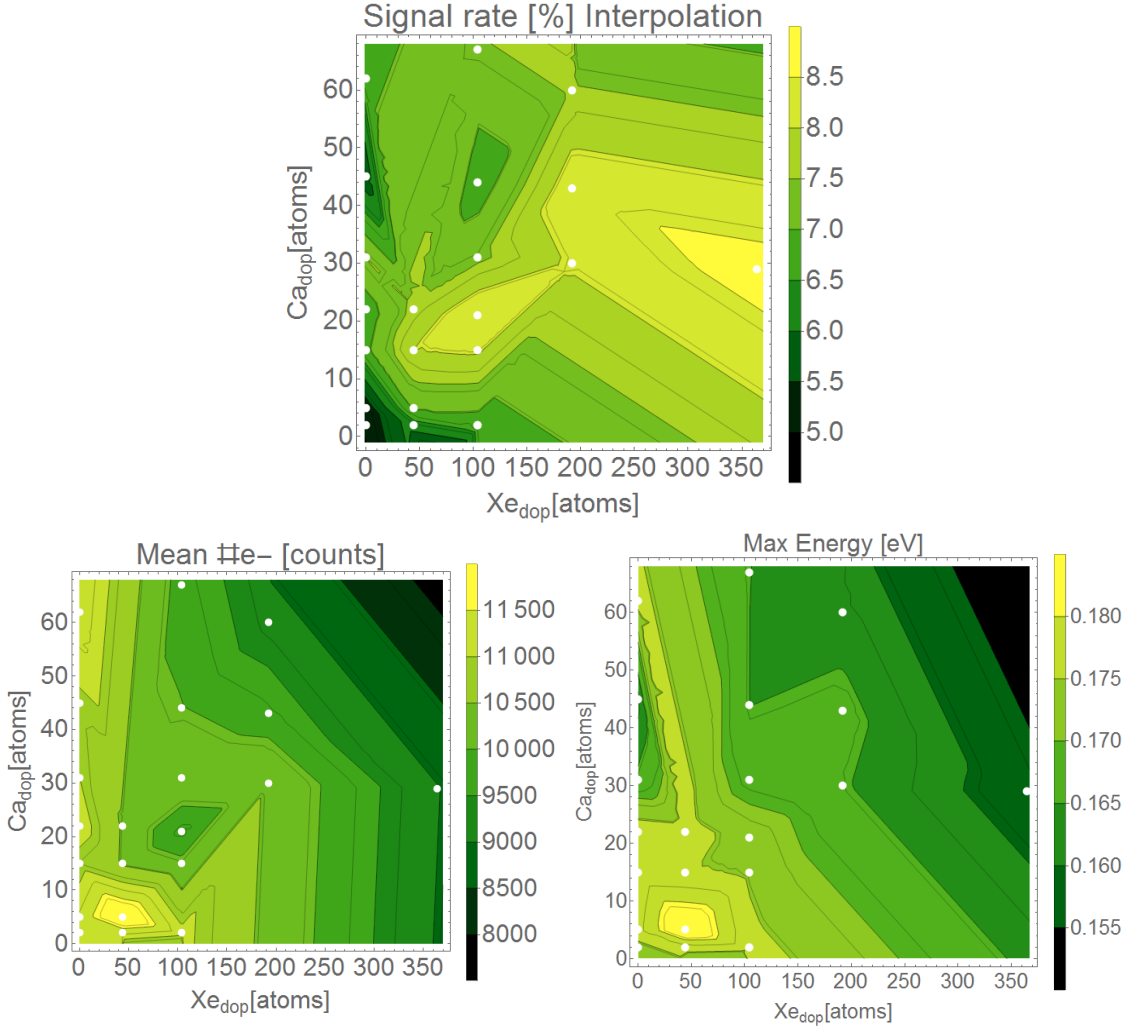


Figure 4.18: From left to right, the interpolation for the signal rate in percentage, mean number of electron in counts and mean max energy in eV respectively. The green scale shows the intensity of the signal where the light yellow means high counts and the darker green lower counts. The white points represents the doping levels where the measurements were taken.

$Xe_{100}-Ca_{20}$ with a constant decrease for higher doping level. In contrast, the energy interpolation have the same maxima as the num of electron but does not present the depletion. Moreover, after the highest energy is present a slow drop starts at heavier Xe doping. At larger number of dopant the interpolation is less precise due the lack of measurement, nevertheless we can see that for smaller droplets at heavy doping the cluster starts to deform and deplete it so the nanoplasma explosion is less powerful.

If we compare the three interpolation, we notice that the signal rate have a peak close to $Xe=100$ and $Ca=20$, but the Mean number of electrons and energy appears at lower doping. This means that at the most efficient rate, we are not igniting the

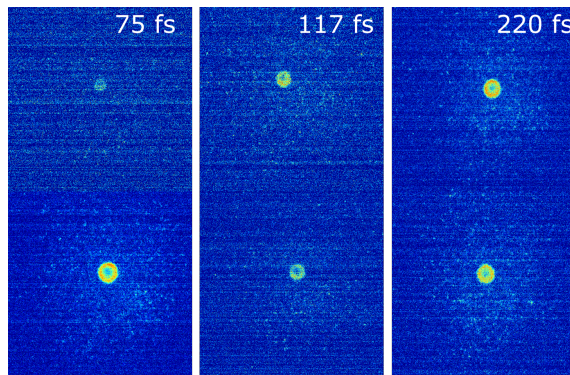
biggest droplets but on contrary, they are being exploded closer to the zero doping.

4.2.3 Laser parameter Dependence

Similar to the experiments done in Heidelberg with the NIR laser pulse. We perform the experiments through different intensities and pulse duration in order to see the effects of the laser system on the coulomb explosion. The laser system used at ELI-Alps is at 3200 nm wavelength and a rate of 100 KHz. One of the advantage of the laser system in ELI-Alps, is the possibility have a tunable pulse duration from $\tau_{pulse} = 45$ ps to 250 fs.

Fig 4.19 show some examples of raw VMI pictures at different pulse duration and in consequence intensities. All signal conserve the same structure seen until now, a circle in the center of the detector with a clear edge that can be identified by our blob detector algorithm. One difference to the images in NIR is the intensity of the signal. Here the pictures are faint and difficult to recognize sometimes specially for the lowest intensity as we will show next.

Figure 4.19: Raw images for different pulse durations and laser intensities. The most of the pictures show low intensity signal, the donut shape is also present for some of them.



Helium-Water Intensity Dependence

Helium clusters at the same nozzle temperature $T_{nozzle} = 11$ K and backing pressure of $P_0 = 30$ mbar, were doped with Water at a fix doping level $P_{dop} = 1E - 4$ mbar pressure measured in the gas doping cell. At this nozzle temperature the Helium droplet have proximate $N = 244647$ atoms before going trough the oven chamber and its doped with $H_2O_{dop}=56$ atoms. The VMI voltages were set to VMIx1 and the MCP and PHS to 1750 V and 4000 V respectively. The camera was stablish to exposure time of $t_{exp} = 34\mu s$. 100000 pictures were taken for 6 different laser power,

at 2, 4, 6, 7, 8 and 9.5 W, measured before the laser beam enters to the detection chamber and its back focus by the mirror.

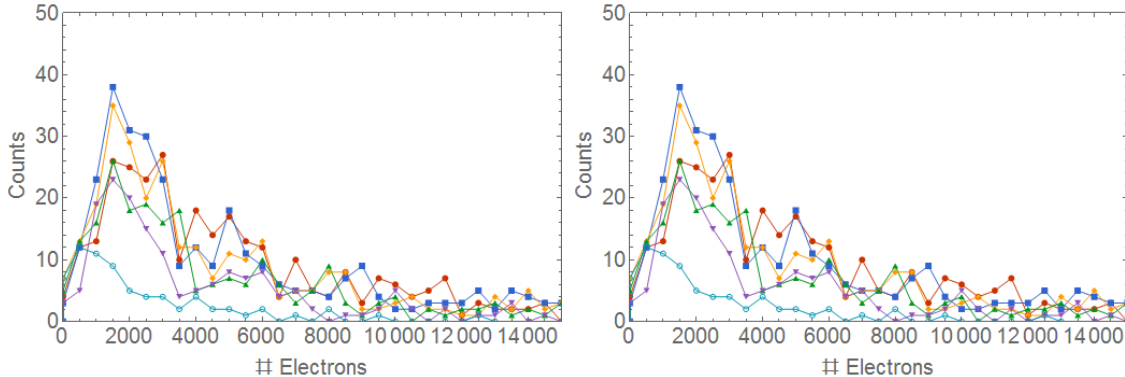


Figure 4.20: On The left, the histogram for the Number of electrons for all intensity levels. On the right, the histogram for the max energies. The electron histogram was binned every 1000 e- while the energy was binned every 0.015 eV. The dashed line in the energy histogram shows the minimum energy that the lob finder algorithm can achieve.

Having the laser power, the intensity can be calculated for each laser power using the Xe cut off calibration. The legends in Fig.4.20 are the different laser intensities calculated for each of the laser power using Eq 3.2. On the right, the energy histogram have a clear distribution, there exist a predominant range of energies where for all intensities most of the electrons reach a max energy around 0.1 Furthermore, on the left histogram, most of the data is distributes in the peak near to 2000 e-, having a stiff rise from zero to 1000 e- and a slower decrease after 4000 e-, the counts for bigger electronic clouds decrease for low intensities. As seen the blue and red line share a similar trend compared with high counts and a clear peak compared to the light blue and purple that have a broader distribution with lower counts.

Fig 4.21 top, shows the signal rate where a linear dependence is present for the laser intensity, meaning it plays a fundamental role in the ignition of the process. At lower intensity, less probable to find signal and the highest intensity shows up to 4 time more signals than the lower one. At the same time we can identify that once the intensity reach $2E14\text{W/cm}^2$ the process starts to keep in a constant rate, it suggest the existence of an intensity threshold, so the plasma formation will not be affected by the extra intensity radiated. This could be attribute to the ionization process, as known, minimum energy is needed ionized the dopant, but once these intensity is reach, all dopant will be completely ionized, so there is no longer energy transfer. On the bottom, the corresponding Mean of energy and number of electrons for each data set at it corresponding intensities. The mean values of #e- and E_{max} , shows a similar disposition as the signal rate, the more intense the laser pulse the

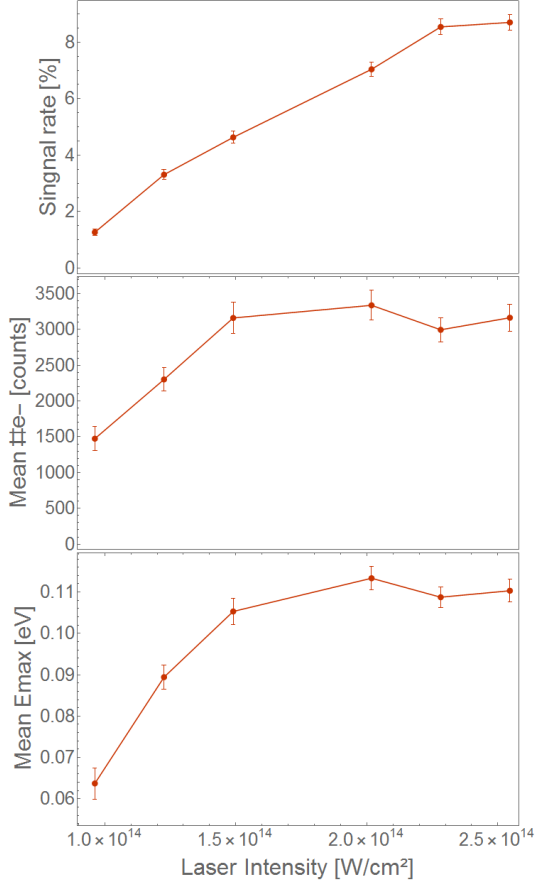


Figure 4.21: From top to bottom, signal rate and mean values of number of electrons and max energy for different laser intensities

more energy and electrons can be found. The means values start to rise in a fast way on left but once it reach the 3 best intensities the divergence decrease and changes are less noticeable, following our previous assumption with the signal rate.

Helium Pulse Duration Dependence

In this data set, we present the result for the energy distribution of helium cluster doped with Xenon in different pulse duration. Helium clusters at the same nozzle temperature $T_{nozzle} = 10.5$ K and backing pressure of $P_0 = 30$ mbar, were doped with Xenon at a fix doping level $P_{dop} = 2.4E - 4$ mbar pressure measured in the gas doping cell. At this nozzle temperature the Helium forms big clusters, with approximated $N = 3150000$ atoms before going through the oven chamber and its doped with $Xe_{dop}=75$ atoms. The VMI voltages were set to VMIx1 and the MCP and PHS to 1600V and 4000V respectively. The camera was stablish to a exposure time of $t_{exp} = 34\mu s$. A first averaged mode signal was taken as a guide to the eye and after 100000 pictures were taken at 4 different pulse duration, at 65, 120, 200 and

Pulse duration [fs]	Power[mW]	Laser intensity [W/Cm ²]
65	8.8	1.5E14
120	9.7	8E13
200	9.8	5E13
250	9.2	3.9E13

250 fs, measured by the ELI-laser personal supporting us in the experiment, using FROG technique. In the beginning of the experiment, we notice that the laser pulse have a dependence with the laser power, longer pulses results in a weaker power. Table ?? resume the laser power obtained for each of the pulse duration. Fortunately the intensities didn't defer much and the intensities obtained are farther that the threshold to start the coulomb explosion as seen in the intensity scan above.

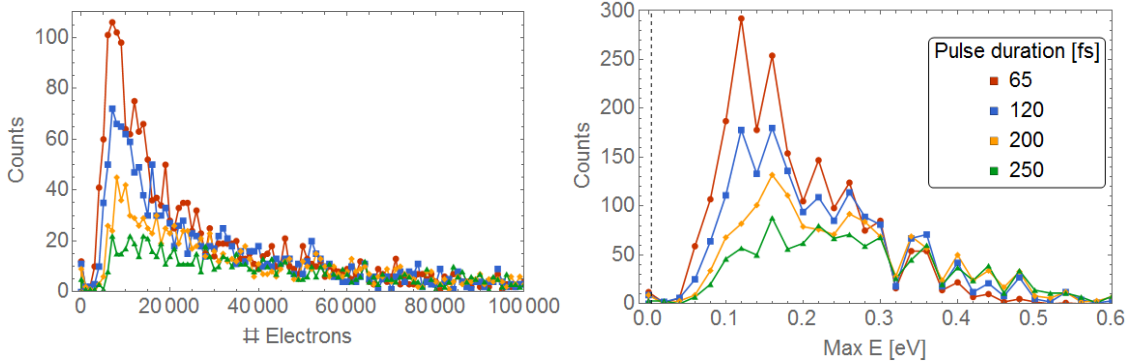


Figure 4.22: On The left, the histogram for the Number of electrons for all intensity levels binned every 1000 e-. On the right, the histogram for the max energies binned every 0.02 eV. The dashed line in the energy histogram shows the minimum energy that the blob finder algorithm can achieve.

Fig 4.22 presents the histogram a for the number of electron and e max energy. The histograms shows a clear peak for the shorter duration while in the longest the distribution get broader. It means, that the smaller droplets are easily ignited on the shorter pulses, so we see the peak close to 100000 electrons, Furthermore, the energy histogram also have a similar behaviour with a stiff peak that shifts around 0.15 to 0.2 eV depending on the pulse duration and with a slow decrease after 0.3 eV for all of them. The electron histogram on contrasts, does not present the peak shift but it does broaden its distribution with the pulse length.

Fig. 4.23 top, presents the signal rate for all the different pulses. As shown, the signal rate have a mark dependence on the pulse duration, at the short pulses it have a ratio of almost 20% and it starts decreasing constantly down to 10% at the longest pulse. This behaviour is expected because, as saw in the intensity dependence, once we stretch the pulse the energy gets redistributed, so the laser field interacting in the ionization process is weaker, hence, the coulomb explosion ignition probability

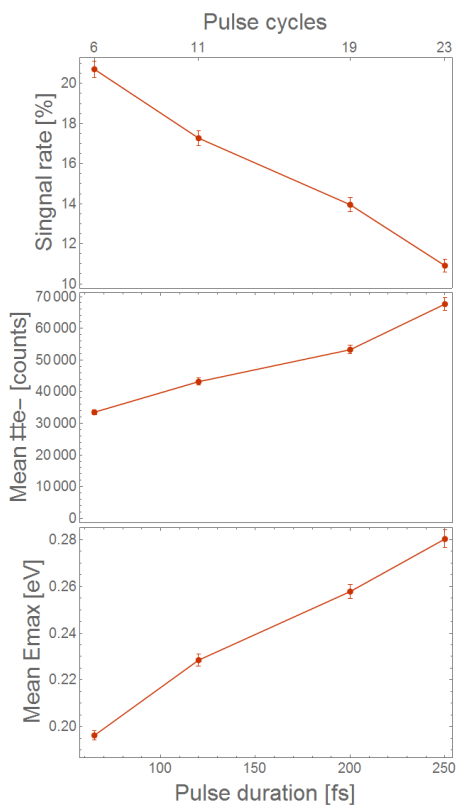


Figure 4.23: On the top, signal rate for the He-Xe pulse duration scan. On the center and bottom, mean values for the $\#e^-$ an max energy depending on the laser pulse.

decrease. On the center and bottom, we plot the mean number of electrons and E_{max} with dependency on the pulse duration. On contrast, the longer pulses are more likely to explode the bigger droplets. This can be seen in the energies mean where the values rises with the pulse, as in the number of electrons.

4.3 Neon Nanoplasma in Mid-Infrared

In the next section we present the results for the second beam time at ELI-Alps where we examines the nanoplasma formation of Neon clusters in Mid-Infrared laser pulses. The laser for this experiment was the same system used in Helium droplets. Neon cluster were created via a supersonic expansion with a conical nozzle with aperture $d=15 \mu\text{m}$ of diameter. In order to obtain different cluster sizes, we used several nozzle temperatures around 37 K to 42 K, with a constant backing pressure of 10 mbar. Neon 0.6 were used to assure the purity of the clusters and to avoid any nozzle clog. Neon was doped with xenon through the gas doping cell. We will present 3 different experiments; Neon clusters size, Laser Pulse duration scan and Xe doping dependence. The VMI voltages keeps the same rate and the MCP and PHS voltages will be specified in each section. The pressures in the detection chamber oscillated during the experiments around $6 \cdot 10^{-8}$ mbar with the chopper open (Cluster beam in).

Neon cluster formation presents a technical challenge due its solidification curve, at this backing pressure, small changes on the nozzle temperature leads to solidification of the gas and nozzle clogging. Another difference between neon and helium, is that neon clusters after the supersonic expansion are in a solid state and in consequence the dopant sit in the surface of the cluster [53]. to determine the cluster size we use the Hagen scale with $\langle N \rangle = 33(\Gamma^*/1000)^{2.235}$ [29] with $\Gamma^* = k \frac{p_0 d^{0.85}}{T_0^{2.29}}$ based on the work of *Karnbach et al* [?], where p_0 is the stagnation pressure, d is the diameter of the nozzle, T_0 is the temperature and k is the gas condensation constant, For Ne $k = 185$ [?].

Fig 4.24 show a compilation of the raw VMI signals of neon plasma for different sizes and doping levels. In general all pictures have a similar distributions to the helium clusters. Fig. b, c and d represent a typical signal for doped small clusters. The most common signals shapes are small and medium size bright circles with low intensity. Additionally, there exist a small defect in the detector in the center-upper-right, where the brightness intensity decrease in all signal. It is cause because the large amount of electrons collected during the days burned the phosphor layer decreasing its detection efficiency, leaving a blind spot. Fortunately it is

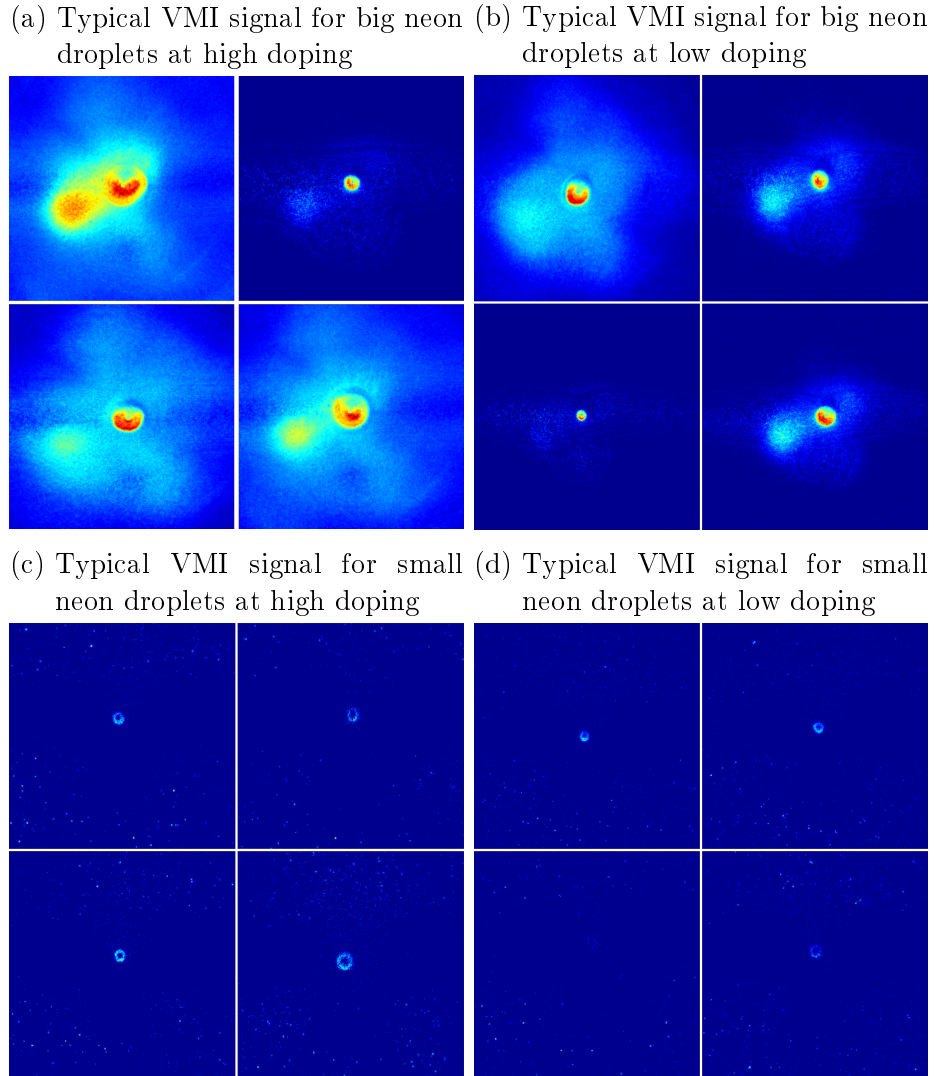


Figure 4.24: Sample signals for the Neon nanplasma for different sizes and doping levels.

a systematic error and for future experiments we will just need to replace the screen. Additionally Fig 4.24 a. represents a typical signal of larger droplets. These huge signals have unusual shapes with elongations on the central feature and anisotropic high brightness that starts saturate the camera. Although, this signals was not a significant percentage of the results, they did appear regularly. One explanation for its irregular outline is assuming big clusters with irregular shapes. As Neon clusters are solid, it is possible that the bigger clusters will not condensate uniformly and in consequence they will create anomalous signals. Subsequently, this big droplets will be analyzed independently and will not be taken into account in the next sections but gives us an interesting landmark in the study of Ne plasma.

Nevertheless, Fig 4.25 shows a similar energy distribution as founded in He clus-

ters. Fig a. show a summed and averaged VMI picture of the bigger droplets, the with circles correspond to the energies draw in dash lines on the roght plot. Fig b. show the energy distribution for the averaged signals at different Xe doping levels, presenting one clear peak at 0.3 eV that coincide to the edge of the central feature in the raw image. The second dash line show the energy at the end of the consecutive plateou at 15 eV, describing also the edge of the signal cloud around the central brigt circle similar to the describe in the He clusters examples.

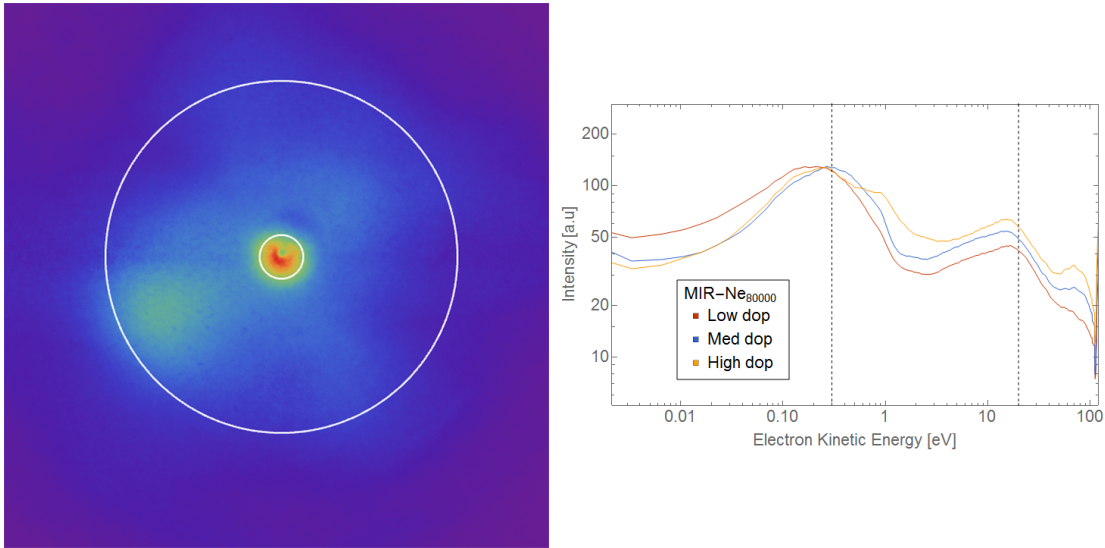


Figure 4.25: On the left, The number of electron histograms for differnet Xe doping levels. On the right the energy histograms. The dashed line represents the minimun energy detected by the bloop finder algorithm.

4.3.1 Doping Dependence

In this experiment small Neon clusters where doped with Xenon at different doping levels. The Neon clusters were created at the same nozzle temperature $T_{nozzle} = 39$ K ($\langle N \rangle_{Ne} = 3.3 \cdot 10^4 \pm 1.5 \cdot 10^3$) and at a backing pressure of $P_0 = 10$ mbar. Xenon were introduce at 7 different pressures measured in the oven chamber. The VMI voltages were set to VMIx1 (see table 2.1) and the MCP and PHS to 1800 V and 4000 V respectively. The camera was stablish to an exposure time of $t_{exp} = 34 \mu s$ and the laser power were set to an average power of 10 W.

Fig. 4.26 shows the histogram for the number of electrons and the Max energy. On the right, the histogram show a close distribution with shifting peaks from 0.05 to 0.1 eV and a drastic decrease up to 0.2 eV. The max counts increase regularly with the doping level until the purple line with Xe_{202} and for higher doping the counts starts to reduce.. On the electrons histogram, a broader distribution is shown with a

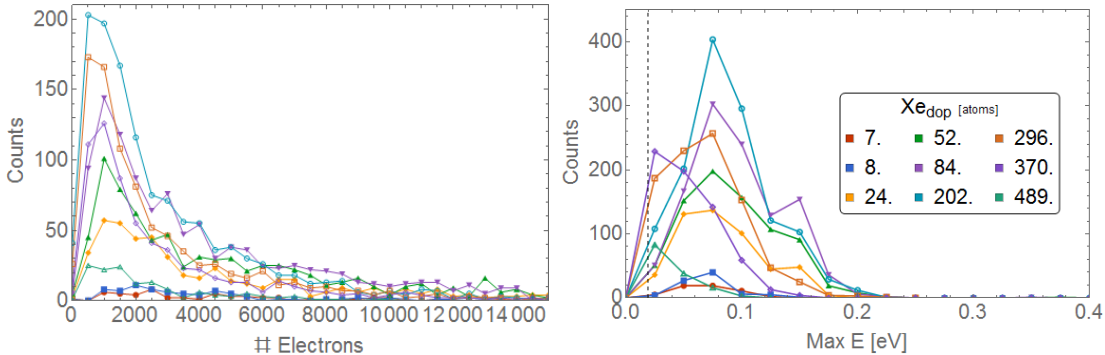


Figure 4.26: On the left, The number of electron histograms for differnet Xe doping levels. On the right the energy histograms. The dashed line represents the minimun energy detected by the bloop finder algorithm.

systematic peak at 3000 electrons, it means that the mean signal found, correspond to small clusters, even though massive signals up to 30000 electrons can be found.

Fig 4.27 top, shows the signal rate for the different pressures and the energy distribution for all doping levels. As notice on the left of the plot, the nanoplasma signal rate increase rapidly with the doping, until the best doping at $5 \cdot 10^{-5}$ mbar and keep constant for higher doping. This agrees to our previous results showing there exist a minimum doping level to have the most efficient plasma creation, and stronger doping does not help to have more signal. On contrary, for the highest doping levels we denote a small reduction in the signal rate showing that at this level, the clusters starts to be destroyed, and the signal rate goes down. On one hand, The mean values shows a constant increment in the energy for the first pressures, going in agreement with the signal rate, in other words, adding more dopant to the Neon allows to achieve higher energies, but after reaching the doping limit pressure, a decrease in the mean energy appears. On the other hand, for the mean number of electrons, we see that for the first doping, the mean value keeps quite constants, but once we go upper the $5 \cdot 10^{-5}$ mbar, the mean electron decrease but the signal rate keeps high. This results shows that the doping increase the efficiency to ignite the nanoplasma, but at large doping level the mean value of electrons decrease, meaning that we are igniting small droplets. In short, is more efficient to ignite bigger droplets than small ones, because according to the data, the small ones need a larger amount of doping to be ignited while the large cluster just need a few atoms.

4.3.2 cluster Size Dependence

In order to understand the nano plasma explosion in Neon cluster, this experiment was done on different Neon cluster at a fix doping level with Xenon. The Neon clus-

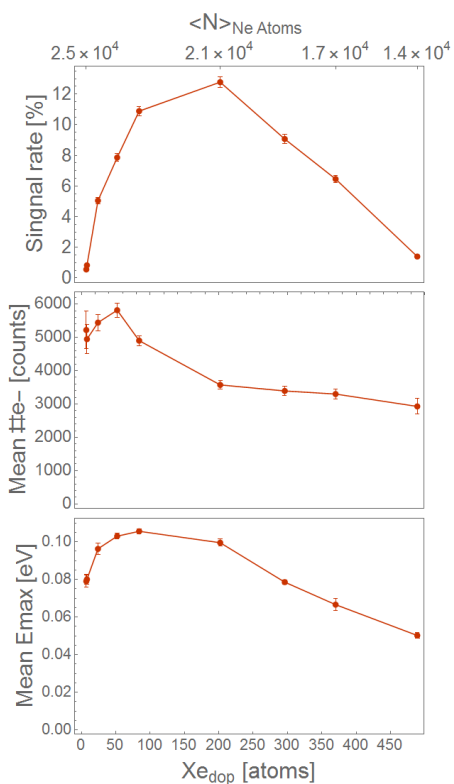


Figure 4.27: On the top, signal rate for the Ne-Xe doping dependence. On the center and bottom, the mean values for the #e- and max energy depending on the laser pulse.

ters were created at 5 nozzle temperature 39, 40, 41, 42 and 44 K with a stagnation pressure of $P_0 = 10$ mbar. Xenon were introduce at a fix pressures measured in the doping cell of 0.00036 mbar. The VMI voltages where set to VMIx1 and the MCP and PHS to 1800 V and 4100 V respectively. The camera was stablish to exposure time of $t_{exp} = 34 \mu\text{s}$ with the single shoot measurement scheme. The laser power were set to an average power of 11 W.

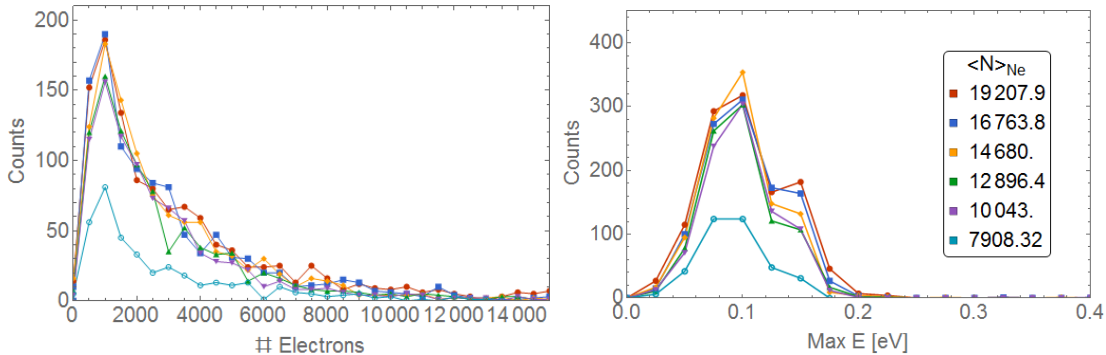


Figure 4.28: From left to right, the number of electron histograms and the energy histograms for the different number of atom $\langle N \rangle$ in the neon cluster.

Fig. 4.28 shows the histogram for the number of electrons and the max energy. On the right, the histogram have similar distribution independent of the cluster size, the biggest droplets present almost the same tendency just varying the peak count centred on 0.1 eV. On contrast, the light blue line is the only cluster size with a signification count change. Furthermore, on the left, the electron count histograms present similar trends with a peak around 1000 electrons, analogous to the histogram in the He-Xe doping. The counts just decrease due the signal rate as show in Fig 4.29, and slightly difference in the broaden at bigger droplets.

Fig 4.29 shows the signal rate and the energy distribution for the different nozzle temperatures. On the left, the signal rate shows an expected result where the bigger droplets present the higher rates and it decrease with the cluster size (high temperatures). The mean values show in Fig. 4.29 center and bottom, have a trivial behaviour, congruent to the signal rate, both, mean number of electrons and Max energy, show an increase with the cluster size. Again as in the He size dependence, the bigger droplets have more electrons to be detected so this relation is expected.

4.3.3 Neon Pulse Duration Dependence

The last measurement done in ELI-Alps was a laser pulse duration dependence. Neon cluster at a fix doping level with Xenon at backing pressure of $P_0 = 10$ mbar and nozzle temperature 39 K ($N_{Ne} = 3 \cdot 10^4 \pm 1.5 \cdot 10^3$ atoms), were shoot by the

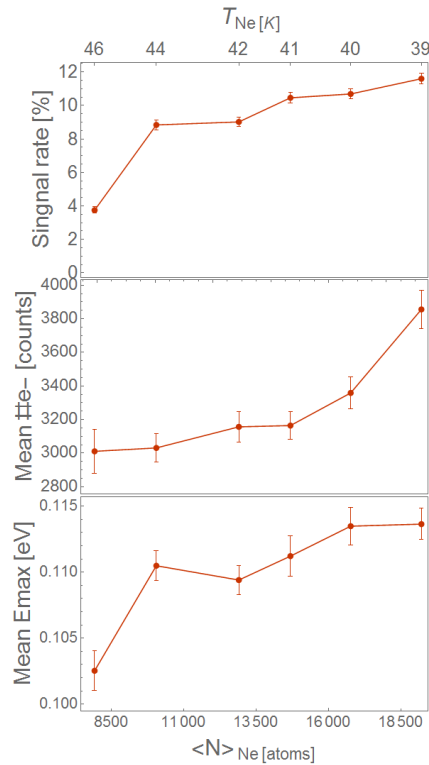


Figure 4.29: On the top, signal rate for the Ne-Xe doping dependence. On the center and bottom, the mean values for the #e- and max energy depending on the number of atoms $\langle N \rangle$ in the neon cluster.

Pulse duration [fs]	Power[W]	Laser intensity [W/Cm ²]
48	10.5	2E14
55	11	1.7E14
64	11	1.5E14
71	10.4	1.3E14
94	8.6	1E14

Table 4.4: Neon pulse scan intensity table.

MIR laser pulse at 5 different pulse duration of, 48, 55, 64 71, and 94 fs. Xenon were introduce at a fix pressures measured in the doping cell at 0.0002 mbar. The VMI voltages were set to VMIx1 and the MCP and PHS to 1700 V and 4000 V respectively. The camera was stablish to exposure time of 34 μ s with the single shoot measurement scheme. As in section 4.2.5 the pulse duration have a recurrent effect in the laser power, Table 4.4 shows the different powers and consecutive the laser intensities at each data set was taken.

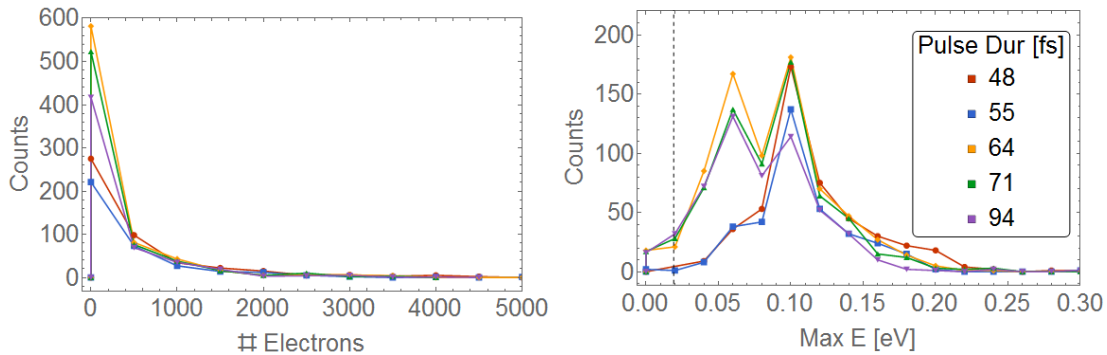


Figure 4.30: From left to right, the number of electron histograms and the energy histograms for the different laser pulse duration. The electron are binner every 1000 whilete the energy histograms is binned every 0.02 eV

Fig. 4.30 shows the histogram for the number of electrons and the max energy. On the right, the histogram have difrentt distribution dependent of the cluster size. As seen, the longer pulser reach a broader range of energy in contrast to to the shorter pulses which have a clear and define peak centred at 0.1 eV. the initial positive slope is stiffer for the longer pulses who reach a first peak at 0.05 eV and decrease after 0.15 same as the shorter ones. Furthermore, on the left, the electron count histograms present a new trend with a peak distribution close to 0 e- for all pulses, what means that most of the signals have a extream low brightness and have a number of electrons lower than 1000.

Fig. 4.31 present the signal rate and mean values for the different pulse duration. Here the signal rates shows the same tendency that sec 4.2, The pulse duration

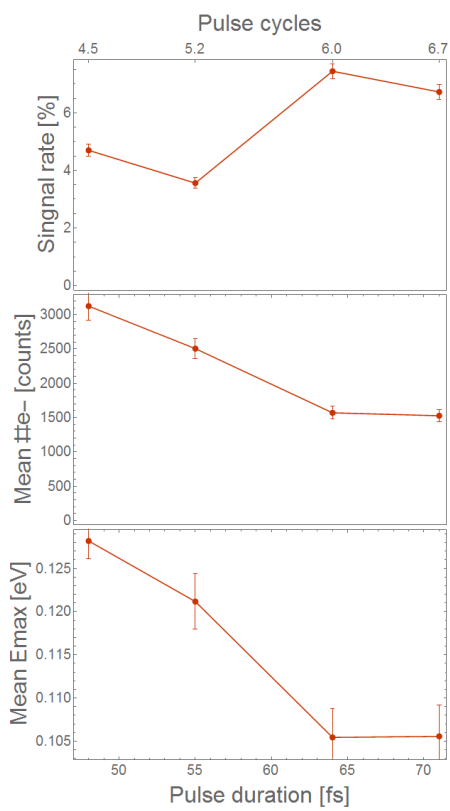


Figure 4.31: On the top, signal rate for the Ne-Xe doping dependence. On the center and bottom, the mean values for the #e- and max energy depending on the pulse duration.

plays an important role in the nanoplasma ignition, and the probability to create nanoplasma decrease constantly with the pulse, in this case, almost having no signal for pulses longer than 100 fs. Surprisingly in the mean values for the electron numbers and energy also shown a strong relation to the pulse duration. As table 4.4 reefers, the intensity that the laser gave were almost the same, so the variations in the mean values confirm that at longer pulses the rates to ionize bigger droplets increase. So as shown, we can see the same effect regardless the cluster element and doping level. For understand this result we need to picture how the stretch of a pulse will derive in more cycles in it. The first cycles will be determinant for the Ionization of the dopant, the electrons create in the beginning of the pulse will have more time to interact with the laser field, and in consequence they will acquire more energy and time to interact with the cluster. Once we stretch the pulse, the electrons produced in this first cycle will see more cycles, and the ionization of the cluster will be more efficient.

5 Summary and Discussion

In the proceeding chapter a detailed description of the data at similar parameters is discuss, followed by the relation of the energy distribution dependence with the number of electrons, relating it to the analytical model described in section 1.4.4.

First, we will compare the helium clusters in NIR and MIR for their pulse duration and laser intensity and subsequently compare it to the dopant elements and its role in the efficiency of the plasma formation. Additionally, a He-Ne clusters size in MIR discussion is presented to analyze the role of the cluster element at different sizes and dopants. We will pay special attention to the Xe-Ca doping experiment in He clusters to analyze the efficient of having two different dopants.

Finally, in order to relate the data to the analytical model, the number of electron with the max energy of the single coulomb explosion were correlated in each data set to associate them to energy distribution of the uniform charge spherical model. For this, we assume that the maximal kinetic energy detected is given by the position of the electron at the outer radius of electronic cloud before the cluster coulomb exploded, and the number of electron are related to the electron charge density. The result, is a simple probability density distribution that helps to pursue an educated guess of the plasma process energies without having to do costly and time consuming simulations. Finally, we present a summary and outlook of the results of this work and the possible outcome for the suture.

5.1 Laser parameters dependence on clusters

As shown, He cluster were ignites in NIR and MIR lasers at different laser intensities, additionally, Ne and He cluster in the same MIR field were ignited at different pulse duration. Here we present a comparison of the He at similar cluster sizes and the Ne and He cluster at the different pulses.

Fig 5.1 shows the comparison for the experiments with different laser intensity and pulse duration. On the left we show the signal rates and mean values for the different laser intensities using He clusters interacting with the MIR and NIR laser. On one hand, there exist a linear dependence where the intensity increase

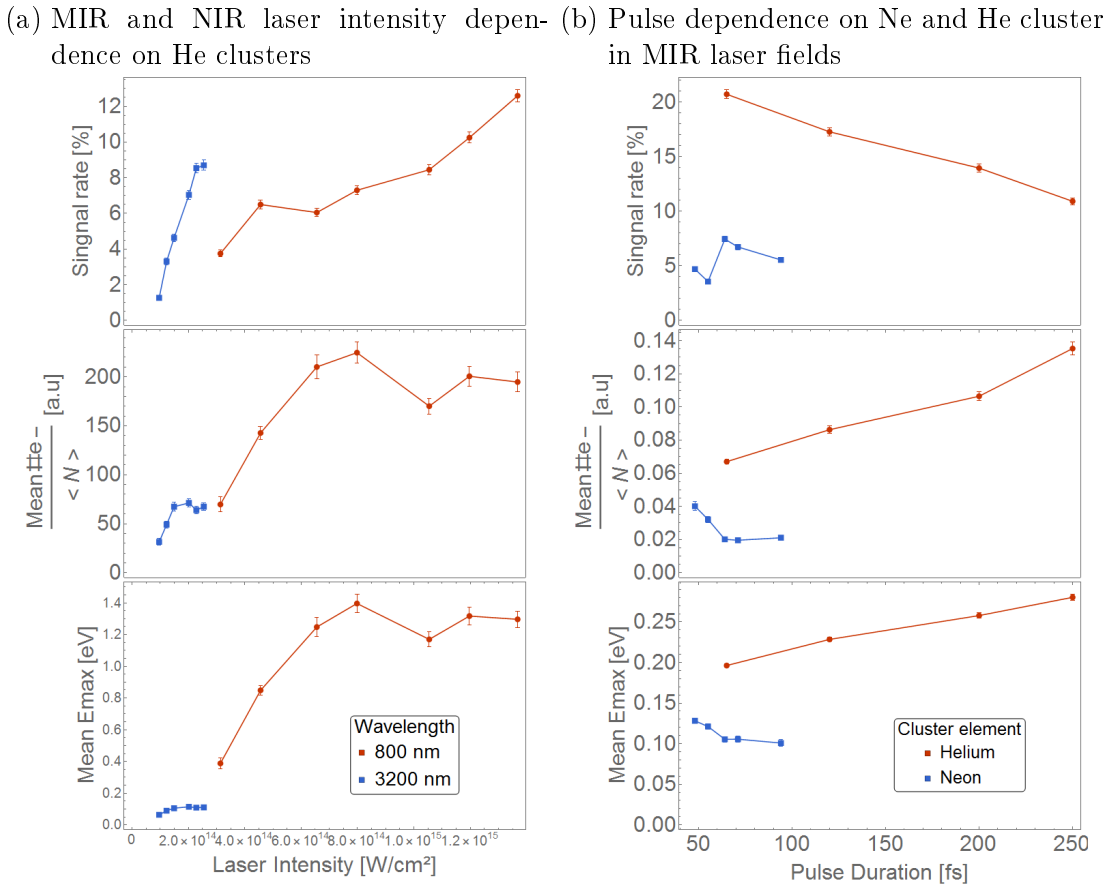


Figure 5.1: Comparison of the pulse duration and laser intensity. On the right, the pulse duration dependency for the signal rate and mean values of He and Ne clusters. On the left, the laser intensity dependence for He cluster in NIR at 800 nm wavelength and MIR at 3200 nm wavelength. The mean number of electron is normalized to the cluster size in both cases.

the signal rate drastically, with both lines (blues and red) having a zero signal close to $8 \cdot 10^{13} \text{ W/cm}^2$. As expected, there exist a minimum beam intensity to achieve plasma formation because the main energy transfer from the photons to the clusters is done via ionized dopant electrons that initiate the electronic cascade and forms the coulomb explosion. If the initial energy is not enough to ionize the dopant, none electrons will interact with the laser field and the plasma will not be created. On contrast, the signal rate in the MIR can be comparable to the NIR even at lower intensities, for example, He rate for the blue line at $2 \cdot 10^{14} \text{ W/cm}^2$ is the same as the point at $8 \cdot 10^{14} \text{ W/cm}^2$ in the blue curve. It also can be related to the doping level and the slightly size difference in each easement but both lines have a parallel behaviour that confirm our assumption

On the other hand, despite the normalization at the cluster size, is clear that the NIR field produce more electrons at higher energies, reaching energies one order

of magnitude higher than the MIR. This could be interpreted that the 800 nm wavelength range in the plasma resonance and the cluster is ionized completed, even for the biggest droplets, as shown in the plateau for intensities upper than $1 \cdot 10^{15} \text{ W/cm}^2$. In contrast, assuming a complete ionization and that the detector can reach almost all electrons coming out of the explosion, in the mean number of electrons the blue curve does not have such high values as the red, what could indicate that the plasma formation in MIR laser fields is incomplete or partial.

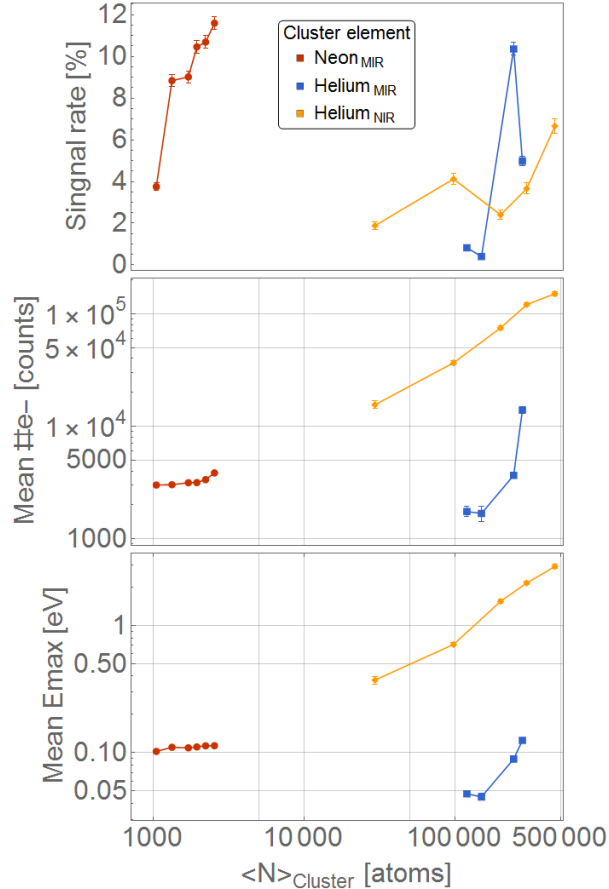
Fig 5.1 b. shows the pulse duration dependence of big He and Ne cluster in the MIR laser. Although in Ne a vast part of the pulse measurement is missing, we still see some relation in the points around 60 to 100 fs. On top, the red signal rate presents an expected decrease in accordance to the laser intensity plot, the longer pulses have lower intensity, in consequence the signal rate goes down. Same happens for the blue curve, that in the 60 to 100 fs range where it behaves parallel to the He line. In contrast, a surprising result is shown in the mean values contrasting to the intensity dependence results. It shows that at longer pulses higher energies and electron numbers are achieved, in other words, it enhances the plasma formation for bigger droplets. Although, it is a non-intuitive result, it can be explained if we take into account that for longer pulses we have more cycles in the pulse. In consequence, even the initial ionization probability is lower for the first cycles, the electrons created on them will have more time to interact with the laser field, acquiring energy and boosting the electronic cascade to end in the coulomb explosion.

5.2 Cluster Size Dependence

As shown in fig 5.2 the droplet size plays an important role in the nanoplasma explosion. All clusters have a common linear behaviour linked to the cluster size, the bigger the cluster more signal can be found. On one hand, Ne cluster shows a more stiff tendency, its signal rates goes from 4 to 12% in small droplets compared to the He_{NIR} at the smallest size does not go up the 3%. Moreover, either He_{MIR} and He_{NIR} have a continuous growth for cluster around a few hundreds of thousands. In contrast at the biggest He_{MIR} cluster shows a depletion of the signal, suggesting that exists a maximal cluster size where that MIR laser is not efficient any more, contrary to the NIR where at the same size, presents an enhancement of its efficiency and for huge clusters reaches a maximum according to the data.

On the other hand, the mean values show a similar behaviour in the MIR independent of the cluster element, lines blue and red, have similar values, having an initial constant trend and the bigger sizes have higher counts, yet in contrast the

Figure 5.2: Cluster size dependence of He and Ne cluster in MIR laser fields (yellow and blue), and He cluster in NIR laser (Red) the mean values are in logarithmic scales and the signal rate in linear scale.



mean number of electrons for the smallest droplets reach counts 2 order of magnitude lower. Same happens in the mean energy where the bigger droplets show higher energies, and all lines shows a similar trend. The reason for this tendency is not clear, but if we assume the interaction dopant-cluster, small cluster could have a high probability of losing the ionized electrons in the beginning of the pulse, so the ignition process is less efficient. However, for the bigger clusters, the ionized electron have more atoms to interact, so the losses reduces and in consequence the bigger clusters can be more efficient to create the nanoplasma. The reason for this tendency is not clear, but if we assume the interaction dopant-cluster, small cluster could have a high probability of losing the ionized electrons in the beginning of the pulse, so the ignition process is less efficient, while for the bigger clusters, the ionized electron have more atoms to interact, so the losses are less, and in consequence the bigger clusters are more efficient to create the nanoplasma.

5.3 Doping Dependence

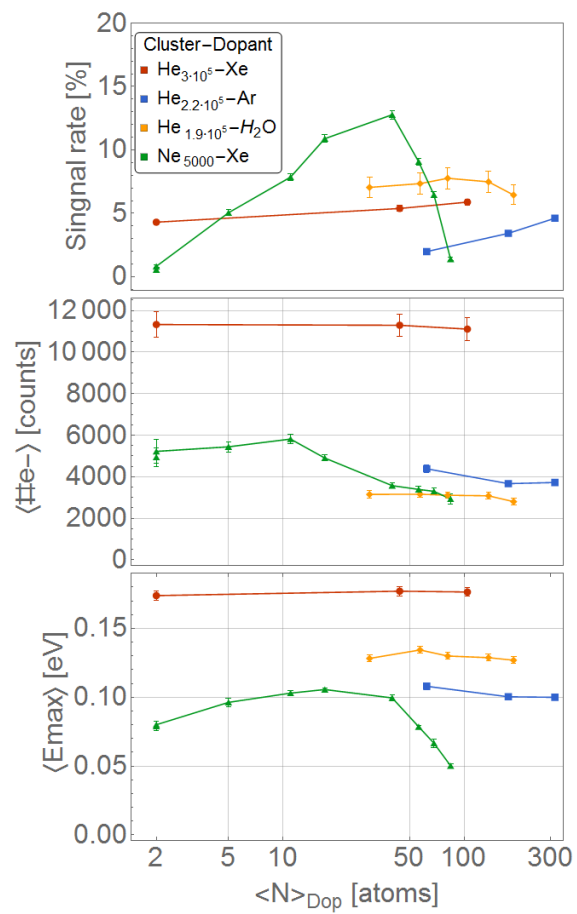
Fig 5.3 shows an overview of all the mean values and signal rate for the He droplets with Ar, Xe and water, and Ne doped with Xe at different doping levels. On top the signal rate shows for $\text{He}_{2.5.10^5}$ similar values for low and high dopant. In contrast for the Ne_{5000} at extreme low levels the signal rate goes to zero. This lack of dynamics is an expected result, as explained, the MIR laser field does not have enough energy to ionize directly the He or Ne, so a dopant with a lower IP is needed in order to start the process. Once the process is started and the electronic cloud is formed, the extra electrons given via the dopant ionization does not change the final result. The green line, Ne-Xe, is the only graph that have important changes. It suggests that the difference on cluster size between the Ne_{5000} and $\text{He}_{2.5.10^5}$ affect the cross section to get dopants and in consequence a minimum cluster size-doping pressure relation need to be achieve to effectively pickup Xe and so the plasma formation can start. This results shows that the doping can increase the efficiency to ignite the nanoplasma, and at large doping level the mean value of electrons decrease, meaning that we are igniting small droplets. In short, is more efficient to ignite bigger droplets than small ones, because according to the data, the small ones need a larger amount of doping to be ignited while the large cluster just need a few atoms.

The mean values also shows a similar dynamics with steady He clusters independent on the dopant or the dopant level for He, while the Ne cluster present a constant grow for low doping levels showing a plateau around 50 atoms and a depletion for higher doping. It's clear that, for the Ne line, the increase of dopants leads to an increase on the plasma formation, yet in case the dopant is to large, can be totally destroyed due the evaporation and cluster shrinkage, similar to the reports in other experiments [?]

Fig 5.4, 5.5 and 5.6, shows the signal rate and mean values interpolation for the combination of Xe and Ca in He droplets in the MIR laser. The dashed color line are cuts at a constant dopant numbers, Xe+Ca at 40, 50, 65, 85, 100, 120 and 150 atoms. The lines were choose in order that it lays between 3 data points, so the interpolation is accurate enough. On the right of each figure the cuts are plotted depending on the Xe atoms. It means that the right side of each line represent the doping with the maximum Xe atoms at the Xe+Ca constant, once we go from right to left, we replace each Xe atom for one Ca atom until all Xe atom are replaced. Each line have a maximum of 40 points, because it was the max Ca doping measured with enough statistics.

An important result can be derived from Fig 5.4, as shown in the cut lines at constant total doping, we found a increment in the signal as the Ca doping replace

Figure 5.3: doping level dependence of He and Ne cluster in MIR laser fields doped with water, argon, and xenon in MIR fields.



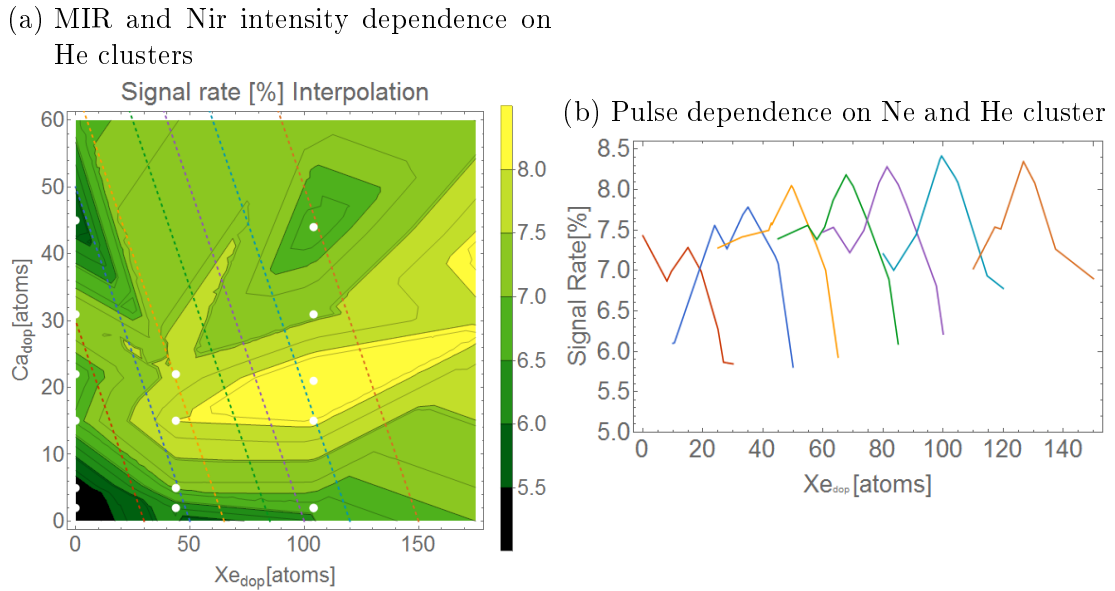


Figure 5.4: On the left, signal rate interpolation for He cluster doped with Xe and Ca at different doping levels. The white points correspond to the actual measurements and the dashed line the cuts at constant number of dopant atoms. On the right, the cuts for at a constant dopant numbers, Xe+Ca at 40, 50, 65, 85, 100, 120 and 150 atoms for the corresponding color lines.

the Xe. In all line, from right to left, the signal rate goes up when a few atoms of Ca are added despite the amount of Xe. It demonstrate a better efficiency in the doping for Xe-Ca combination compared to only Xe or only Ca. This tendency can be spot not just on the big peak in the interpolation between 70 to 120 Xe atoms and 15 to 25 Ca atoms, but also in each of the cuts, where the lines clearly display a peak, the signal rate increase faster for these extra Ca atoms added. Once a saturation maxima is reach, the extra Ca atoms added makes the signal rate again decrees but in a slower way in most of the cases.

Fig 5.5 show one clear peak at low doping where the maximum number of electrons appears, then for higher doping the counts starts to decreases and even a small depletion is shown in the range of Xe=100 Ca=20 atoms. On the right, the cut at constant dopant is show, the color from left to right represent the same cut done in the corresponding interpolation, and it's necessary to read it at the same way. Where the right side of each line represents just Xe doping and each number to the left mean replacing one Xe atom for one Ca atom. As show, the exist also a recurrent peak efficiency in the nanoplasma ignition, meaning that at this peak the larger cluster are ionized, similar as shown on the Pulse duration scan.

Equally important. In the E_{max} interpolation, a clear peak is also shown at Xe=50 and Ca=7 atom, This can be found in interpolation cuts, where the highly doped

(a) MIR and Nir intensity dependence on He clusters

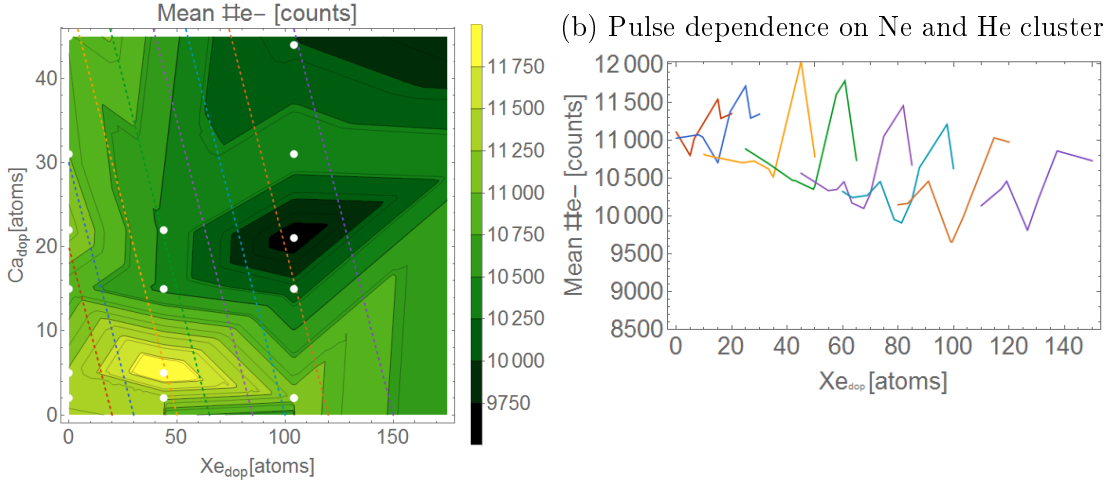


Figure 5.5: On left, the mean number of electrons interpolation for He cluster doped with Xe and Ca at different doping levels. On the right, the cuts for at a constant dopant numbers, Xe+Ca at 40, 50, 65, 85, 100, 120 and 150 atoms for the corresponding color lines.

(a) MIR and Nir intensity dependence on He clusters

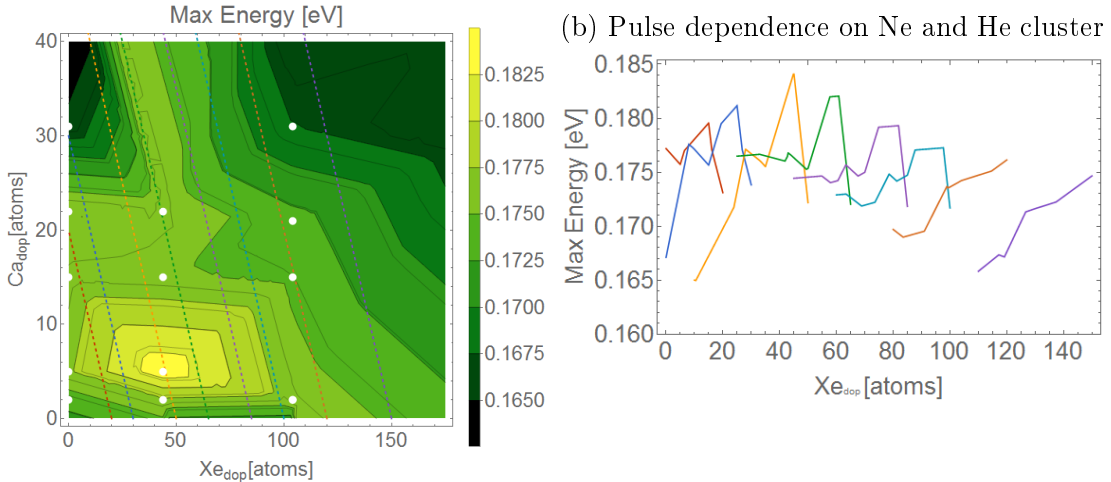


Figure 5.6: On left, the mean max energy interpolation for He cluster doped with Xe and Ca at different doping levels. On the right, the cuts for at a constant dopant numbers, Xe+Ca at 40, 50, 65, 85, 100, 120 and 150 atoms for the corresponding color lines.

lines have a more constant performance and no real change is shown, but once we get close to the optimum doping (Yellow line), the replacement of Xe atom for Ca atoms becomes drastic effective, with a peak founded close to 0.2 eV. This measurement can be compare directly to the water doping scan where we show that once the

ignition of the cluster starts, adding more water atoms does not creates changes in the process. Here, Xe doping results in a similar behavior, the points with just Xe atoms (Right edge of each colored line) have a relative constant mean energy, but once we introduce the Ca, dynamics start to appears, given a peak close to the Mean electrons interpolation. For the heavily doped clusters, on the blue, orange and purple cuts in the right, we see that the peaks are not present any more due the cluster destruction when to many atoms are added.

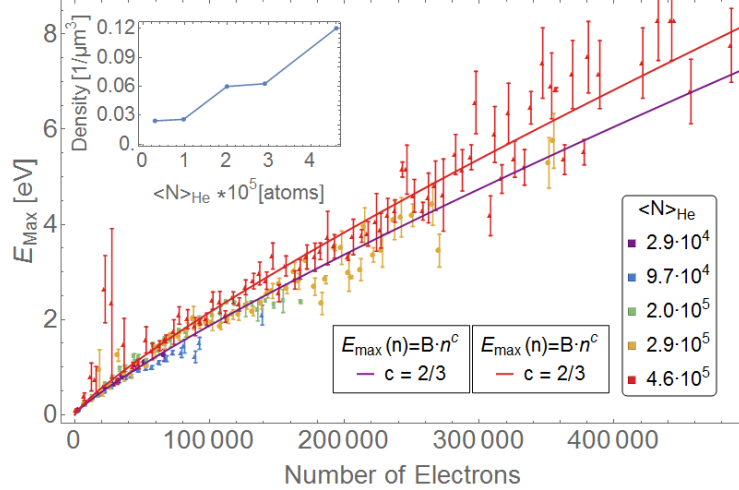
5.4 Electron-Energy Distribution

Once the number of electron and max energy was extracted from each VMI picture, an energy distribution depending on the electrons detected can be plot to fitted to the uniform charge spherical model explained in chapter 1. The next figures will display the binned correlation for the max kinetic energy and number of electrons with their correspondent fit based on $E_{max} = B \cdot n^{2/3}$ Eq. 1.30, where n is the number of electrons and B is the B-factor related to the electron density in the electronic cloud. The error bars are the standard derivation for the binned section and in case there is just one point in the binned region the error was assigned to the resolution of the experiment.

Fig ?? presents the data for He droplets in NIR laser fields for the cluster size dependence and the laser intensity measurements. Fig a. shows the binned energy distribution for the different droplets sizes. The red and purple line is a fit based on Eq. 1.30 where B is the B-Factor and n is the number of electrons, the $2/3$ factor is fix to the fitting. The red and purple line correspond to the biggest and smaller droplets respectively, and all other fit lines showed the same tendency fit quite well to the data points. For the B-factor at $N_{e,6 \cdot 10^5}$ the corresponding electronic cloud density is around $\rho = 2.2[1/\mu\text{m}^3]$, what leads to an electronic cloud radius of $4.3 \mu\text{m}$. In Fig b. the same process is done for each of the data sets at different laser intensities. All fits have the same tendency regardless the laser intensities, changing slightly on the B-factor. This in an important outcome meaning that the data fits quite well to our simple spherical electronic cloud model. As the B-factor is directly related to the density of the electronic cloud using Eq. 1.3 is possible to delimit the radii of the electronic sphere. In other words, according to this model, if we know the total number of electrons it's possible to calculate the maximal energy that we can detect. For the B-factor at $1.4 \cdot 10^{15} \text{ W/cm}^2$ the corresponding electronic cloud density is around $\rho = 0.02[1/\mu\text{m}^3]$, what leads to an electronic cloud radius of $136 \mu\text{m}$. The Inset on the top-left cornet shows the electron density for each of the laser

intensities and cluster sizes, showing a strong dependence quit the cluster size as expected but a similarity with the signal rate intensity dependence with a plateau in the higher laser intensities.

(a) He cluster size dependence energy distribution in NIR laser pulses



(b) Helaser intensity Dependence Energy distribution in NIR laser pulses

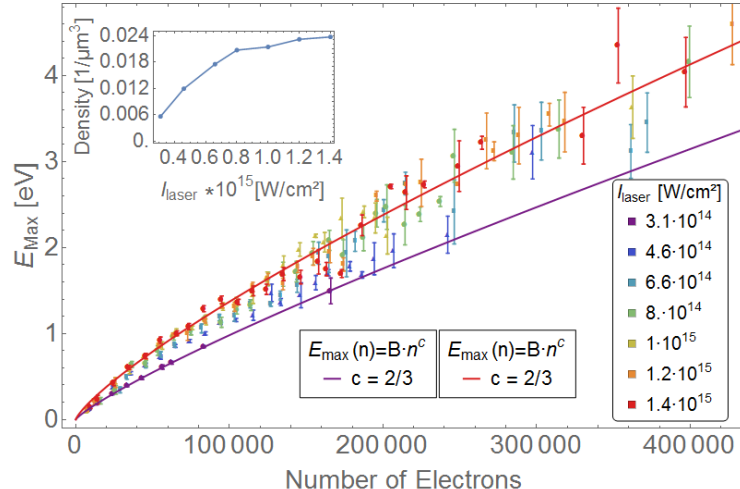


Figure 5.7: Energy distribution related to the number of electron for He clusters in NIR laser fields at different Cluster size fig a. and laser intensity Fig b.

Fig 5.8 presents the data for He droplets in MIR laser fields for the cluster size dependence and the Pulse Duration measurements. Fig a. presents the binned maximal kinetic energy distribution for different droplet size, the color points shows the different cluster sizes with the standard dispersion as error bars. The continue lines are fit lines with c exponent fixed to 2/3. It is clear that the continue lines deviates from the data, meaning that the spherical model cannot be applied for these measurements. Moreover, the dashed line is a fit based on the same equation

but with the exponent c free. As seen, this lines have a better agreements with the data, even though the analytical model cannot be applied in this case, there exist a clear correlation of the energy and number of electrons that a refinement of the model could solve in a future. This new exponent is persistent in all the fit for the MIR experiments in helium. Fig B show another example where the spherical model (continues lines) fails and a better fit with the c match the data (dash line)

There is no theoretical background that can predict this behaviour, one of the possible explanation, taking into account that the exponent is closely linked to the geometry of the cloud, is that the big droplets are not perfectly spherical, for example, because He is liquid, the droplets could turn in an ellipsoidal shapes. . A second reason can be because of the partial coulomb explosion described in the previous section. As describe, not all the cluster is generating a plasma and just part of it generates a nanoplasma, so the final electronic cloud will present abnormalities making its density and shape non uniform. Although our analytical model cannot describe precisely the energy distribution it is clear that the number of electron and max energy have a close relation and even the model does not fit, it can be possible to introduce some correction in the future to have a better model

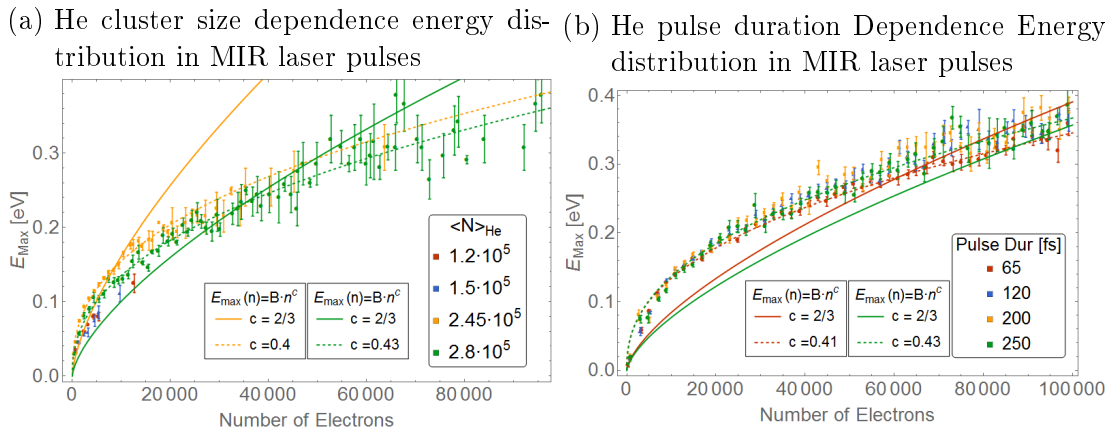


Figure 5.8: Energy distribution related to the number of electron for He clusters in MIR laser fields at different Fig. a. and cluster sizes and pulse duration Fig. b.

Fig 5.9 presents the data for Ne droplets in MIR laser fields for the cluster size dependence and the Xe dependence measurements, with c and B factor set free. In Fig a. The fit function are done for the shorts pulse with the c exponent at $2/3$ and as a free parameter. Once again the model does not fit but a clear energy distribution is present independent for the pulse duration. The dashed line follows $B = 0.03$ and $c = 0.23$ and is shared for the other data sets. Figure b. shows the Energy distribution with a similar trend, the data point and signal presents the

same energy distribution as shown in the pulse scan. The fit function was done in the same way. The model fit shows and proximate better agreement to the first data point at lower energies but diverge rapidly to the bigger ones. The dash fit on the contrary show that the energy distribution follows a similar trend independent to the cluster size, but our spherical model cannot be applied.

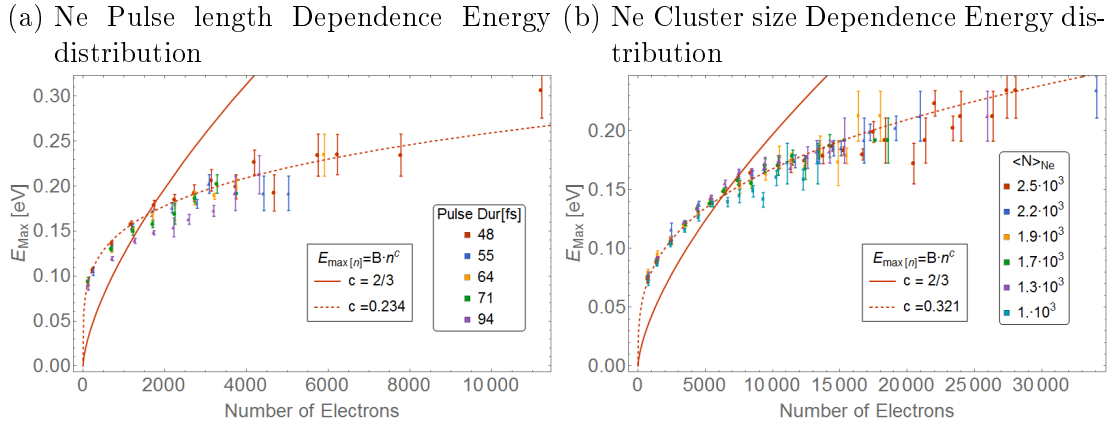


Figure 5.9: Energy distribution related to the number of electron for Ne clusters in MIR laser fields at different pulse duration fig a. and cluster sizes Fig b.

List of Figures

1.1	Helium phase diagram	10
1.2	Scheme for a nozzle expansion	11
1.3	Waan der Wall He-He potential	11
1.4	helium isentropic diagram	12
1.5	Phase diagram for Expansion regimens	13
1.6	Expansion droplets Regimens	14
1.7	Neon phase-Isentropic diagrams	15
1.8	Helium creation, doping and evaporation sketch	17
1.9	Relaxation processes for photoionization	20
1.10	Ionization regimes	21
1.11	Ponderomotive 3 steps	24
1.12	Cluster potential regimes	26
1.13	sketch of the Coulomb explosion for a doped cluster due the excitation of a pulsed laser field. At the beginning of the process the laser ionized the droplet, until some femtoseconds (up to 500fs) after, the system collapse and result into a coulomb explosion.	27
1.14	Islam Model fit	30
2.1	Sketch of the vacuum chambers, including the main parts of the setup	32
2.2	Cut of the Oven design, including part of the rod and the crucible	34
2.3	Representation of particle trajectories A, B and C of the ionization volume to the detector plane, which, in spite of initially different velocity the finish on the same point of the detector plane. Withdrawn from [21]	36
2.4	At the top of the graphic some basic functions f_k in different colors, which can be used for the Inverse-Abel transform in the Basex method. On the bottom, the corresponding Abel-transformed functions Fk. Taken from [21]	37
2.5	MCP sketch cut	38
2.6	TOF cup	39

3.1	VMI raw images example	42
3.2	Trigger Scheme	43
3.3	Correlation signals example	44
3.4	energy calibration of the VMI spectrometer with SIMION. Electrons with discrete kinetic energy are emitted perpendicular to the spectrometer axis.	45
3.5	(a) Photoelectron image of potassium excited and ionized by linear polarized 404nm light, (b) Abel inverted image and (c) corresponding photoelectron spectrum, not yet calibrated on the energy	46
3.6	Abel inverse transform example	48
3.7	Difference of mean pixel values to determine the radius of the central feature in the VMI images	50
3.8	Fit-Abel transform agreement	51
3.9	Example signal finder	51
4.1	examples NIR signal	53
4.2	Average energy distributions in NIr	54
4.3	NIR He Intensity dependence. Histograms	55
4.4	NIR He intensity dependence. Signal Rate and Mean Values)	57
4.5	NIR He droplet size. histograms	57
4.6	NIR He intensity dependence. Signal Rate and Mean Values)	58
4.7	MIR He raw images	60
4.8	MIR He droplet scan histograms	60
4.9	MIR TOF spectra He	61
4.10	MIR He droplet scan histograms	62
4.11	MIR He droplet size dependence	63
4.12	MIR He Doping examples	64
4.13	MIR He-Ar. Histograms	64
4.14	MIR He-Ar doping, signal rate and mean values	65
4.15	MIR He-Water. Histograms	66
4.16	MIR He-Water doping, signal rate and mean values	67
4.17	MIR He-Xe-Ca doping. Histogram	68
4.18	MIR He-Xe-Ca doping. Interpolations	69
4.19	MIR He laser parameter examples	70
4.20	MIR He-intensity dependence. Histogram	71
4.21	MIR He intensity dependence	72
4.22	MIR He-intensity dependence. Histogram	73
4.23	MIR He pulse scan. Signal rate and mean values	74

4.24	MIR Neon raw samples	76
4.25	MIR Ne-Xe doping scan.Histograms	77
4.26	MIR Ne-Xe doping scan.Histograms	78
4.27	MIR Ne-Xe. Signal rate and mean values	79
4.28	MIR Ne size dependence.Histograms	80
4.29	MIR Ne size dependence. Signal rate and mean values	81
4.30	MIR Ne pulse duration. Histograms	82
4.31	MIR Ne pulse duration. Signal rate and mean values	83
5.1	Laser parameter comparison	86
5.2	Cluster size comparison	88
5.3	Doping level comparison	90
5.4	Xe-Ca interpolation signal rate	91
5.5	Xe-Ca interpolation num electrons	92
5.6	Xe-Ca interpolation max energy	92
5.7	Energy-Number of electrons relation. NIR Helium Droplets	94
5.8	Energy-Number of electrons relation. MIR helium droplets	95
5.9	Energy-Number of electrons relation. Neon Droplets	96

List of Tables

2.1	Typical voltages for the different VMI settings	37
3.1	trigger Channel delays	43
4.1	NIR laser power to intensities	55
4.2	NIR Helium Cluster Size	58
4.3	cluster size reference	62
4.4	Neon pulse scan intensity table.	82

6 Bibliography

- [1] *Helium.* <http://ltl.tkk.fi/research/theory/helium.html>
- [2] BECKER, U. (Hrsg.) ; SHIRLEY, D. A. (Hrsg.): *VUV and Soft X-Ray Photoionization.* <http://dx.doi.org/10.1007/978-1-4613-0315-2>
- [3] A. BETHE, H. ; E. SALPETER, E. : *The Quantum Mechanics of One- and Two-Electron Atoms.* Bd. 35. <http://dx.doi.org/10.1007/978-3-662-12869-5>.
<http://dx.doi.org/10.1007/978-3-662-12869-5>
- [4] ATKINS, K. R.: *Liquid Helium.* Cambridge University Press. – ISBN 978-1-107-63890-7. – Google-Books-ID: gzmNAwAAQBAJ
- [5] AUGST, S. ; MEYERHOFER, D. D. ; STRICKLAND, D. ; CHIN, S. L.: Laser ionization of noble gases by Coulomb-barrier suppression. 8, Nr. 4, 858–867. <http://dx.doi.org/10.1364/JOSAB.8.000858>. – DOI 10.1364/JOSAB.8.000858. – ISSN 1520-8540
- [6] BERKOWITZ, J. : *Photoabsorption, photoionization, and photoelectron spectroscopy.* Academic Press. – ISBN 978-0-12-091650-4. – Google-Books-ID: POeHAAAAIAAJ
- [7] BLANCO, M. ; V. SHEVADE, A. ; A. RYAN, M. : Quantum Mechanics and First-Principles Molecular Dynamics Selection of Polymer Sensing Materials. http://dx.doi.org/10.1007/978-0-387-73715-7_3. – DOI 10.1007/978-0-387-73715-7₃, S.71 – – 92
- [8] BÜNERMANN, O. ; STIENKEMEIER, F. : Modeling the formation of alkali clusters attached to helium nanodroplets and the abundance of high-spin states. 61, Nr. 3, 645–655. <http://dx.doi.org/10.1140/epjd/e2011-10466-0>. – DOI 10.1140/epjd/e2011-10466-0. – ISSN 1434-6079
- [9] BUCHENAU, H. ; KNUTH, E. L. ; NORTHBY, J. ; TOENNIES, J. P. ; WINKLER, C. : Mass spectra and time-of-flight distributions of helium cluster beams. 92, Nr. 11, 6875–6889. <http://dx.doi.org/10.1063/1.458275>. – DOI 10.1063/1.458275. – ISSN 0021-9606, 1089–7690

- [10] CHRISTEN, W. ; RADEMANN, K. ; EVEN, U. : Supersonic Beams at High Particle Densities: Model Description beyond the Ideal Gas Approximation †. 114, Nr. 42, 11189–11201. <http://dx.doi.org/10.1021/jp102855m>. – DOI 10.1021/jp102855m. – ISSN 1089–5639, 1520–5215
- [11] CONNERADE, J. P.: *Highly Excited Atoms*. Cambridge University Press. – ISBN 978–0–521–43232–0. – Google-Books-ID: VgpkXDfkqYEC
- [12] DALY, N. R.: Scintillation Type Mass Spectrometer Ion Detector. 31, Nr. 3, 264–267. <http://dx.doi.org/10.1063/1.1716953>. – DOI 10.1063/1.1716953. – ISSN 0034–6748
- [13] DELFT, D. van ; KES, P. : The discovery of superconductivity. 63, Nr. 9, 38–43. <http://dx.doi.org/10.1063/1.3490499>. – DOI 10.1063/1.3490499. – ISSN 0031–9228
- [14] DELHUIILLE, R. ; MIFFRE, A. ; LAVALLETTE, E. ; BÜCHNER, M. ; RIZZO, C. ; TRÉNEC, G. ; VIGUÉ, J. ; LOESCH, H. J. ; GAUYACQ, J. P.: Optimization of a Langmuir–Taylor detector for lithium. 73, Nr. 6, 2249–2258. <http://dx.doi.org/10.1063/1.1472467>. – DOI 10.1063/1.1472467. – ISSN 0034–6748
- [15] DITMIRE, T. ; DONNELLY, T. ; RUBENCHIK, A. M. ; FALCONE, R. W. ; PERRY, M. D.: Interaction of intense laser pulses with atomic clusters. 53, Nr. 5, 3379–3402. <http://dx.doi.org/10.1103/PhysRevA.53.3379>. – DOI 10.1103/PhysRevA.53.3379
- [16] DRESCHER, M. ; HENTSCHEL, M. ; KIENBERGER, R. ; UBERACKER, M. ; YAKOVLEV, V. ; SCRINZI, A. ; WESTERWALBESLOH, T. ; KLEINEBERG, U. ; HEINZMANN, U. ; KRAUSZ, F. : Time-resolved atomic inner-shell spectroscopy. 419, Nr. 6909, 803. <http://dx.doi.org/10.1038/nature01143>. – DOI 10.1038/nature01143. – ISSN 1476–4687
- [17] EINSTEIN, A. : Über einen die Erzeugung und Verwandlung des Lichtes betreffenden heuristischen Gesichtspunkt. 322, Nr. 6, 132–148. <http://dx.doi.org/10.1002/andp.19053220607>. – DOI 10.1002/andp.19053220607. – ISSN 1521–3889
- [18] ENSS, C. ; HUNKLINGER, S. : *Low-Temperature Physics*. Springer-Verlag //www.springer.com/de/book/9783540231646. – ISBN 978–3–540–23164–6
- [19] EPPINK, A. T. J. B. ; PARKER, D. H.: Velocity map imaging of ions and electrons using electrostatic lenses: Application in photoelectron and photofragment

ion imaging of molecular oxygen. 68, Nr. 9, 3477–3484. <http://dx.doi.org/10.1063/1.1148310>. – DOI 10.1063/1.1148310. – ISSN 0034–6748

- [20] ERK, B. : *Nobel cluster gas expansion driven by a ultra-short high intensity infrared laser*
- [21] FECHNER, L. : *Aufbau eines Velocity-Map-Imaging-Spektrometers und winkelaufgeloste Spektroskopie an Rubidium-dotierten Helium-Nanotropfchen.* http://hacol13.physik.uni-freiburg.de/fp/Versuche/FP2/FP2-21-VMI/Diplomarbeit_Lutz_Fechner.pdf
- [22] FENNEL, T. ; MEIWES-BROER, K.-H. ; TIGGESBÄUMKER, J. ; REINHARD, P.-G. ; DINH, P. M. ; SURAUD, E. : Laser-driven nonlinear cluster dynamics. 82, Nr. 2, 1793–1842. <http://dx.doi.org/10.1103/RevModPhys.82.1793>. – DOI 10.1103/RevModPhys.82.1793
- [23] FERMI, E. : Quantum Theory of Radiation. 4, Nr. 1, 87–132. <http://dx.doi.org/10.1103/RevModPhys.4.87>. – DOI 10.1103/RevModPhys.4.87
- [24] GAVEAU, M.-A. ; BRIANT, M. ; VALLET, V. ; M. MESTDAGH, J. ; P. VISTICOT, J. : Reaction Between Barium and N₂O on Large Neon Clusters. http://dx.doi.org/10.1007/978-3-642-56800-8_57. – DOI 10.1007/978-3-642-56800-8_57. – ISBN 978 – 3 – 642 – 63150 – 4, S.827 – 838
- [25] GOUGH, T. E. ; MENGEL, M. ; ROWNTREE, P. A. ; SCOLES, G. : Infrared spectroscopy at the surface of clusters: SF₆ on Ar. 83, Nr. 10, 4958–4961. <http://dx.doi.org/10.1063/1.449757>. – DOI 10.1063/1.449757. – ISSN 0021–9606
- [26] GREBENEV, S. ; TOENNIES, J. P. ; VILESOV, A. F. : Superfluidity Within a Small Helium-4 Cluster: The Microscopic Andronikashvili Experiment. 279, Nr. 5359, 2083–2086. <http://dx.doi.org/10.1126/science.279.5359.2083>. – DOI 10.1126/science.279.5359.2083. – ISSN 0036–8075, 1095–9203
- [27] GRIFFITHS, D. J.: *Introduction to electrodynamics*. Fourth edition. Pearson. – ISBN 978–0–321–85656–2
- [28] GRÜNER, B. : *Femtosekundenspektroskopie an dotierten Heliumnanotröpfchen: Dissipative Vibrationsdynamik und Charakterisierung eines Nanoplasmas*
- [29] HAGENA, O. F. ; OBERT, W. : Cluster Formation in Expanding Supersonic Jets: Effect of Pressure, Temperature, Nozzle Size, and Test Gas. 56, Nr. 5, 1793–1802.

<http://dx.doi.org/10.1063/1.1677455>. – DOI 10.1063/1.1677455. – ISSN 0021–9606

- [30] HAGENA, O. F. ; OBERT, W. : Cluster Formation in Expanding Supersonic Jets: Effect of Pressure, Temperature, Nozzle Size, and Test Gas. 56, Nr. 5, 1793–1802. <http://dx.doi.org/10.1063/1.1677455>. – DOI 10.1063/1.1677455. – ISSN 0021–9606
- [31] HALPERIN, W. P. ; RASMUSSEN, F. B. ; ARCHIE, C. N. ; RICHARDSON, R. C.: Properties of melting 3He: Specific heat, entropy, latent heat, and temperature. 31, Nr. 5, 617–698. <http://dx.doi.org/10.1007/BF00116046>. – DOI 10.1007/BF00116046. – ISSN 1573–7357
- [32] HARMS, J. ; TOENNIES, J. P. ; DALFOVO, F. : Density of superfluid helium droplets. 58, Nr. 6, 3341–3350. <http://dx.doi.org/10.1103/PhysRevB.58.3341>. – DOI 10.1103/PhysRevB.58.3341
- [33] HAUGHT, A. F. ; POLK, D. H.: Formation and Heating of Laser Irradiated Solid Particle Plasmas. 13, Nr. 11, 2825–2841. <http://dx.doi.org/10.1063/1.1692869>. – DOI 10.1063/1.1692869. – ISSN 0031–9171
- [34] HEIDENREICH, A. ; GRÜNER, B. ; SCHOMAS, D. ; STIENKEMEIER, F. ; KRISHNAN, S. R. ; MUDRICH, M. : Charging dynamics of dopants in helium nanoplasmatics. <http://dx.doi.org/10.1080/09500340.2017.1281454>. – DOI 10.1080/09500340.2017.1281454
- [35] ISLAM, M. R. ; SAALMANN, U. ; ROST, J. M.: Kinetic energy of ions after Coulomb explosion of clusters induced by an intense laser pulse. 73, Nr. 4, 041201. <http://dx.doi.org/10.1103/PhysRevA.73.041201>. – DOI 10.1103/PhysRevA.73.041201
- [36] KAMENEV, A. : Introduction to the Keldysh Formalism.
- [37] KAPITZA, P. : Viscosity of Liquid Helium below the -Point. 141, Nr. 3558, 74. <http://dx.doi.org/10.1038/141074a0>. – DOI 10.1038/141074a0. – ISSN 1476–4687
- [38] KARNAKOV, B. M. ; MUR, V. D. ; POPRUZHENKO, S. V. ; POPOV, V. S.: Strong field ionization by ultrashort laser pulses: Application of the Keldysh theory. 374, Nr. 2, 386–390. <http://dx.doi.org/10.1016/j.physleta.2009.10.058>. – DOI 10.1016/j.physleta.2009.10.058. – ISSN 0375–9601
- [39] KELDYSH, L. V.: Ionization in the field of a strong electromagnetic wave. 20, 1307. <https://ci.nii.ac.jp/naid/10006486551/>

- [40] KNUTH, E. L. ; HENNE, U. : Average size and size distribution of large droplets produced in a free-jet expansion of a liquid. 110, Nr. 5, 2664–2668. <http://dx.doi.org/10.1063/1.477988>. – DOI 10.1063/1.477988. – ISSN 0021–9606, 1089–7690
- [41] KRISHNAN, S. R. ; FECHNER, L. ; KREMER, M. ; SHARMA, V. ; FISCHER, B. ; CAMUS, N. ; JHA, J. ; KRISHNAMURTHY, M. ; PFEIFER, T. ; MOSHAMMER, R. ; ULLRICH, J. ; STIENKEMEIER, F. ; MUDRICH, M. : Ignition of Doped Helium Nanodroplets in Intense Few-Cycle Laser Pulses. In: YAMANOUCHI, K. (Hrsg.) ; KATSUMI, M. (Hrsg.): *Multiphoton Processes and Attosecond Physics*, Springer Berlin Heidelberg (Springer Proceedings in Physics). – ISBN 978–3–642–28948–4, S. 385–390
- [42] KRISHNAN, S. R.: Doped helium nanodroplets in intense few-cycle infrared pulses. http://inis.iaea.org/Search/search.aspx?orig_q=RN:43095633
- [43] LAST, I. ; JORTNER, J. : Quasiresonance ionization of large multicharged clusters in a strong laser field. 60, Nr. 3, 2215–2221. <http://dx.doi.org/10.1103/PhysRevA.60.2215>. – DOI 10.1103/PhysRevA.60.2215
- [44] LEWERENZ, M. ; SCHILLING, B. ; TOENNIES, J. P.: Successive capture and coagulation of atoms and molecules to small clusters in large liquid helium clusters. 102, Nr. 20, 8191–8207. <http://dx.doi.org/10.1063/1.469231>. – DOI 10.1063/1.469231. – ISSN 0021–9606
- [45] LEWIS, W. K. ; HARRUFF-MILLER, B. A. ; LEATHERMAN, P. ; GORD, M. A. ; BUNKER, C. E.: Helium droplet calorimetry of strongly bound species: Carbon clusters from C₂ to C₁₂. 85, Nr. 9, 094102. <http://dx.doi.org/10.1063/1.4895670>. – DOI 10.1063/1.4895670. – ISSN 0034–6748, 1089–7623
- [46] MADISON, K. W. ; PATEL, P. K. ; ALLEN, M. ; PRICE, D. ; FITZPATRICK, R. ; DITMIRE, T. : Role of laser-pulse duration in the neutron yield of deuterium cluster targets. 70, Nr. 5. <http://dx.doi.org/10.1103/PhysRevA.70.053201>. – DOI 10.1103/PhysRevA.70.053201. – ISSN 1050–2947, 1094–1622
- [47] MAINFRAY, G. : MULTIPHOTON IONIZATION OF ATOMS.
- [48] MÖBIUS, E. ; GALVIN, A. B. ; KISTLER, L. M. ; KUCHAREK, H. ; POPECKI, M. A.: Time-of-flight mass spectrographs—From ions to neutral atoms. 121, Nr. 12, 11,647–11,666. <http://dx.doi.org/10.1002/2016JA022553>. – DOI 10.1002/2016JA022553. – ISSN 2169–9402

- [49] MEIJA, J. ; COPLEN, T. B. ; BERGLUND, M. ; BRAND, W. A. ; DE, B. P. ; GRÖNING, M. ; HOLDEN, N. E. ; IRRGEHER, J. ; LOSS, R. D. ; WALCZYK, T. ; PROHASKA, T. : Atomic weights of the elements 2013 (IUPAC Technical Report). 88, Nr. 3, 265–291. <http://dx.doi.org/10.1515/pac-2015-0305>. – DOI 10.1515/pac-2015-0305. – ISSN 0033-4545
- [50] MIKABERIDZE, A. : *Atomic and molecular clusters in intense laser pulses.* https://www.pks.mpg.de/mpi-doc/rostgruppe/dissertation/mikaberidze_dissertation.pdf
- [51] MOUROU, G. A. ; TAJIMA, T. ; BULANOV, S. V.: Optics in the relativistic regime. 78, Nr. 2, 309–371. <http://dx.doi.org/10.1103/RevModPhys.78.309>. – DOI 10.1103/RevModPhys.78.309
- [52] NAUTA, K. ; MILLER, R. E.: Nonequilibrium Self-Assembly of Long Chains of Polar Molecules in Superfluid Helium. 283, Nr. 5409, 1895–1897. <http://dx.doi.org/10.1126/science.283.5409.1895>. – DOI 10.1126/science.283.5409.1895. – ISSN 0036-8075, 1095–9203
- [53] PIETROWSKI, R. von ; RUTZEN, M. ; HAEFTEN, K. von ; KAKAR, S. ; MÖLLER, T. : Fluorescence excitation spectroscopy of Xenon doped Neon clusters: Size and site effects, and cluster melting. 40, S. 22–24. <http://dx.doi.org/10.1007/s004600050149>. – DOI 10.1007/s004600050149
- [54] POPRUZHENKO, S. V.: Keldysh theory of strong field ionization: history, applications, difficulties and perspectives. 47, Nr. 20, 204001. <http://dx.doi.org/10.1088/0953-4075/47/20/204001>. – DOI 10.1088/0953-4075/47/20/204001. – ISSN 0953-4075
- [55] PROTOPAPAS, M. ; KEITEL, C. H. ; KNIGHT, P. L.: Atomic physics with super-high intensity lasers. 60, Nr. 4, 389–486. <http://dx.doi.org/10.1088/0034-4885/60/4/001>. – DOI 10.1088/0034-4885/60/4/001. – ISSN 0034-4885, 1361–6633
- [56] RAFIPOOR, A. J. M.: *Two-Color Photoionization Experiments with Ultrashort Light Pulses on Small Atomic Systems*
- [57] RAY, A. ; SIKDAR, A. K. ; DE, A. : Quasifision timescale: Zeptosecond versus attosecond. 86, 00038. <http://dx.doi.org/10.1051/epjconf/20158600038>. – DOI 10.1051/epjconf/20158600038. – ISSN 2100–014X

- [58] REINHARD, P.-G. ; SURAUD, E. : *Introduction to cluster dynamics*. Wiley-VCH. – ISBN 978-3-527-40345-5. – OCLC: ocm51234499
- [59] RENDLER, N. : *EINZELSCHUSS ELEKTRONEN-IMAGING VON HELIUM-NANOPLASMEN IN INTENSIVEN NAHINFRAROT LASERFELDERN*
- [60] RHODES, C. K.: Multiphoton Ionization of Atoms. 229, Nr. 4720, 1345–1351. <http://dx.doi.org/10.1126/science.229.4720.1345>. – DOI 10.1126/science.229.4720.1345. – ISSN 0036-8075, 1095-9203
- [61] SAALMANN, U. ; SIEDSCHLAG, C. ; ROST, J. M.: Mechanisms of cluster ionization in strong laser pulses. 39, Nr. 4, R39–R77. <http://dx.doi.org/10.1088/0953-4075/39/4/R01>. – DOI 10.1088/0953-4075/39/4/R01. – ISSN 0953-4075, 1361-6455
- [62] SCHMIDT, V. : *Electron Spectrometry of Atoms using Synchrotron Radiation*. Cambridge University Press. – ISBN 978-0-521-55053-6
- [63] SCHOMAS, D. ; RENDLER, N. ; KRULL, J. ; RICHTER, R. ; MUDRICH, M. : A compact design for velocity-map imaging of energetic electrons and ions. 147, Nr. 1. <http://dx.doi.org/10.1063/1.4984076>. – DOI 10.1063/1.4984076. – ISSN 0021-9606
- [64] STEBBINGS, S. L. ; SÜSSMANN, F. ; YANG, Y.-Y. ; SCRINZI, A. ; DURACH, M. ; RUSINA, A. ; STOCKMAN, M. I. ; KLING, M. F.: Generation of isolated attosecond extreme ultraviolet pulses employing nanoplasmonic field enhancement: optimization of coupled ellipsoids. 13, Nr. 7, 073010. <http://dx.doi.org/10.1088/1367-2630/13/7/073010>. – DOI 10.1088/1367-2630/13/7/073010. – ISSN 1367-2630
- [65] STIENKEMEIER, F. ; LEHMANN, K. K.: Spectroscopy and dynamics in helium nanodroplets. 39, Nr. 8, R127–R166. <http://dx.doi.org/10.1088/0953-4075/39/8/R01>. – DOI 10.1088/0953-4075/39/8/R01. – ISSN 0953-4075, 1361-6455
- [66] STRINGARI, S. ; TREINER, J. : Systematics of liquid helium clusters. 87, Nr. 8, 5021-5027. <http://dx.doi.org/10.1063/1.452818>. – DOI 10.1063/1.452818. – ISSN 0021-9606
- [67] SWENSON, C. A.: The Liquid-Solid Transformation in Helium near Absolute Zero. 79, Nr. 4, 626–631. <http://dx.doi.org/10.1103/PhysRev.79.626>. – DOI 10.1103/PhysRev.79.626

- [68] TCHAPLYGUINE, M. ; LUNDWALL, M. ; GISSELBRECHT, M. ; ÖHRWALL, G. ; FEIFEL, R. ; SORENSEN, S. ; SVENSSON, S. ; MÅRTENSSON, N. ; BJÖRNEHOLM, O. : Variable surface composition and radial interface formation in self-assembled free, mixed ArXe clusters. 69, Nr. 3, 031201. <http://dx.doi.org/10.1103/PhysRevA.69.031201>. – DOI 10.1103/PhysRevA.69.031201
- [69] THIRÉ, N. ; MAKSIMENKA, R. ; KISS, B. ; FERCHAUD, C. ; GITZINGER, G. ; PINOTEAU, T. ; JOUSSELIN, H. ; JAROSCH, S. ; BIZOUARD, P. ; PIETRO, V. D. ; CORMIER, E. ; OSVAY, K. ; FORGET, N. : Highly stable, 15 W, few-cycle, 65 mrad CEP-noise mid-IR OPCPA for statistical physics. 26, Nr. 21, 26907–26915. <http://dx.doi.org/10.1364/OE.26.026907>. – DOI 10.1364/OE.26.026907. – ISSN 1094–4087
- [70] TOENNIES, J. P. ; VILESOV, A. F.: Spectroscopy of Atoms and Molecules in Liquid Helium. 49, Nr. 1, 1–41. <http://dx.doi.org/10.1146/annurev.physchem.49.1.1>. – DOI 10.1146/annurev.physchem.49.1.1
- [71] TOENNIES, J. P. ; VILESOV, A. F.: Superfluid Helium Droplets: A Uniquely Cold Nanomatrix for Molecules and Molecular Complexes. 43, Nr. 20, 2622–2648. <http://dx.doi.org/10.1002/anie.200300611>. – DOI 10.1002/anie.200300611. – ISSN 1521–3773
- [72] UIBERACKER, M. ; UPHUES, T. ; SCHULTZE, M. ; VERHOEF, A. J. ; YAKOVLEV, V. ; KLING, M. F. ; RAUSCHENBERGER, J. ; KABACHNIK, N. M. ; SCHRÖDER, H. ; LEZIUS, M. ; KOMPA, K. L. ; MULLER, H.-G. ; VRACKING, M. J. J. ; HENDEL, S. ; KLEINEBERG, U. ; HEINZMANN, U. ; DRESCHER, M. ; KRAUSZ, F. : Attosecond real-time observation of electron tunnelling in atoms. 446, Nr. 7136, 627–632. <http://dx.doi.org/10.1038/nature05648>. – DOI 10.1038/nature05648. – ISSN 1476–4687
- [73] WABNITZ, H. ; BITTNER, L. ; CASTRO, A. R. B. ; DÖHRMANN, R. ; GÜRTLER, P. ; LAARMANN, T. ; LAASCH, W. ; SCHULZ, J. ; SWIDERSKI, A. ; HAEFTEN, K. von ; MÖLLER, T. ; FAATZ, B. ; FATEEV, A. ; FELDHAUS, J. ; GERTH, C. ; HAHN, U. ; SALDIN, E. ; SCHNEIDMILLER, E. ; SYTCHEV, K. ; TIEDTKE, K. ; TREUSCH, R. ; YURKOV, M. : Multiple ionization of atom clusters by intense soft X-rays from a free-electron laser. 420, Nr. 6915, 482–485. <http://dx.doi.org/10.1038/nature01197>. – DOI 10.1038/nature01197. – ISSN 1476–4687
- [74] WEINBERGER, P. : The discovery of thermodynamics. 93, Nr. 20, 2576–2612. <http://dx.doi.org/10.1080/14786435.2013.784402>. – DOI 10.1080/14786435.2013.784402. – ISSN 1478–6435

- [75] WHITTLE, E. ; DOWS, D. A. ; PIMENTEL, G. C.: Matrix Isolation Method for the Experimental Study of Unstable Species. 22, Nr. 11, 1943–1943. <http://dx.doi.org/10.1063/1.1739957>. – DOI 10.1063/1.1739957. – ISSN 0021–9606, 1089–7690
- [76] WILEY, W. C. ; MCLAREN, I. H.: Time-of-Flight Mass Spectrometer with Improved Resolution. 26, Nr. 12, 1150–1157. <http://dx.doi.org/10.1063/1.1715212>. – DOI 10.1063/1.1715212. – ISSN 0034–6748
- [77] WITUSCHEK, A. ; VANGEROW, J. von ; GRZESIAK, J. ; STIENKEMEIER, F. ; MUDRICH, M. : A simple photoionization scheme for characterizing electron and ion spectrometers. 87, Nr. 8, 083105. <http://dx.doi.org/10.1063/1.4960401>. – DOI 10.1063/1.4960401. – ISSN 0034–6748, 1089–7623
- [78] YOUNG, D. A.: PHASE DIAGRAMS OF THE ELEMENTS.
- [79] ZEWAIL, A. H.: Femtochemistry: Atomic-Scale Dynamics of the Chemical Bond. 104, Nr. 24, 5660–5694. <http://dx.doi.org/10.1021/jp001460h>. – DOI 10.1021/jp001460h. – ISSN 1089–5639
- [80] ZHAO, K. ; ZHANG, Q. ; CHINI, M. ; WU, Y. ; WANG, X. ; CHANG, Z. : Tailoring a 67 attosecond pulse through advantageous phase-mismatch. 37, Nr. 18, 3891–3893. <http://dx.doi.org/10.1364/OL.37.003891>. – DOI 10.1364/OL.37.003891. – ISSN 1539–4794

Danksagung

An dieser Stelle Danke

Erklärung

Ort, Datum

Unterschrift